Rivista Italiana di Paleontologia e Stratigrafia
(*Research in Paleontology and Stratigraphy*)
vol. 123(3): 487-540. **November 2017**

DEPOSITIONAL ARCHITECTURE, FACIES CHARACTER AND GEOCHEMICAL SIGNATURE OF THE TIVOLI TRAVERTINES (PLEISTOCENE, ACQUE ALBULE BASIN, CENTRAL ITALY)

GIOVANNA DELLA PORTA[1*], ANDREA CROCI[2], MATTIA MARINI[1] & SANDOR KELE[3]

[1*]Corresponding author. Dipartimento di Scienze della Terra, Universita' degli Studi di Milano, via Mangiagalli 34, 20133, Milan, Italy. E-mail: giovanna.dellaporta@unimi.it; mattia.marini@unimi.it
[2] Department of Secondary Teacher Education, Manchester Metropolitan University, Brooks Building, 53 Bonsall Street, M15 6GX, Manchester, UK. E-mail: andrea.croci@stu.mmu.ac.uk
[3] Institute for Geological and Geochemical Research, Research Centre for Astronomy and Earth Sciences, Hungarian Academy of Sciences, 45 Budaörsi Street, 1112, Budapest, Hungary. E-mail: keles@geochem.hu

To cite this article: Della Porta G., Croci A., Marini M. & Kele S. (2017) - Depositional architecture, facies character and geochemical signature of the Tivoli travertines (Pleistocene, Acque Albule Basin, Central Italy). *Riv. It. Paleontol. Strat.*, 123(3): 487-540.

Keywords: travertine; Pleistocene; Tivoli; facies; depositional architecture; stable isotope geochemistry.

Abstract. Facies character, diagenesis, geochemical signature, porosity, permeability, and geometry of the upper Pleistocene Tivoli travertines were investigated integrating information from six borehole cores, drilled along a 3 km N-S transect, and quarry faces, in order to propose a revised depositional model. Travertines overlie lacustrine and alluvial plain marls, siltstones, sandstones and pyroclastic deposits from the Roman volcanic districts. In the northern proximal area, with respect to the inferred hydrothermal vents, travertines accumulated in gently-dipping, decametre-scale shallow pools of low-angle terraced slopes. The intermediate depositional zone, 2 km southward, consisted of smooth and terraced slopes dipping S and E. In the southernmost distal zone, travertine marshes dominated by coated vegetation and *Charophytes* interfingered with lacustrine siltstones and fluvial sandstones and conglomerates. Travertine carbon and oxygen stable isotope data confirm the geothermal origin of the precipitating spring water. The travertine succession is marked by numerous intraclastic/extraclastic wackestone to rudstone beds indicative of non-deposition and erosion during subaerial exposure, due to temporary interruption of the vent activity or deviation of the thermal water flow. These unconformities identify nine superimposed travertine units characterized by aggradation in the proximal zone and southward progradation in the intermediate to distal zones. The wedge geometry of the travertine system reflects the vertical and lateral superimposition of individual fan-shaped units in response to changes in the vent location, shifting through time to lower elevations southward. The complexity of the travertine architecture results from the intermittent activity of the vents, their locations, the topographic gradient, thermal water flow paths and the rates and modes of carbonate precipitation.

INTRODUCTION

Travertines are defined as terrestrial carbonates precipitated by water supersaturated with respect to calcium carbonate, typically hydrothermal in origin (Pedley 1990; Ford & Pedley 1996; Capezzuoli et al. 2014). Travertines form through abiotic (CO_2 degassing and evaporation of thermal water outflowing from the spring) and biologically mediated precipitation processes; they are characterized by common bacteria and cyanophytes and generally lack macrophytes (Chafetz & Folk 1984; Capezzuoli et al. 2014). Thermal water precipitating travertine is suggested to have temperature over 20°C (Pedley 1990) or 30°C (Capezzuoli et al. 2014). There is, however, general agreement that temperature based classifications of terrestrial spring carbonates are problematic to apply to the fossil record of inactive systems (Jones & Renaut 2010; Capezzuoli et al. 2014). Spring carbonates can also be differentiated in hydrothermal or thermogene travertines vs. ambient temperature calcareous tufa or meteogene travertine based on the sources of the dissolved inorganic carbon (DIC), geothermal vs. karstic meteoric respectively, as it can be inferred from the carbon stable isotopic signature of the precipitated carbonates (Pentecost & Viles 1994; Pentecost 2005; Capezzuoli et al. 2014).

The term travertine derives from the Italian *travertino* that comes from the Latin *lapis tiburtinus*,

Received: July 18, 2017; accepted: October 02, 2017

which meant "stone of Tibur" (Chafetz & Folk 1984; Faccenna et al. 2008). Tibur was the Roman name for the present-day town of Tivoli, located nearly 20 km east of Rome (Central Italy) along the Aniene River (Chafetz & Folk 1984; Faccenna et al. 2008). The Romans extensively quarried the travertines in the area west of Tivoli for construction purposes, since the III-II century BC and quarrying is still active at present. Hence, the upper Pleistocene Tivoli travertines represent the deposits from which the general lithology for this type of terrestrial carbonates derives and are the focus of this investigation.

Fundamental precursor studies on the Tivoli travertines by Chafetz & Folk (1984) highlighted the variety of precipitated carbonate fabrics and the complexity of physico-chemical and microbial processes involved in the precipitation of carbonates from thermal springs. Faccenna et al. (2008) proposed a depositional model for the Tivoli travertine system interpreting it as a plateau subdivided in benches separated by discontinuities controlled by fluctuations of the water table, driven by climatic oscillations and tectonic activity.

In the last years, there has been a renewed scientific interest on travertines from the academia and industry. This has been driven by the discovery of non-marine carbonate hydrocarbon reservoirs in the Lower Cretaceous syn-rift and sag phase sedimentary succession of the South Atlantic subsurface, despite the published data about the Pre-Salt carbonate reservoirs so far concern only alkaline lake carbonates (Wright 2012; Wright & Barnett 2015; Saller et al. 2016; Sabato Ceraldi & Green 2017). Nevertheless, dome- and eye-shaped hydrothermal vents have been identified through seismics in the Lower Cretaceous rift section of the Campos Basin, offshore Brazil (Alvarenga et al. 2016). The most studied travertine deposits are those of Pleistocene-Holocene age associated also with present-day active geothermal systems such as those in Central Italy, Hungary, Turkey and Yellowstone (Wyoming, USA). Numerous recent studies have focused on various aspects of these travertine depositional systems ranging from the variety of the fabric types, geochemical signature and diagenesis (Pola et al. 2014; Claes et al. 2015; Anzalone et al. 2017; Cook & Chafetz 2017; De Boever et al. 2017; Erthal et al. 2017; Rodríguez-Berriguete et al. 2017; Török et al. 2017), petrophysical reservoir properties (Chafetz 2013; Ronchi & Cruciani 2015; Soete et al. 2015; Brogi et al. 2016; De Boever et al. 2016; Claes et al. 2017ab), to the depositional geometry and evolution of the depositional system through time (De Filippis & Billi 2012; De Filippis et al. 2012; De Filippis et al. 2013ab; Croci et al. 2016; Wang et al. 2016; Della Porta et al. 2017) and to the use of travertine deposits as recorder of climatic oscillations and tectonic activity (Özkul et al. 2013; Van Noten et al. 2013; Bertini et al. 2014; Gradziński et al. 2014; Toker et al. 2015; Brogi et al. 2017; Frery et al 2017). All these recent studies highlight the variability and complexity of travertine depositional systems from the centimetre scale of the carbonate fabric types to the depositional geometry, affected by numerous extrinsic and intrinsic controlling factors ranging from the regional tectonics, climatic regime to the substrate topography and thermal water physico-chemical properties.

This study aims to propose a revised depositional model of the Tivoli travertines linked to a detailed facies characterization of both the travertines and underlying sedimentary and volcanic substrate deposits based on six borehole cores, complemented with diagenetic, stable carbon and oxygen isotope and porosity and permeability data. Detailed facies information has been integrated in a digital 3D model that combines the centimetre-scale stratigraphic information from the cores with the tens to hundreds metre-scale depositional geometry from excavated quarry walls. This model allows getting better insights of the evolution of the travertine geometry through time and the sedimentary dynamics that affect the geometry of a travertine depositional system.

Geological setting

Tectonics and stratigraphy

The Acque Albule Basin (AAB) is a fault-controlled, elongated (nearly 7 x 4 km) south-dipping depression located to the west of the town of Tivoli, north of the Pleistocene Alban Hills volcanic district (Fig. 1). To the north and east, the AAB is surrounded by mountain ranges, i.e. the Cornicolani, Lucretili, Tiburtini and Prenestini Mts., belonging to the east-verging thrust sheets of the Central Apennine orogen (Cosentino &

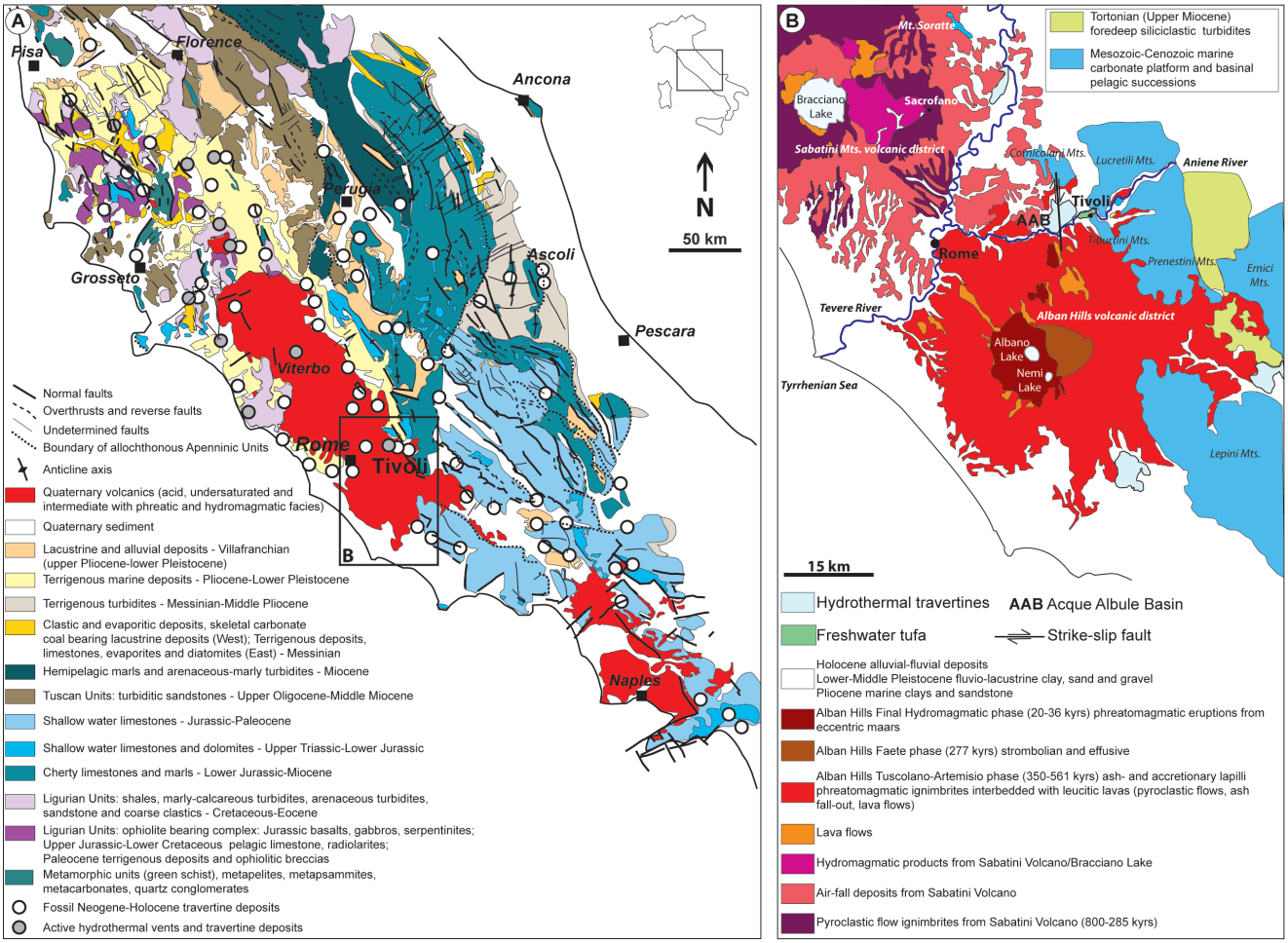

Fig. 1 - A) Synthetic geological map of Central Italy (modified after Bigi et al. 1990) with location of active and fossil hydrothermal springs extracted from Minissale (2004). B) Synthetic geological map of the area between Rome and Tivoli showing the two volcanic districts of the Roman magmatic province (Albani Hills and Sabatini Mts.), the Tivoli upper Pleistocene travertines and the Apennine Mesozoic-Cenozoic carbonate units in the North and East of the Tivoli travertine deposits in the Acque Albule Basin (redrafted after De Rita et al. 1995, 2002; Gaeta et al. 2000; Karner et al. 2001; Faccenna et al. 2008; De Filippis et al. 2013ab).

Parotto 1986; Corrado et al. 1992) and consisting of Mesozoic-Cenozoic carbonate platform and basinal pelagic successions, and Neogene foredeep siliciclastic turbidites (Bollati et al. 2011, 2012). From the late Miocene (Tortonian), this sector of the Central Apennine underwent extensional tectonics as a result of the opening of the Tyrrhenian Sea as a back-arc basin, driven by the westward subduction of the Adriatic-Ionian plate underneath the European plate (Malinverno & Ryan 1986; Doglioni 1991; Patacca et al. 1992; Gueguen et al. 1997). Extensional tectonics was associated with lithospheric thinning, NW-SE normal faulting, and seismic, volcanic and geothermal activity (Faccenna et al. 2008 and references therein). NW-striking normal faults, which often reactivated former Apennine thrust planes, and NE-striking transfer faults controlled the development of numerous Late Miocene-Quaternary extensional basins in Central Italy (Patacca et al. 1992; Faccenna et al. 1994abc, 2008; Carminati & Doglioni 2012). These fault-controlled basins are filled by discordant marine Pliocene claystone and Pliocene-Pleistocene to Holocene lacustrine and fluvial-alluvial successions (Mancini et al. 2014; Milli et al. 2017), which at their top are intercalated with Middle-Upper Pleistocene to Holocene volcanic deposits from the Sabatini Mts. and the Albani Hills volcanic complexes (Fig. 1B) of the Roman magmatic province (Funiciello et al. 2003; Bollati et al. 2011, 2012). This volcanic activity, related to the extensional regime affecting the Tyrrhenian Sea and the inner sector of the Central Apennine (Fig. 1), was characterized by explosive volcanism yielding

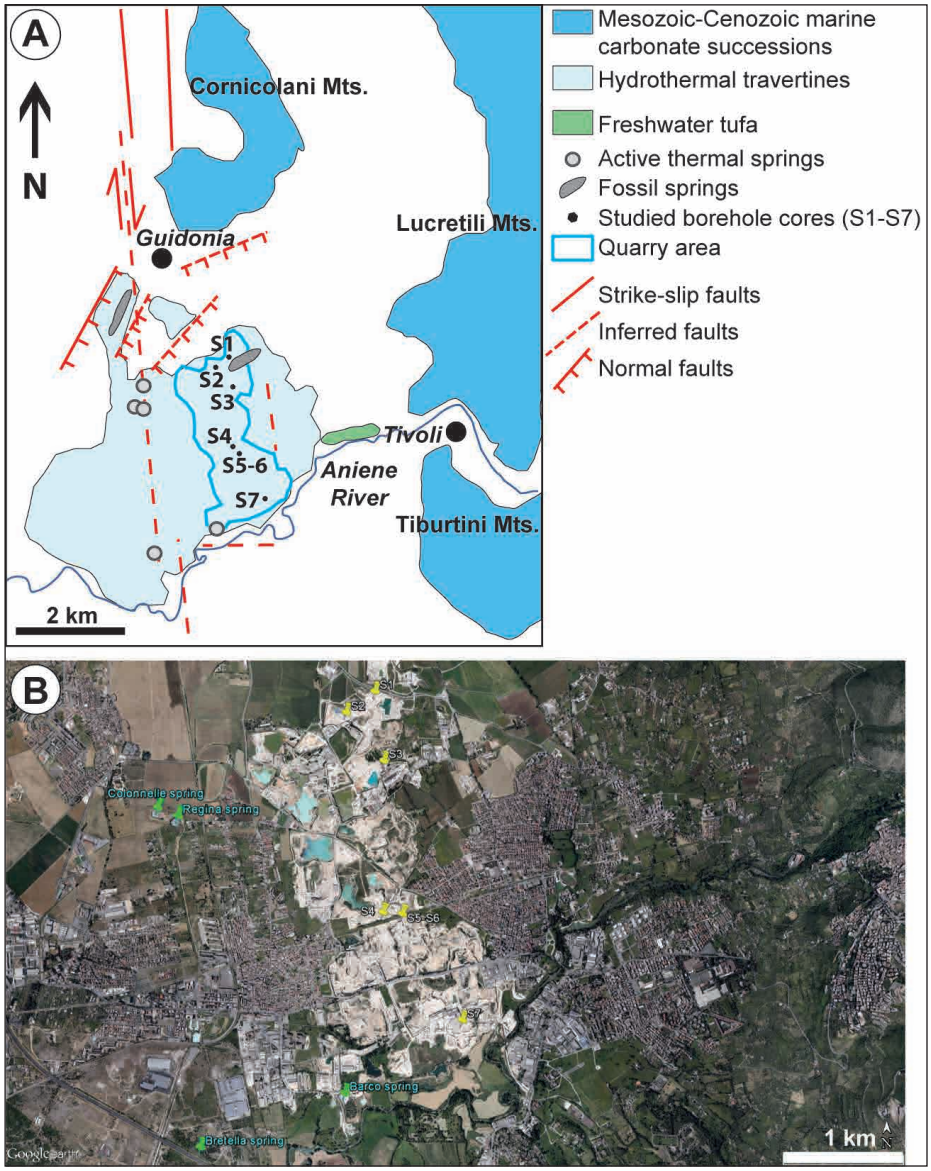

Fig. 2 - A) Synthetic geological map showing the location of the Acque Albule Basin bounded by strike-slip and normal faults and the travertine deposits located North of the Aniene River, with the Tiburtini and Lucretili Mts. on the East and the Cornicolani Mts. in the North made of Mesozoic-Cenozoic marine carbonate successions (redrafted after Faccenna et al. 2008; Brunetti et al. 2013; De Filippis et al. 2013ab). The area of active quarrying west of the town of Tivoli is marked by a blue line. The locations of the Statoil drilled boreholes object of this study (S1 to S7) are reported. B) Google Earth Pro image showing the travertine quarried area, identified by the white colour of the travertines, with the location of the six boreholes drilled by Statoil (S1 to S7) and the present-day active thermal springs.

mafic K- and high K-rich pyroclastic deposits and lavas (Serri et al. 1992, 1993; De Rita et al. 1995, 2002; Gaeta et al. 2000; Marra et al. 2009). The activity of the Sabatini Mts. and Albani Hills volcanoes (Fig. 1B) started from nearly 800 kyr and 561 kyr, respectively, and intermittently continued to 36 kyr (De Rita et al. 1995; Karner et al. 2001). The Albani Hills volcano recorded significant activity between 561 and 250 kyr, followed by a period of relative volcanic dormancy between 250 and 45 kyr and the final Hydromagmatic Phase dated at 36 kyr (Karner et al. 2001). During the Late Pleistocene-Holocene, N-striking right-lateral and NE-striking transtensional to normal faults (Figs 1B, 2) controlled the hydrothermal circulation and the deposition of travertines dated at 115-30 kyr (Faccenna et al. 2008).

Hydrogeology

The hydrogeological system of the AAB (Fig. 3) comprises two connected aquifers: 1) a deep, partly confined aquifer, hosted in fractured Mesozoic-Cenozoic marine limestone strata, and 2) a shallow, unconfined to semi-confined aquifer within the upper Pleistocene travertine deposits (Petitta et al. 2010; Carucci et al. 2012; La Vigna et al. 2013ab, 2016). These two carbonate aquifers are separated by low permeability discontinuous Pliocene marine claystone deposits overlain by Pliocene-Pleistocene continental siliciclastic sandy clayey sequences and Pleistocene volcanic deposits, which constitute either an aquitard or aquiclude (Di Salvo et al. 2013; La Vigna et al. 2013a). The deep confined aquifer is influenced by deeply sourced, high salinity, Ca-Mg-HCO_3-SO_4 and CO_2 rich fluids (Carucci et al.

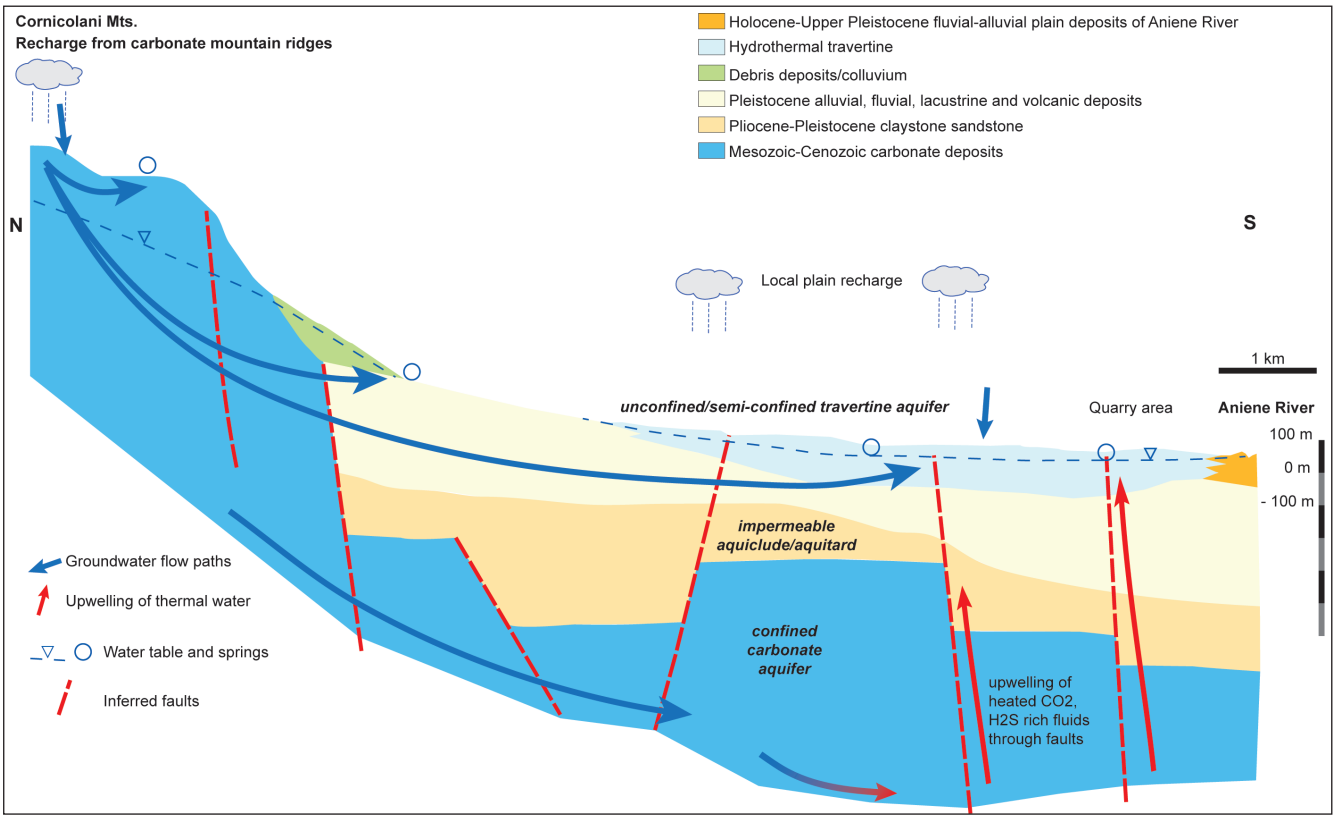

Fig. 3 - Hydrogeological model for the travertine Tivoli plain (redrafted after Carucci et al. 2012; Brunetti et al. 2013; La Vigna et al. 2013ab, 2016). Thermal water has low temperature because of the mixing between the deep geothermal fluids from the confined carbonate aquifer and the shallow travertine aquifer fed by superficial drainage.

2012) as well as by geothermal heat related to the Albani Hills magmatism (Minissale et al. 2002; Billi et al. 2006; Faccenna et al. 2008; Di Salvo et al. 2013). The Ca-Mg-HCO_3 composition is attributed to decarbonation of the Mesozoic-Cenozoic carbonates, whereas the high concentration of sulphate is caused by leaching of the Triassic evaporitic Burano Formation (Minissale et al. 2002; Minissale 2004). The travertine aquifer is presently unconfined in the quarried area (Fig. 2), whereas it is semi-confined where it is still overlain by soils and alluvial-lacustrine deposits post-dating travertine deposition (Carucci et al. 2012; Di Salvo et al. 2013; La Vigna et al. 2013ab). Groundwater is directly fed by rainfall and seepage from the surrounding carbonate ridges, being the travertines the terminal sector of the drainage path feeding into the Aniene River (Fig. 3; Petitta et al. 2010; Carucci et al. 2012; Di Salvo et al. 2013; La Vigna et al. 2013ab). The deep carbonate and shallow travertine aquifers are connected through tectonic discontinuities that allow the upwelling of deep, high-temperature, CO_2-rich mineralized water and the mixing with shallow, ambient temperature, meteoric water derived from the carbonate ridges and superficial drainage (Minissale et al. 2002; Carucci et al. 2012; De Filippis et al. 2013a). This mixing can explain the presence of water with high mineralization but low temperatures feeding the travertine aquifer (Petitta et al. 2010).

The current active thermal springs are located along the NNW-SSE shear zone in the west of the travertine quarry area (Pentecost & Tortora 1989; Minissale et al. 2002) and in the southern area (Figs 2A, B). The Colonnelle and Regina springs discharge 2-3 $m^3 s^{-1}$ of water (Carucci et al. 2012; La Vigna et al. 2013a) with temperature around 23°C, pH 6.0-6.2, Ca 520 mg/kg, Mg 116 mg/kg, HCO_3^- 1488 mg/kg, SO_4^{2-} 734 mg/kg, and pCO_2 0.6 atm (Pentecost & Tortora 1989; Minissale et al. 2002; Minissale 2004; Carucci et al. 2012; La Vigna et al. 2013a; Di Salvo et al. 2013). The springs are generally supersaturated with respect to calcium carbonate, which explains the travertine deposition (Minissale et al. 2002; Carucci et al. 2012).

Previous studies on Tivoli travertines

Chafetz and Folk (1984) interpreted the Tivoli travertines as lake-fill deposits, made of horizon-

tally stratified and laterally extensive accumulations, vertically affected by paleokarst due to periodic lake drainage. The travertines were primarily composed of vertically stacked centimetre-thick layers of shrubs, laterally interrupted by zones composed of calcite ray crystals, intraclasts, and pisoids indicative of spring deposits on the lake bottom.

Faccenna et al. (2008) reconstructed a depositional model of the Tivoli travertine unit, interpreting it as a tabular plateau made of sub-horizontal benches, separated by erosional surfaces, with a progradational pattern and southward steepening of strata. The plateau covers an area nearly 20 km^2 wide with average thickness of 40-50 m, for a total volume of 1 km^3 (Faccenna et al. 2008; De Filippis et al. 2013ab). The depocentre, with maximum thickness up to 80-90 m, coincided with a main N-striking fault and the associated emergences of thermal water (Faccenna et al. 2008). The five identified erosional surfaces and the alternating stages of bench deposition and erosion were suggested to be controlled by episodic fluctuations of the water table influenced by Pleistocene palaeoclimate, fault-related deformation and nearby volcanic activity (Faccenna et al. 2008; De Filippis et al. 2013a). The uppermost and youngest erosional surface separates the travertine deposits from the overlying "testina" unit, consisting of 3-4 m thick, poorly lithified travertine capping most of the Tivoli plateau and dated at 29 ± 4 kyr (Faccenna et al. 2008; De Filippis et al. 2013b). The presence of a fissure ridge structure was identified by De Filippis et al. (2013a) in the NW corner of the Tivoli travertine deposits. The Colle Fiorito fissure ridge was 2 km long and nearly 15 m high and must have accumulated when the volumetric deposition rate reached its climax for the abundance of fluid discharge and the rise of water table (De Filippis et al. 2013a).

Anzalone et al. (2017) investigated a nearly 30 m thick borehole core drilled in the NW Tivoli quarry area and linked the core stratigraphy to the depositional geometry visible in nearby saw-cut quarry walls. They interpreted the Tivoli travertines as accumulated in shallow lake to gentle slope environments with deposition marked by numerous erosional/non depositional discontinuities of different orders and magnitudes. Using sedimentological, stratigraphic and geochemical data they developed a cyclostratigraphic model of the drilled travertine core identifying high-frequency cycles driven by water table fluctuations controlled by millennial scale climatic cycles, medium term sub-Milankovitch and precession-driven Milankovitch climatic fluctuations.

The depositional model proposed for the Tivoli travertines by Erthal et al. (2017) consists of an extensive water-logged flat setting varying laterally into a slope system. These authors investigated in detail the travertine facies focussing on the shrub fabrics and identified six different types of shrub morphologies, linking them to the depositional conditions, water flow hydrodynamic, CO_2 degassing rate, evaporation and influence of microbially mediated precipitation. Slow thermal water flow favours greater contribution of microbially mediated processes to carbonate precipitation that results in arborescent, arbustiform and pustular shrub morphologies, more fragile and made of clotted peloidal micrite aggregates (Erthal et al. 2017).

Material and methods

The investigation of the stratigraphy and facies character of the Tivoli travertines and of the underlying volcanic and sedimentary substrate rocks is based on six research borehole cores (labelled from S1 to S7), drilled by Statoil ASA in 2010, within the active travertine quarry area, west of Tivoli (Fig. 2). The boreholes are located along a nearly 3100 m long transect, extending from well S1 in the north to well S7 in the south. Elevations vary from 68-57 m a.s.l. in the north (wells S1, S2, S3) to nearly 34 m a.s.l. in the south (well S7), close to the Aniene River. Because borehole S5 had limited recovery, corresponding to the uppermost stratigraphic interval of borehole S6, description of core S5 is combined with core S6. The total thickness of the six investigated borehole cores ranges from 35 m to 50 m; each core includes 19-43 m of travertines. At each location, the borehole was drilled on the topmost and youngest suitable quarry bench of travertine excavation; therefore the drilled cores do not include the top 10-20 m thick succession overlying the travertines made of the uppermost Pleistocene-Holocene alluvial and fluvial-lacustrine deposits and the so called "testina" unit (cf. Faccenna et al. 2008). Cores were analysed at the millimetre scale through mesoscale core description complemented with petrographic analysis of thin sections (160 thin sections from the travertines; 83 thin sections from the terrigenous and volcanic deposits).

Cathodoluminescence was performed on 12 thin sections with a luminoscope CITL Cambridge Image Technology Limited, Cambridge, UK (model MK 5-2 operating system at 10-14 kV with a beam current between 300-600 μA, and vacuum gauge 50-70 millitor) at the Earth Sciences Department, Milan University. Scanning Electron Microscope (SEM) analyses were performed on polished slabs, thin sections and freshly broken surfaces, gold coated, with a Cambridge Stereoscan 360, operating at 20 kV with working distance of 15 mm at the Earth Sciences Department, Milan University. Mineralogy of the travertine facies was investigated on 8 powder samples with X-ray powder diffraction (XRD) analytical technique, by means of a X-RAY Powder Diffractometer Philips X'Pert MPD with high temperature chamber at the laboratory of the University of

Milan. For all samples, qualitative analyses were made with Panalytical X'Pert HighScore software to identify the crystalline phases.

Thirty-five plugs (1 inch in diameter) sampled from core S1 were measured for porosity and permeability with a Helium gas expansion porosimeter at the Weatherford Labs by Statoil ASA (Bergen, Norway). In addition to plug porosity-permeability measurements, the porosity of each distinguished travertine facies was semi-quantitatively estimated through image analysis by determining the percentage of pore space per area from thin section photomicrographs (areas of nearly 2–4 cm^2) with the software ImageJ.

Stable isotope (oxygen and carbon) analyses on 208 carbonate powder samples were determined using an automated carbonate preparation device (Gasbench II) and a Thermo Fisher Scientific Delta Plus XP continuous flow mass spectrometer at the Institute for Geological and Geochemical Research, Hungarian Academy of Sciences, Budapest, Hungary. Carbonate powders were extracted with a dental microdrill avoiding the mixing of carbonate components and were reacted with 100% phosphoric acid at 70°C. Standardization was conducted using laboratory calcite standards calibrated against the NBS-19 standard. The carbon and oxygen isotope compositions are expressed in the conventional delta notation against the international standard V-PDB (for $\delta^{13}C$ and $\delta^{18}O$). Reproducibility for both C and O isotope analyses is better than ± 0.1 ‰.

Facies types, their vertical stacking and key stratigraphic boundaries identified through core logging were integrated with observations of depositional geometries and stratigraphic architectures on saw-cut quarry faces, adjacent to the locations where the borehole cores were drilled, complemented with high resolution georeferenced photographs of the quarry walls provided by Statoil ASA (Durand 2011) and satellite imagery from Google Earth Pro®. The outcrop spatial information and vertical facies stacking from core data were used to develop a 3D digital model of the travertine deposit using the software Petrel 2015® (Schlumberger). Points and polylines belonging to key stratigraphic boundaries digitized from georeferenced, orthorectified quarry wall photographs at Statoil ASA were used as input data for surface interpolation, which was accomplished by means of either a convergent interpolation algorithm or a functional surface algorithm depending on the nature and expected geometry of each stratigraphic surface. The 3D Petrel digital model allowed visualizing the architecture of the travertine units bounded by the interpolated surfaces and populated with the facies types extracted from core description. This digital model of the Tivoli travertines provided better insights on the evolution of the depositional system architecture through time and space.

Results

Travertine, terrigenous and volcanic facies

The analysed cores (Fig. 4) are composed of fourteen travertine facies (T1-T14) made of low Mg calcite, vertically stacked at the centimetre to decimetre-scale. Travertine facies types were distinguished on the basis of texture, precipitated carbonate fabric and components and classified according to the terminology proposed by Della Porta (2015), Croci et al. (2016) and Della Porta et al. (2017). The description of the travertine facies (Figs 5-9A-D) is summarised in Table 1. The post-travertine carbonate precipitates and sediment filling that accumulated within primary voids and secondary dissolution vugs to metre-scale karstic caves (C1, C2) are shown in Figures 9E-K. Additional travertine diagenetic features are reported in Figure 10. The terrigenous and volcanic deposits, mostly underlying the main travertine deposits (Fig. 4), were distinguished in ten facies (F1-F10) on the basis of lithology and composition (siliciclastic, carbonate, volcanic and volcaniclastic), dominant grain size, sedimentary structures and degree of lithification (Table 2; Figs 11, 12). The terrigenous deposits include black colour mudstone (F1), marl (F5), fine sand, silt and clay (F6) with rare layers with carbonate encrusted *Charophytes* algae and plant stems (facies T14) and loose sand, sandstone and conglomerate (F7 to F10). The volcanic deposits include facies F2, F3 and F4 representing pyroclastites with feldspars and feldspatoids, and volcanic ashes.

Post-travertine sediment filling and diagenetic features

The travertine primary and secondary vuggy porosity display various types of sediment fillings ranging from light to dark grey colour, silt- to mud-grade mixed detrital calcite crystals, travertine intraclasts, terrigenous sediment and yellowish ostracode wackestone/packstone (Fig. 9K), laminated or structureless, locally associated with millimetre-thick calcite rafts (C1 in Figure 4). The thickness of these deposits varies from 2 cm up to 20 cm. A particular kind of vug filling deposit (C2 in Figure 4; Figs 9E-J) consists of dark to light brown concentric laminated and vertically oriented columnar carbonate cementstone structures adjacent to extraclastic packstone to grainstone and rudstone and pisoidal packstone/grainstone to rudstone. These deposits only occur in core S7 in a nearly 5 m thick interval at core depths of 13.50-18.50 m (Fig. 4), comprised between the underlying T9 facies and the overlying F6 siltstone. The columnar decimetre-size structures (Fig. 9G) are formed by discontinuous sparitic laminae with crystal fans with undulose extinction alternating with micrite/microsparite crusts (10-100 μm thick), embedding tufts of possible calcified filamentous cyanobacteria (Figs 9E-F). Some of the micrite laminae show some weak to bright orange luminescence in cathodoluminescence analysis. The extraclastic packstone to rudstone includes angular clasts, up to 2 cm in size, deriving from the Mesozoic-Cenozoic successions cropping out in the rid-

ges surrounding the Tivoli area (Figs 1, 2). Pisoids forming packstone/grainstone to rudstone are 1-20 mm in diameter and consist of concentric micrite laminae (10-200 μm thick) coating nuclei made of extraclasts (Neogene marine carbonates, planktonic and benthic foraminifer wackestone/packstone, detrital quartz and chert) and travertine intraclasts (Figs 9H-J). The micrite/microsparite matrix around pisoids and extraclasts includes ostracodes, phosphatic and siliciclastic detrital grains. The pisoidal grainstone is cemented by limpid equant calcite sparite with drusy mosaics preceded by meniscus micritic crusts.

The diagenetic features observed in the travertine facies types (Table 1) appear to be similar and can be subdivided into: cement types, recrystallization features, dissolution and pedogenetic features. Cement types lining the pore walls (Figs 10A-G) include, in order of occurrence: a) micritic to sparitic pendant cement that, when present, is the first cement phase observed; b) equant microsparite to sparite forming blocky mosaics; c) prismatic calcite cement with scalenohedral terminations forming more than 1 mm long crystals. In some cases primary voids show geopetal ostracode wackestone infill (C1) that postdates the pendant cement and precedes or postdates the prismatic cement precipitation (Fig. 10F). Cathodoluminescence analysis shows that most of the precipitated travertines and cement types are non-luminescent. Nevertheless, the crystalline dendrites (T1), clotted peloidal micrite dendrite (T2) and radial coated grains (T6) might show a weak luminescence (Figs 10H-K). The prismatic scalenohedral and blocky calcite cements show some luminescent growth phases (Figs 10J, K). Evidence of recrystallization of the turbid lozenge shaped crystals (facies T1 and T6) in limpid blocky sparite and of the clotted peloidal micrite (facies T2) into microsparite to sparite are also observed (Figs 10L-M). Dissolution features range from sub-millimetre size vugs to metre-size caves and vertically oriented conduits. Dissolution affected also the clotted peloidal micrite framework and the prismatic calcite cement lining the primary pores (Fig. 10N). Rarely, in facies T9 and T11, pyrite crystals occur in the intercrystalline space within the pore filling blocky cement mosaic. Quarry wall observations indicate that facies T13 detrital travertine packstone/rudstone is often associated with decimetre to metre-thick terrigenous clay layers and paleosols. These deposits were not identified in cores due to lack of core recovery during drilling through clay beds. However, pedogenetic features such as circumgranular cracks and alveolar texture were observed in thin sections (Fig. 10O).

Travertine SEM analysis

SEM analysis of travertine samples shows that the limpid equant microsparite to sparite (20-100 μm) cement lining the pores consists of euhedral rhombohedral calcite crystals growing on the micritic primary precipitates (Fig. 13A). The turbid lozenge shaped crystals forming the T1 crystalline dendrites show a nanometre scale internal mouldic porosity with moulds that can show squared, rounded or dumb-bell cross sections (Fig. 13B). Some broken crystals show that they are internally composed of sub-micron scale clots of micrite (Fig. 13C). This internal structure of the dendrite crystals might explain their turbid micritic-like appearance under the polarized light microscope. SEM investigation of clotted peloidal micrite dendrites shows that they consist of clots (5-60 μm in diameter) made of submicron-scale calcite from which columnar bladed microsparite crystals (20-100 μm long) depart radially (Fig. 13D). The central micrite clots can consist of either nanometre-scale (0.1-1 μm) anhedral sub-spherical calcite structures (Fig. 13E) or euhedral dodecahedral carbonate crystals (Fig. 13F). T2 and T6 facies show the presence of organic membrane embedding micron-size clots of calcite and coccoid, filamentous and dumb-bell micron-size bacterioform structures (Figs 13G, H).

Travertine porosity and permeability

Mean porosity calculated through image analysis on thin section areas ranges between 2 and 15 %, with the highest values estimated for facies T4 to T8 and T13 (Table 1). Porosity and permeability measured on plugs from core S1 show variations of both parameters with respect to facies types (Fig. 14). Facies T2, T4, T8, T10 and T13 have the highest porosity (10-25 %). Permeability varies from 0.005 to 7038 mD and samples with the highest permeability (> 100 mD) belong to facies T2, T8, T10 and T14. Facies T2 and T8 show 5-15 % porosity and variable permeability, from 0.1 to 1000 mD, which might even decrease at increasing porosity. Facies T13 shows a positive linear correlation between permeability and porosity, which

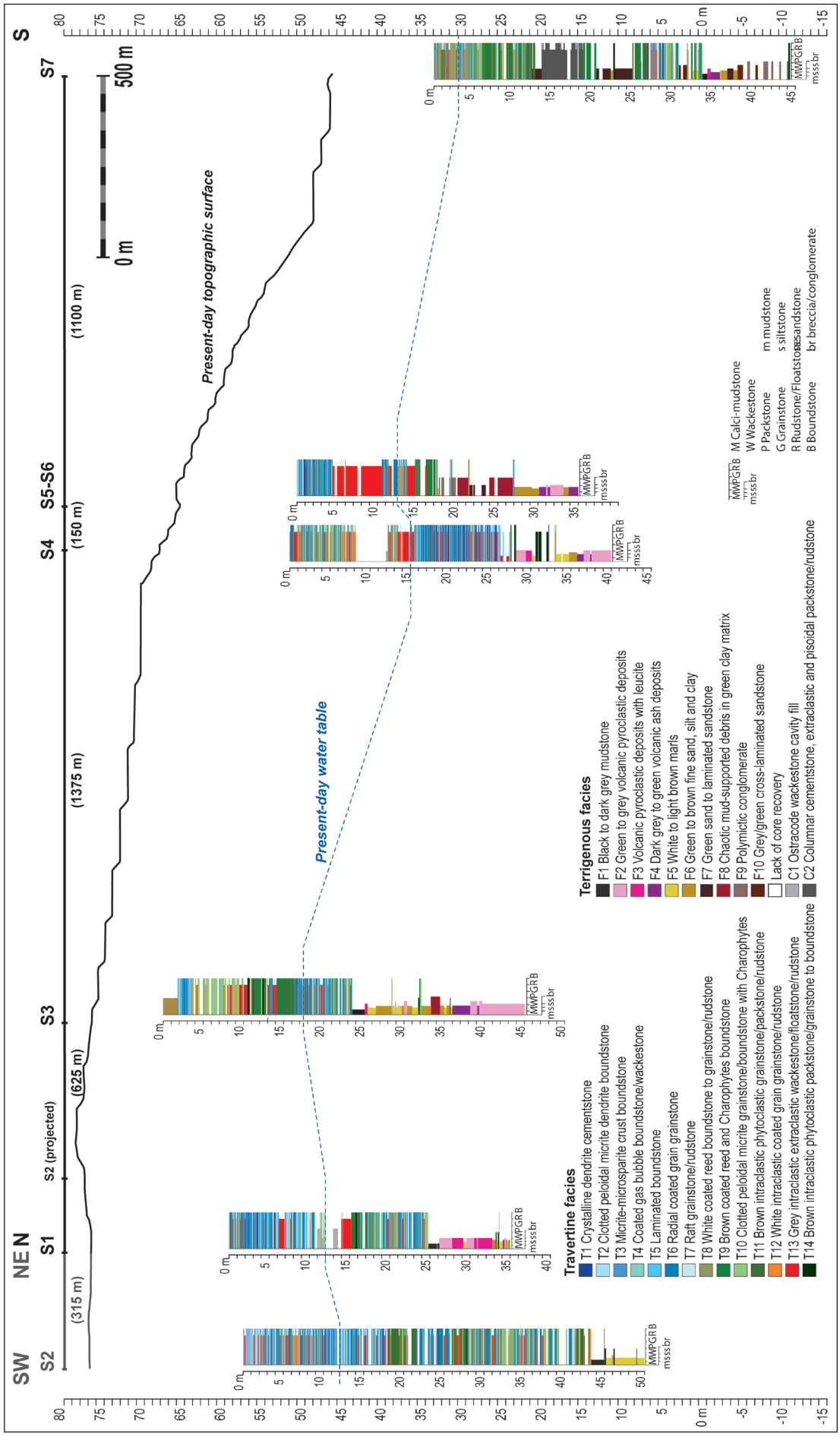

Fig. 4 - Stratigraphic logs of the six analysed cores along a transect oriented nearly N-S with exception of S1-S2 that are along a NE to SW transect. The upper black line represents the topographic surface as extracted from the topographic map of the Tivoli area. The dashed blue line represents the present-day water table depth as identified during core drilling. Detailed facies descriptions are provided in Table 1 and 2.

Facies	Core description	Petrographic analysis	Thickness and spatial distribution	Diagenetic features	Porosity (% area in thin section)	Depositional processes and environment
T1 Crystalline dendrite cementstone (Figs 5A-F)	White dense, mms to few cms thick layers of branching dendritic calcite crystals, adjacent to each other, growing upward. Sub-parallel stacked layers from horizontal to inclined up to 45° (smooth slope); cm to dm-size rounded convex-outward morphologies (pool rims of terraced slope); few cms wide, mms high, stepped morphology (micro-terraces). Crystals may show sub-parallel mm-thick growth laminae.	Cementstone of lozenge-shaped turbid, inclusion-rich crystals (100-600 µm long, 40-60 µm wide) departing from a central elongated crystal acting as a stalk (uniform extinction under crossed polarizers). When central stalk crystal absent, pairs of lozenge crystals form vertically stacked "v" (uniform or undulose extinction). The dark turbid appearance resembles crystals consisting of aggregated micrite acquiring euhedral rational crystal faces. Transitions of T1 dendrites from/into T2 micritic dendrite.	Beds: 5 mm to 20 cm thick (S5-S6), generally 2-5 cm; maximum thickness: 20 cm (S5-S6). T1 in all cores from 1.5 to 9% (S4). T1 associated laterally with T6 or T2; vertically alternating with T5, T3, T6, T2 and T13.	T1 dendrites surrounded by 1) cloudy microsparite (10-20 µm); 2) limpid equant microsparite to sparite (20-100 µm); 3) followed by prismatic scalenohedral cement, syntaxial with same extinction pattern as T1 crystal. T1 crystals partly replaced by limpid calcite spar (meteoric diagenesis). Meteoric alteration might produce both micritization and sparitization.	min: 0.3%; max: 10%; average: 3%. Inter-dendrite, between adjacent crystals.	Physico-chemical precipitation due to rapid CO_2 degassing in high-energy turbulent, fast flowing thermal water settings, close to the vent and on inclined steeply dipping surfaces of slopes, rims and walls of pools in terraced slopes and micro-terraced inclined surfaces (cf., Folk et al. 1985; Jones & Renaut 1995, 2010; Guo & Riding 1998; Chafetz & Guidry 1999; Della Porta 2015). Dendrites form due to high disequilibrium during rapid precipitation with impurities and crystal defects promoting crystal splitting (Jones & Renaut 1995).
T2 Clotted peloidal micrite dendrite boundstone (Figs 5G-K)	White to light tan, branching bush-like dendritic structures (few mms to cms thick, 1-15 mm wide), upright oriented and adjacent to each other in rows vertically stacked, separated by mm-thick dense micritic or microsparitic crusts (T3). Beds horizontal, parallel or undulated at the cm-scale; T2 can form stepped micro-terraces or convex upward mounded morphologies.	Boundstone of vertically superimposed T2 layers; dendrites made of irregular micrite clots (10-20 µm in diameter, rarely up to 50 µm) embedded in micrite and/or cloudy equant microsparite (5-50 µm) forming branches (100s µms to mms long) departing from a basal substrate or from an elongated upright central stem. T2 layers are separated by sub-mm leiolitic or peloidal micrite laminae (T3). Rare ostracodes, gastropods, mm-size bivalves and possible insect larval cases. Sparse coated gas bubbles and micrite laminae. Some T2 dendrites transitional into T1 (branches with geometric lozenge shapes with sharp boundaries made of dense micrite).	Beds: sub-horizontal or undulated, 0.2-5 cm thick; cm-dm size convex-upward mounded structures; maximum thickness: 10-20 cm (S2). T2 in all cores from 0.5 to 10% (S2). T2 vertically alternating with mm-thick T3, T2 associated with T4, T6 and T7.	T2 dendrites surrounded by: 1) equant microsparite to sparite (20-150 µm in size); 2) prismatic scalenohedral crystals (100s µm to 1 mm); 3) locally preceded by pendant vadose cement and micrite crusts. Irregular sparite substituting the micrite forming the branches (sparitization driven by meteoric diagenesis). Micrite dissolution due to meteoric diagenesis produces secondary matrix porosity.	min: 1.5%; max: 15%; average: 5%. Inter-dendrite, up to a few mms in size; microporosity. Coated bubble, inter-laminae porosity (1-2 mm). Vertically stacked T2 layers poorly connected because of tight T3 laminae in between.	T2 dendrites (shrubs *sensu* Chafetz & Folk 1984) might be due to biologically induced/influenced precipitation associated with microbial mats of cyanobacteria and sulphide oxidizing bacteria (Chafetz & Folk 1984; Guo & Riding 1994; Guo et al. 1996; Guo & Riding 1998; Chafetz & Guidry 1999; Erthal et al. 2017), even though some authors suggest an abiotic origin (Pentecost 1990; Pentecost & Coletta 2007). T2 dendrites typical of low to moderate energy flat ponds and sub-horizontal pools of terraced slope systems where the flow and turbulence of thermal water are limited and microbial mats drape the pool substrate.
T3 Micrite-microsparite crust boundstone (Figs 6A-B, D)	White dense laminae (0.5-1.5 mm thick) forming mms to cms thick undulated layers; T3 might form stepped microterraced morphologies, sub-horizontal or slightly inclined.	Laminae made of dense leiolitic and clotted peloidal micrite or microsparite. Lamination due to the alternation of micritic layers, dark in colour, and light colour microsparitic layers.	Beds: 1-5 mm up to 5- 11 cm thick (S4). T3 in all cores from 0.5 to 2.5% (S4). Most abundant in core S4, similarly to T1 and T5. T3 vertically alternates with T1 and T2.	Micrite recrystallization in microsparite.	min: 0.1%; max: 5%; average: 2%. Rare inter-laminae porosity.	Possible biologically induced/influenced precipitation of micrite/microsparite crusts in association with microbial mats. In micro-terraced pools and rims of low-angle terraced systems and smooth slopes. T3 drapes T2 and T1 and marks the interruption of T2 and T1 dendrite growth.

Tab. 1 - Description and interpretation of travertine facies. Codes S1-S7 refer to the drilled cores (Figs 2, 4).

Facies	Core description	Petrographic analysis	Thickness and spatial distribution	Diagenetic features	Porosity (% area in thin section)	Depositional processes and environment
T4 Coated gas bubble boundstone to wackestone (Figs 6A-B, D-E)	Light tan to grey, carbonate films isolating rounded hollow pore spaces with spherical to elongated shape (from 0.5 mm to 5 mm in diameter), attributed to coatings around gas bubbles; vertically stacked and welded together bubbles up to 2-3 cm in height. Coated bubbles can occur sparse in carbonate mud matrix (micrite and microsparite) or form frameworks of welded bubbles.	Boundstone to wackestone with sparse bubbles coated by thin layers (5-100 µm) made of leiolitic or peloidal micrite and microsparite. On the outer surface, micron-size T2 micritic or T1 crystalline dendrites can develop. T4 boundstone includes sparse peloids, clots of clotted micrite, intraclasts, rafts and ostracodes.	Beds: 5 mm to 5 cm; maximum thickness: 25 cm (S1). T4 in all cores from 0.5 to 9% (S1). T4 associated with T2, T6, T8, T1, T5. Sparse bubbles in T10. T4-T10 overlying the unconformity T13 with T8. T4 at rim nuclei draped by T1.	Internally and externally lined by cement: 1) equant microsparite to sparite (20-200 µm in size), 2) prismatic scalenohedral cement (100-250 µm).	min: 3%; max: 35%; average: 15%. Intra-bubble, intraparticle porosity several mm-size, isolated and unconnected.	Gas bubbles produced by water turbulence or by microbial metabolic activity. Physico-chemical precipitation (CO_2 degassing) or microbial mediation (Chafetz et al. 1991; Folk & Chafetz 1984; Guo & Riding 1998; Gandin & Capezzuoli 2014; Della Porta 2015; Erthal et al. 2017) in stagnant low-energy ponds and pools of terraced slope systems, nuclei of pool rims of terraced slopes.
T5 Laminated boundstone (Figs 6C, F)	White dense, wavy laminae from tens µms to 2 mm thick. Laminae are undulated, from sub-horizontal to sub-vertical; laminae develop convex-upward morphologies, when laterally welded together. Some of the laminae form irregular porous framework.	Boundstone of laminae (20 µm to 1-2 mm thick, on average 100-300 µm) made of leiolitic and clotted peloidal micrite associated with microsparite (5-20 µm crystal size). Clots of peloidal micrite, rare ostacodes and bivalves. Grey/green internal sediment of ostracod wackestone in interlaminae porosity.	Beds: 2 mm to 13 cm thick, average 4 cm; maximum thickness: tens of cm (S4). T5 in all cores from 0.1 to 7% (S4). T5 vertically alternates with T1, T3, T4. T5 adjacent to rims or slopes with T1.	Cement types lining the inter-laminae porosity and externally the laminae are: 1) limpid equant mosaics of blocky microsparite to sparite (20-100 µm), 2) prismatic scalenohedral cement growing perpendicular to the laminae orientation (up to 0.5 mm thick); 3) locally vadose brown pendant sparite and micrite crusts.	min: 3%; max: 15%; average: 7%. Lens-shaped inter-laminae porosity up to 3 cm wide. In S4 inter-laminae space infilled by siliciclastic silt and ostracode wackestone.	Also labelled as stromatolites (Rainey & Jones 2009) and associated with microbial biofilms (Gandin & Capezzuoli 2014). T5 occurs both in sub-horizontal ponds, pools of terraced slope systems and on inclined slope surfaces associated with fast-flowing T1 crystalline crusts.
T6 Radial coated grain grainstone (Figs 6G-K)	White to light tan mm- to cm-thick layers of sub-rounded coated grains grainstone; in some cases grains welded together to form a framework. Grains show radial coatings around a central nucleus (400-700 µm to 2-8 mm in size) made of micrite or hollow; well sorted, can show both fining and coarsening upward trends (more common). Layers often sub-horizontal to low-angle dipping beds.	Grainstone (microsparite to sparite), rare packstone (microsparite or clotted micrite), to boundstone (grains welded together). Coatings made of turbid, lozenge-shaped crystals (150 µm-1 mm long), similar to T1 crystals with uniform or undulose extinction, arranged radially around a nucleus made of clotted peloidal micrite, intraclast (coated bubbles, rafts), ostracode fragment, or hollow. Less common irregular grains with whole coating or only central area made of clotted peloidal micrite as T2. Ostracodes, bivalves, rare detrital feldspars.	Beds: 5 mm to 20 cm thick, average 4 cm. T6 in all cores from 4 to 25% (S2, S1). T6 can evolve into T2 or T1 dendrites. T6 is associated with T8, T2, T4; T6 adjacent to convex-upward rims, made of T1. T6 vertically alternates with all facies except T9, T11 and T14.	Cement types in interparticle pore space: a) equant blocky mosaics of microsparite (20-150 µm); b) prismatic scalenohedral crystals (400-500 µm long) syntaxial on radial crystal coating; c) preceding pendant cement (100-200 µm irregular droplets) in some cases with Fe oxide. Meteoric vuggy dissolution, micritization and sparitization.	min: 1%; max: 12%; average: 6%. Interparticle and intraparticle porosity from sub-mm to 1 cm in size; trapped gas bubbles and irregular fenestral-like vugs.	Labelled as radial pisoids or spherulites (Folk & Chafetz 1983; Chafetz & Folk 1984; Guo & Riding 1998; Cook & Chafetz 2017) or radiating dendrites (Rainey & Jones 2009) precipitated when disequilibrium is higher than during crystalline dendrite precipitation (Jones & Renaut 1995) or due to CO_2 degassing/evaporation from quiescent water (Rainey & Jones 2009). When T6 grains are transitional into T2 they might represent stagnant conditions and increasing microbially influenced precipitation (cf. Guo and Riding 1998). T6 grains occur in shallow pools of terraced slope systems, in stagnant ponds with reeds and on inclined surfaces of slopes (Della Porta et al. 2017). T6 radial grains are a common fabric of the Tivoli travertines. They have been described in other localities in Central Italy (Della Porta et al. 2017).

Tab. 1 - Description and interpretation of travertine facies. Codes S1-S7 refer to the drilled cores (Figs 2, 4).

Facies	Core description	Petrographic analysis	Thickness and spatial distribution	Diagenetic features	Porosity (% area in thin section)	Depositional processes and environment
T7 Raft grainstone/ rudstone (Figs 7A-C)	White to light grey, grain-supported grainstone to rudstone made of flat sub-mm thick fragmented carbonate plates (rafts).	Individual rafts consist of micritic and microsparitic sub-mm thick films from which prismatic calcite crystals grow perpendicularly. Rafts can act as nucleation substrate for T1 and T2 dendrites oriented upward or downward.	Beds: 0.5 mm to 2 cm thick, 1-10 cm wide lens-shaped. T7 very rare, a few cms in each core. T7 associated with T4, T2, T6; it overlies T11 and T13.	Interparticle space cemented by: 1) equant microsparite; 2) prismatic scalenohedral crystals (200 µm long).	min: 5%; max: 15%; average: 8%. Interparticle porosity up to 1.5 cm in size.	Rafts are films of carbonate precipitated on the surface of pools, at the water-air interface, indicative of stagnant water (Chafetz et al. 1991; Gandin & Capezzuoli 2014; Della Porta 2015) and form rudstone when fragmented. Raft deposits are lens shaped because accumulated in laterally confined ponds.
T8 White coated reed boundstone to grainstone/ rudstone (Figs 7D-G)	White colour, elongated upright vertically oriented or horizontally prostrated carbonate coated stems with rounded cross-section (mostly reeds; diameters 0.5-5 mm, length up to 10 cm), forming boundstone to grainstone/rudstone.	Boundstone of coated reeds in growth position and fragmented reed grainstone/ packstone/rudstone. Coating types: a) rims (0.1-1 mm thick) of leiolitic and clotted peloidal micrite and microsparite, 2) tubes welded by clotted micrite; 3) coating as T1 and T6 crystals (60-150 µm long) arranged radially, followed by clotted micrite and microsparite. Rare *Charophytes* stems, ostracodes, gastropods and rafts. Ostracodes in clotted micrite or in geopetal position filling primary pores.	Beds: 1-24 cm thick. T8 in all cores from 2 to 8.5% (S1, S2, S7). T8 associated laterally with T2, T6, T10 or making the core of rims. T8 alternates with T10 and underlies or overlies T13 detrital layers.	Cement types between or within stem mouldic pores: 1) equant blocky sparite; 2) prismatic scalenohedral cement syntaxial with crystalline coatings (400-800 µm long) and undulose extinction; 3) irregular brown-colour crusts (80-200 µm thick) of pendant cement; locally pyrite in pores.	min: 0.1%; max: 20%; average: 6%. Interparticle, intraparticle and secondary mouldic porosity filled by ostracode grain/packstone and pyrite.	Reeds grow in freshwater or diluted and cooled thermal waters, in marshy flats and form mounds at the base of travertine slopes (marsh pool facies; Guo & Riding 1998). T8 marks the presence of vegetation due to cooled thermal water and mixing with freshwater in distal locations or following subaerial exposure (reeds encrusted by carbonate when the thermal activity resumes; Della Porta et al. 2017). T8 occurs in shallow ponds and terrace pools associated with T6; often overlies the detrital facies T13.
T9 Brown coated reed and *Charophytes* boundstone (Figs 7H-L)	Tan to brown or grey boundstone to grainstone/rudstone formed by carbonate encrusted mm-size *Charophytes* algae and reed stems (1-20 cm in length, 0.5-2 mm in diameters). The dark colour and the abundant presence of *Charophytes* distinguish facies T9 from T8 at the core scale.	Boundstone with irregular framework of clotted peloidal micrite and microsparite precipitated around *Charophytes* and reed stems also in life position. Grainstone consists of peloids, clots of peloidal micrite, coated stems of algae and reeds. Ostracodes (within the clotted peloidal micrite and within primary framework porosity), gastropods, carbonate intraclasts and rafts.	Beds: 5-30 cm thick, up to 50 cm (S1). T9 in all cores from 1 to 11% (S7, S3). At the bottom of S7 it alternates with F5 marls. T9 associated with T10, T11 and T13.	Cement types: 1) pendant micritic cement; 2) equant microsparite to sparite (100-200 µm); 3) scalenohedral prismatic cement (200-800 µm long); 4) fibrous crystal fans. Cement grows around reed moulds and above small rafts. Evidences of early dissolution.	min: 1%; max: 15%; average: 5%. Framework, interparticle and intraparticle porosity (0.5-5 mm, to 2 cm), partly filled by silt, ostracodes and cement.	Physico-chemical and microbially influenced processes. Shallow lacustrine ponds to palustrine environment with terrigenous and freshwater or cooler thermal water input. T9 occurs in the distal S7 core and within an intermediate unit occurring at 15 m depth (from S1 to S5-S6) during which the more distal-like facies prevail across the whole transect.
T10 Clotted peloidal micrite grainstone/ boundstone with *Charophytes* (Figs 8A-C)	Light tan to grey homogeneous texture, mesoscopically appearing as calci-mudstone/wackestone with sparse mm-size vugs and tubular algal stems with 0.2-1 mm diameter, in vertical life position and fragmented, locally associated with raft fragments.	Clotted peloidal micrite grainstone to boundstone made of a) irregular micrite clots (1-0.1 m, mostly 200-300 µm in size) of leiolitic and clotted peloidal micrite (peloids 10-20 µm in diameter, with 10 µm microsparite), partly welded together; b) irregular framework of clotted micrite; c) peloidal grainstone with *Charophytes* stems; d) wackestone with *Charophytes* and ostracodes. Sparse coated gas bubbles, ostracodes, gastropods, filamentous micron-size bacterioform structures.	Beds: 5 mm to 15 cm thick; maximum 70 cm (S3). T10 in all cores from 1 to 18% (S3, S1, S7). T10 at onset of travertine deposition overlying F1. T10 alternates with T2, T6, T8 and T13.	Cement types: 1) equant (20-100 µm) microsparite to sparite irregular rims around micrite clots; 2) equant microsparite/sparite followed by prismatic scalenohedral cement (200-250 µm to 1 mm long); 3) locally pendant vadose cement; 4) rare fibrous cement with undulose extinction. Dissolution of micrite and microsparite.	min: 0.5%; max: 7%; average: 3%. Sub-mm to cm-size sub-horizontal fenestrae-like pores and irregular vugs, interparticle, microporosity, coated gas bubbles porosity.	Facies T10 not differentiated in Tivoli travertines in previous works. Clotted peloidal micrite fabric suggest the influence of microbial mats. T10 represents the onset of travertine deposition in a lacustrine to stagnant pool environment and it occurs in shallow flat ponds.

Tab. 1 - Description and interpretation of travertine facies. Codes S1-S7 refer to the drilled cores (Figs 2, 4).

Facies	Core description	Petrographic analysis	Thickness and spatial distribution	Diagenetic features	Porosity (% area in thin section)	Depositional processes and environment
T11 Brown intraclastic phytoclastic packstone/ grainstone/ rudstone (Figs 8D)	Brown to dark grey packstone/grainstone to rudstone with peloids, angular intraclasts, radial coated grains, vegetation stem fragments (up to a few cms in length, a few mms in diameter).	Packstone: matrix of leiolitic micrite and microsparite. Grainstone: equant blocky sparite as cement. Grains: a) *Charophytes* stems (up to 5 mm long, 0.5 mm in diameter), b) reed fragments (up to 1 cm long); c) irregular clots of peloidal micrite (up to 5 mm in size); d) intraclasts of micrite, coated bubble and rafts, radial coated grains; e) peloids and faecal pellets. Gastropods, bivalves and ostracodes.	Beds: up to 42 cm thick (S2). T11 in all cores from 1 to 12% (S7, S3, S2). T11 associated with T9, both vertically and laterally, and with T10, T8 and T14.	Cement types: 1) equant mosaics of microsparite (10-50 µm) to sparite (100-300 µm); 2) scalenohedral prismatic cement (200-250 µm). Pedogenic alteration, Fe oxides, pyrite infill of voids, desiccation sediment filled fissures.	min: 1%; max: 2.5%; average: 2%. Interparticle, intraparticle, mouldic, fenestral porosity (0.1-3 mm, up to 1.5 cm).	Detrital facies reworking T9 and T10, accumulated in shallow ponds, lacustrine to palustrine environments with terrigenous and freshwater input developing in distal system (S7) and as T9 in an intermediate unit in the succession occurring from core S1 to S6 around 15 m depth during which the more distal-like facies prevail also in proximal zones.
T12 White intraclastic coated grain grainstone/ rudstone (Figs 8E-F)	White/grey grainstone/packstone to rudstone with travertine intraclasts (0.1 mm to 5 cm size, sub-rounded to sub-angular), skeletal fragments and radial coated grains. No sedimentary structures. Intraclasts with micritic to microsparitic carbonate coating.	Grainstone/rudstone with fragments of: clots of leiolitic/clotted micrite (T10), coated bubble (T4), coated reeds (T8), rafts (T7), radial coated grains (T6), clotted peloidal micrite (T2), crystalline dendrites (T1). Ostracodes, gastropods, peloids, rare phosphate grains, fragments of putative filamentous cyanobacteria.	Beds: 0.5-20 cm thick (S3, S4), mostly 5 mm. T12 in all cores from 1 to 6% (S4); it overlies T13 and it is overlain by T6, T2 or T8.	Cement types in interparticle pores: 1) equant blocky microsparite and sparite lined by irregular micrite; 2) prismatic scalenohedral cement. Meteoric dissolution.	min: 2.5%; max: 9%; average: 5%. Interparticle (1-2 mm); fenestral (1.5 cm); intraparticle/ mouldic stems (5 mm).	Detrital grainy sediment due to local reworking of travertine precipitates. Accumulating in pools or inclined surfaces or associated with (preceding or following) periods of subaerial exposure (T13) and inactivity of the hydrothermal system.
T13 Grey intraclastic extraclastic wackestone/ floatstone/ rudstone (Figs 8G-J)	Detrital travertine intraclasts (angular clasts, sub-mm to dms beyond core width) in grey matrix (calci-mudstone/marls); poorly sorted grainstone, packstone, floatstone and rudstone (micrite matrix, or cemented by sparite). T13 associated with terrigenous deposits (claystone and marls with ostracodes with siliciclastic extraclasts). Erosional base; grain-supported textures are at the base and top of T13 layers.	Grainstone, packstone, floatstone, rudstone travertine fragments of T1, T2, T6, T10, T4 and T8. Vadose pisoids; possible coated cyanobacteria filaments. Extraclasts: quartz, mica and K-feldspar crystals. Wackestone to floatstone facies show a dense micrite and microsparite matrix, with clay content. Micrite can show a meniscus fabric followed by cement. Sometimes intraclasts show show dissolution and recrystallization features.	Beds: from 5 mm to 4-7 m thick (S6). T13 in all cores from 1 to 34% (S6, S4). T13 vertically followed or preceded by T12 and T8.	Cement types are: a) equant sparite mosaic; b) scalenohedral prismatic cement; c) vadose pendant cement. They can also follow meniscus-like micrite binding. Alveolar texture related to soils and fungi in between T2 clasts. Sparitization of travertine intraclasts due to meteoric water diagenesis.	min: 1.5%; max: 11.5%; average: 6%. Interparticle, fenestral, vuggy and mouldic porosity (1 mm-2 cm in size)	Lithoclast travertines were associated with pedogenic calcrete and palustrine limestones in fresh-water marshes by (Guo & Riding 1998). T13 represents unconformities: detrital facies due to non deposition and erosion of travertines, related to phases of interruption of the thermal water flow or changes in the flow direction (Gandin & Capezzuoli 2014; Cook & Chafetz 2017). Detrital rubble and terrigenous matrix, soils and vegetation are encrusted by carbonate precipitation when the hydrothermal flow is renewed.
T14 Brown intraclastic phytoclastic packstone/ grainstone to boundstone (Figs 9A-D)	Tan to light brown, grain-supported packstone to grainstone/rudstone to boundstone with reeds, phytoclasts, carbonate intraclasts and siliciclastic detrital grains. Grain size from sub-mm to 1-4 mm. No sedimentary structures..	Packstone to grainstone/rudstone and boundstone with peloids and micrite clots, intraclasts of clotted peloidal micrite, reed and algae fragments coated by crystalline crusts (up to a few 100 µm thick), with wavy patterns and undulose extinction, rarely coated by microsparite to clotted micrite. Ostracodes, bivalves, gastropods, detrital feldspars, phosphate grains. Rare *Charophytes*, possibly diatoms; filamentous tufts of putative calcified cyanobacteria coat plant stems.	Beds: average 6-7 cm thick; 90 cm thick in S4. T14 in all cores 0.1-2%. T14 intercalated with terrigenous marls and siltstone (F5, F6). T14 in S1 to S7 associated with T9, T10, T11.	Coated stems surrounded by irregular micrite coatings followed by equant calcite spar (100-200 µm) and prismatic scalenohedral cement (up to 200 µm in length). Matrix sometimes (in S2 and S3) silicified.	min: 0.5%; max: 4%; average: 2%. Interparticle, intraparticle, mouldic (plant stem, molluscs). Sub-mm size (up to 2 mm, rarely 5 mm).	Palustrine to shallow lacustrine, freshwater pond deposit where plant stems are encrusted by carbonate precipitated in shallow stagnant water with siliciclastic sand and silt input. Occurrence of T14 facies a) in the intermediate phase around 15 m depth associated with T9, T10, T11, T13; and b) in the travertine substrate strata between decametre-thick siliciclastic and volcanoclastic deposits.

Tab. 1 - Description and interpretation of travertine facies. Codes S1-S7 refer to the drilled cores (Figs 2, 4).

Facies	Core description	Petrographic analysis	Thickness, distribution and associated facies	Diagenetic features	Depositional processes and environment
F1 Black to dark grey mudstone (Figs 11A-C)	Black to dark grey, structureless mudstone rich in organic matter.	Organic matter rich clay embedding sparse a) silt- to sand-grade volcanic and carbonate angular clasts and detrital feldspars, b) cubic to framboidal pyrite crystals (0.1-0.5 mm in size) forming mm-size globular aggregates; c) rare carbonate clasts of freshwater tufa or travertine; d) rare gastropods.	0.5-1.5 m. In every core, except S5-S6 below the main travertine unit; overlain by travertine T10 facies with a sharp contact.	Lithified to poorly lithified, cohesive. Alteration cortex around pyrite crystals (Fe hydroxide) and volcanic clasts.	Fine-grained sediment deposited from suspension fall-out in organic matter-rich, stagnant, poorly oxygenated freshwater ponds and wetland marshs.
F2 Green to grey volcanic pyroclastic deposits (Figs 11D-E)	Structureless, matrix-supported deposit consisting of silt to clay-grade volcanic ash matrix with floating minerals and lithic fragments (silt to coarse sand grade).	Mineral grains of pyroxene, feldspatoids, biotite/phlogopite crystals (from Albani Hills volcanic district). There are also deposits with feldspars (Mt Sabatini volcanic district). Vesiculated lapilli, pumices, scorias and lithic clasts also present.	1-6 m. Ubiquitous (except S2), interbedded with F3 and F4, occurring in two distinct depositional events separated by lacustrine facies F5 and F6.	Poorly lithified. Weak to strong argillification of volcanic ash matrix.	Undifferentiated phreatomagmatic pyroclastic flow deposits referable to either the Albani Hills or the Mt Sabatini volcanic districts; in some cases reworking in lacustrine/palustrine depositional environment or altered by pedogenesis due to subaerial exposure.
F3 Grey volcanic pyroclastic deposits with feldspatoids (leucite) (Figs 11F-I)	Structureless, matrix-supported deposit consisting of silt to clay-grade volcanic ash matrix with sparse lithic fragments and minerals, including common mm-size feldspatoid crystals.	Mafic volcanic deposits with pyroxene, feldspatoid (leucite), biotite/phlogopite crystals, lapilli, pumices, scorias and lithic clasts.	A few dms thick in S2, S3, S4, S7; lacking in S5-S6. Up to nearly 2 m in S1 alternating with F2.	Poorly lithified. Weak to strong argillification of volcanic matrix.	F3 similar to and intercalated with F2 pyroclastic deposits but it can be distinguished by the presence of leucite crystals. The F3 pyroclastic deposit can be assigned to the Villa Senni eruptive sequence of the Albani Hills volcanic district (Tuscolano Artemisio phase, dated at 351-357 kyrs; Karner et al. 2001).
F4 Dark grey to green volcanic ash	Fine-grained volcanic ash consisting of lapilli with sparse mineral and lithic fragments.	Mineral grains of pyroxene, feldspar, biotite/phlogopite crystals. Lithic fragments of volcanic rocks, chert and carbonate rocks.	A few cm to 2 m (in S3). In S3, S4, S5-S6, S7, F4 associated with F2 and underlying F5-F6, not penetrated in S1 and S2 boreholes.	Poorly lithified. Weak to strong argillification of volcanic matrix.	Undifferentiated fall out volcanic deposits referable to either the Albani Hills or the Sabatini Mts. volcanic districts. F4 volcanic ash mostly belongs to the oldest volcanic eruptive phase penetrated by the boreholes where F4 underlies lacustrine siltstone and marls. F4 probably accumulated in shallow lacustrine ponds and was affected by pedogenesis during subaerial exposure.
F5 White to light brown marl (Figs 11J-N)	White to light grey/tan marls, argillaceous calci-mudstone and calcareous claystone with mms to a few cms freshwater tufa carbonate clasts.	Presence of organic matter, framboidal pyrite, *Charophytes* carbonate encrusted stems (also fragmented and reworked), rare gyrogonites, diatoms, ostracodes, bivalves, gastropods and sand- to pebble-grade carbonate clasts of possible freshwater tufa and packstone with phosphate nodules, pyroxenes, feldspars, volcanic glass detrital grains.	A few cm to 5-10 m (in S1-S4). Interbedded with F6. Invariably capping and capped by F2, F3, F4 pyroclastites.	Lithified to poorly lithified. Recrystallization of micrite in microsparite. Desiccation cracks; *in situ* brecciation. Silicification (chalcedony and microquartz) associated with rhyzocretion. Prismatic calcite crystals around *Charophytes,* stems. Intraparticle porosity (algae, gastropods) and fissures with equant sparite cement. Bivalve bio-mouldic porosity.	Deposition in shallow lacustrine to palustrine environment with sporadic terrigenous, volcanoclastic and carbonate clast inputs from tributary streams. Desiccation and pedogenetic features testify temporary subaerial exposures. Carbonate mud might be of detrital origin from abrasion of carbonate clasts and bioclasts or derived from settling of micrite precipitated in the water column or due to algal/microbial activity.

Tab. 2 - Description and interpretation of terrigenous and volcanic facies. Codes S1-S7 refer to the drilled cores (Figs 2, 4).

Facies	Core description	Petrographic analysis	Thickness, distribution and associated facies	Diagenetic features	Depositional processes and environment
F6 Green to brown fine sand, silt and clay (Figs 11O, 12A-B)	Green to brown, structureless to parallel laminated very fine sand, silt and clay, locally bearing carbonate coated phytoclasts, charcoal, palaeosols and intercalated with thin beds with volcanic clasts.	Presence of organic matter and remains of vegetation (possible leaves and stems), framboidal pyrite, carbonate encrusted *Charophytes* stems, diatoms, ostracodes, bivalves, gastropods, Fe-stained vadose pisoids and sand- to pebble-grade carbonate clasts of possible freshwater tufa and packstone with phosphate nodules, sparse quartz, pyroxene, feldspar, volcanic glass detrital grains.	A few dms to nearly 3 m (in S3, S5-S6, S7). Interbedded with F5 marls; capping and being capped by F2, F3, F4 pyroclastites.	Unlithified to weakly lithified, cohesive. Desiccation cracks; *in situ* brecciation. Prismatic calcite crystals likely around root casts. Equant sparite precipitated within irregular vugs. Fe oxide coated pisoids with authigenic quartz at the nuclei. Rhyzocretion with Fe oxide staining and authigenic quartz.	F6 alternates with F5 and represents deposition in shallow lacustrine to palustrine ponds with sporadic siliciclastic and carbonate clast inputs from tributary streams that were temporarily exposed to subaerial conditions.
F7 Green sand to laminated sandstone (Figs 12C-E)	Green to brown, structureless or parallel and cross-laminated sandstone and siltstone, locally wacke texture with high amount of clay matrix.	Detrital quartz, feldspar, biotite, carbonate freshwater tufa clasts, vadose pisoids, plant remains.	A few dms. In S5-S6 and S7 only; associated with F6, F9 and F10.	Unlithified to weakly lithified, cohesive.	Deposition by traction by fluvial stream in the Aniene River alluvial plain (exclusive to S5-S6 and S7).
F8 Chaotic mud-supported debris in green clay matrix (Figs 12F-H)	Structureless to chaotic, matrix-supported deposit consisting of sand to pebble-grade carbonate tufa, travertine and volcanic clasts in a silty clayey matrix.	Clasts include volcanic mineral grains (pyroxenes, feldspars), lapilli and carbonate (tufa and travertines) clasts.	0.5-2 m thick in S5-S6 and S3 only; interbedded with F5-F6 deposits and preceding the main travertine unit.	Unlithified to weakly lithified, cohesive. Pedogenic alteration with carbonate encrusted root casts (rhyzocretion made of prismatic calcite crystals similar to *Microcodium*).	Mass transport deposit related to debris flows forming colluvial fans accumulating at the margin of shallow lacustrine environments, reworking travertine clasts, volcanic mineral grains and ash forming silt/clay matrix. Pedogenic features indicate temporary subaerial exposures with formation of soil and vegetation cover.
F9 Polymictic conglomerate (Figs 12I-K)	Moderately sorted, polymictic, clast-supported conglomerates consisting of well-rounded to sub-angular clasts (0.2-2 cm size) of substrate rocks in a fine-grained terrigenous matrix (fine sand to mud-grade) and carbonate cement. Clasts can show imbrication.	Clasts of marine limestones (wackestone with Cenozoic planktonic foraminifers, coated grain grainstone) and chert fragments deriving from the Mesozoic-Cenozoic substrate rocks, sandstone and volcanic deposits.	A few dms recovery in an interval 6 m thick. At the base of S7 and below the main travertine unit in S5-S6.	Weakly to strongly lithified with clay or marly matrix or sparite cement (pendant, meniscus and equant calcite).	Bed load traction and deposition by fluvial streams having the catchment area in the surrounding marine carbonate-dominated ridges. Terraced fluvial deposits of the Aniene River (only in S5-S6 and S7).
F10 Grey/green cross-laminated sandstone (Figs 12L-N)	Tan to grey/green, medium to coarse sand to cemented cross-laminated sandstone ranging from litharenite to lithic arkose and wacke.	Lithic fragments of Mesozoic-Cenozoic marine carbonate substrate rocks and chert; volcanic fragments and minerals (pyroxenes, feldspars).	A few dms to nearly 1 m. In S7 only, associated with F7 and F9.	From unlithified to well-cemented; lithified intervals preserve interparticle porosity. Cement: vadose pendant and meniscus equant to bladed sparite. In some cases clay Fe oxide matrix is present.	Traction deposition by fluvial stream. Terraced fluvial deposits of the Aniene River (only in S7).

Tab. 2 - Description and interpretation of terrigenous and volcanic facies. Codes S1-S7 refer to the drilled cores (Figs 2, 4).

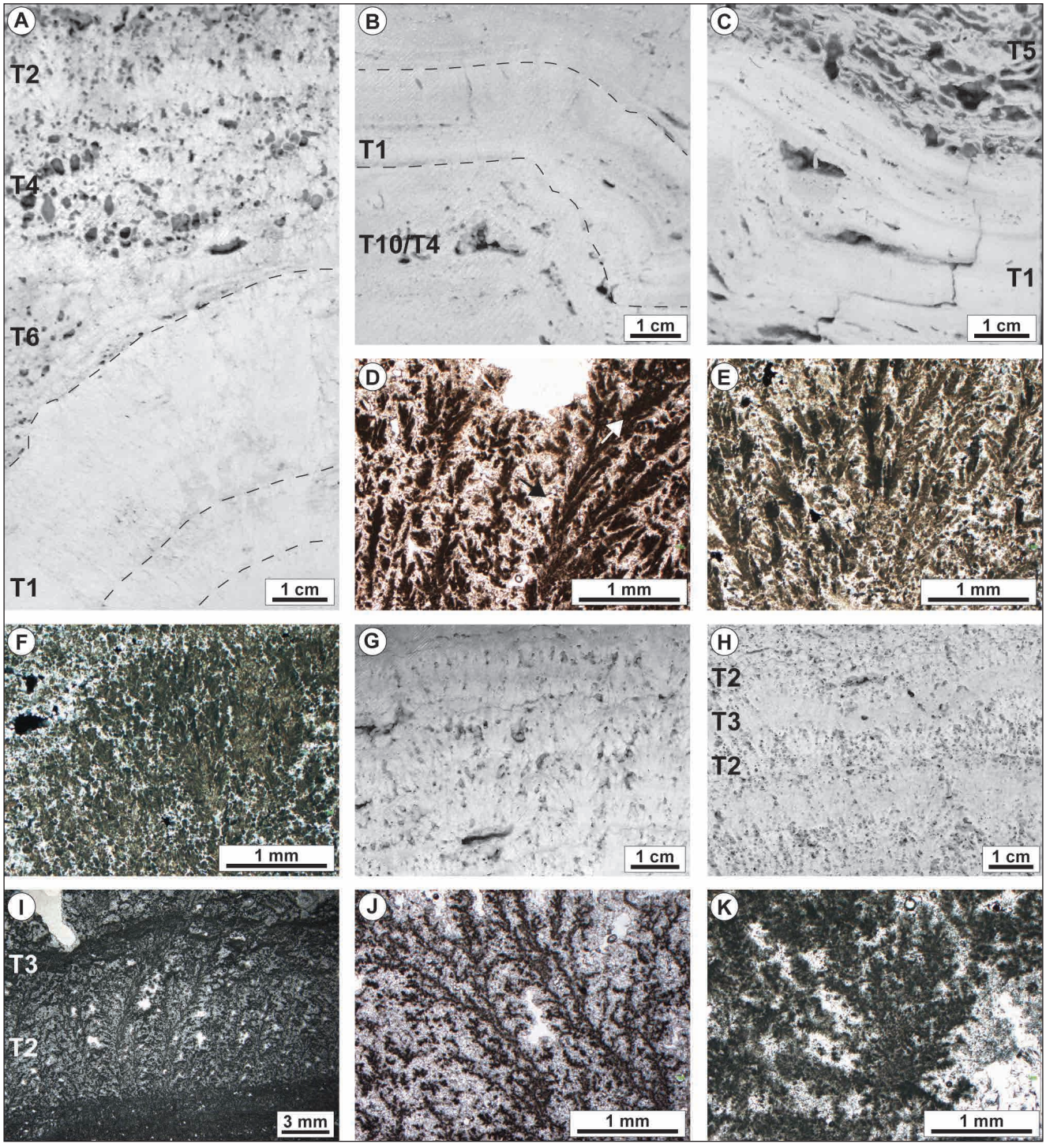

Fig. 5 - Core slab photos and photomicrographs of travertine facies T1 and T2. A) Core slab of terraced slope (S2) showing a decimetre-size pool rim made of centimetre-thick crystalline dendrites (T1) overlain by the adjacent pool facies including radial coated grain grainstone (T6), coated bubble boundstone (T4) and clotted peloidal micrite dendrites (T2). B) Core slab image of a few centimetre in size, rounded pool rim from S4 terraced slope made of crystalline dendrites (T1) with the nucleus made of clotted peloidal micrite grainstone (T10) and irregular coated gas bubbles (T4). C) Core slab image of a smooth slope (S4) with inclined layers (up to 40° in core) of crystalline dendrites (T1) overlain by laminated boundstone (T5). D) Photomicrograph of T1 dendrites made of branching lozenge-shaped turbid crystals (white arrow) surrounded by equant sparite (black arrow). E) Crossed polarizer image of T1 crystalline dendrite crystals showing undulose extinction. F) Photomicrograph in crossed polarisers of a rounded rim made of fan-shaped crystalline dendrites. G) Centimetre-thick superimposed layers of dendrites made of clotted peloidal micrite (T2) from core S2. H) S2 core slab of centimetre-thick layers of clotted peloidal micrite dendrites (T2) alternating with millimetre-thick, dense micrite/microsparite crusts (T3). I) Photomicrograph of centimetre-thick layers of clotted peloidal micrite dendrites (T2) alternating with dense micrite crusts (T3). J) Branching dendrites made of clotted peloidal micrite (T2) with the inter-branching space filled by equant sparite. K) Fan-shaped clotted peloidal micrite dendrites (T2) with the inter-branching space filled by equant sparite.

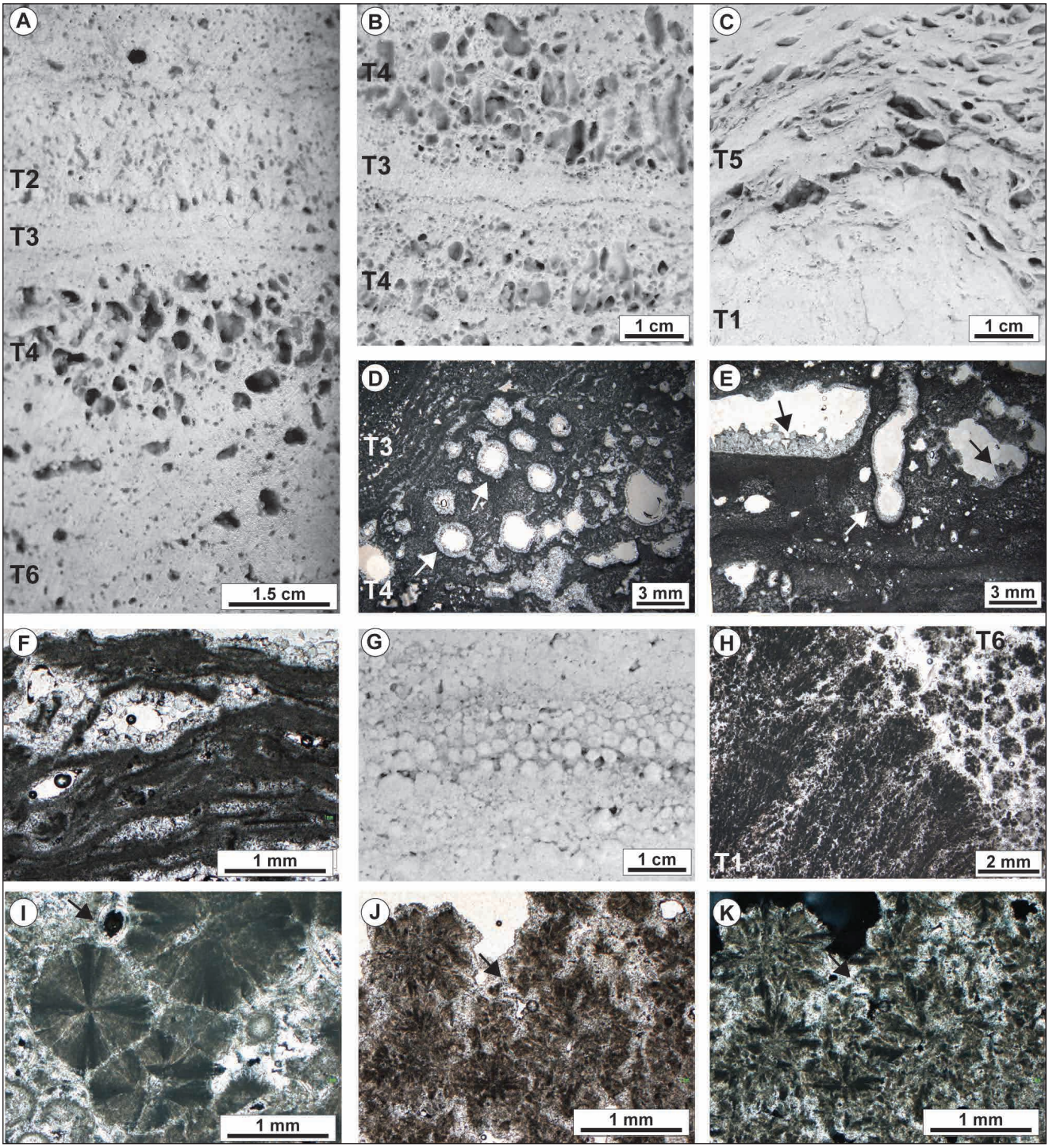

Fig. 6 - Core slab photos and photomicrographs of travertine facies T3 to T6. A) S1 core slab showing centimetre-scale T2 clotted peloidal micrite dendrites, T3 dense micrite crust, T4 coated gas bubble boundstone and T6 radial coated grain grainstone. B) Core slab (S1) with T3 dense micrite crust separating coated bubble boundstone (T4) with vertically elongated and amalgamated vertically stacked carbonate-coated gas bubbles. C) Laminated boundstone T5 from core S2 terraced slope overlying T1 crystalline dendrites. D) T4 coated gas bubbles embedded in clotted micrite overlain by T3 micrite laminae. Bubble porosity is lined by prismatic calcite cement with scalenohedral terminations (white arrows). E) Clotted peloidal wackestone with sparse coated bubble forming an elongated structure due to the vertical amalgamation of more bubbles (white arrow). Porosity is lined by prismatic calcite cement with scalenohedral terminations (black arrows). F) Laminated boundstone T5 with lens-shaped inter-laminae pores partially filled by sparite cement. G) S3 core slab image of radial coated grain grainstone T6 with fining upward trends. H) Photomicrograph of pool rim adjacent to a pool with T6 radial coated grain grainstone (core S1). I) Image in crossed polarizers of radial grains made of fan-shaped crystals with undulose extinction. One ostracode is marked by a black arrow. J) and K) Parallel and crossed polarizers image of T6 radial grains made of lozenge shaped turbid crystals similar to those that compose the T1 crystalline dendrites. Grains are surrounded by limpid blocky sparite (black arrows). Some interparticle porosity is still present.

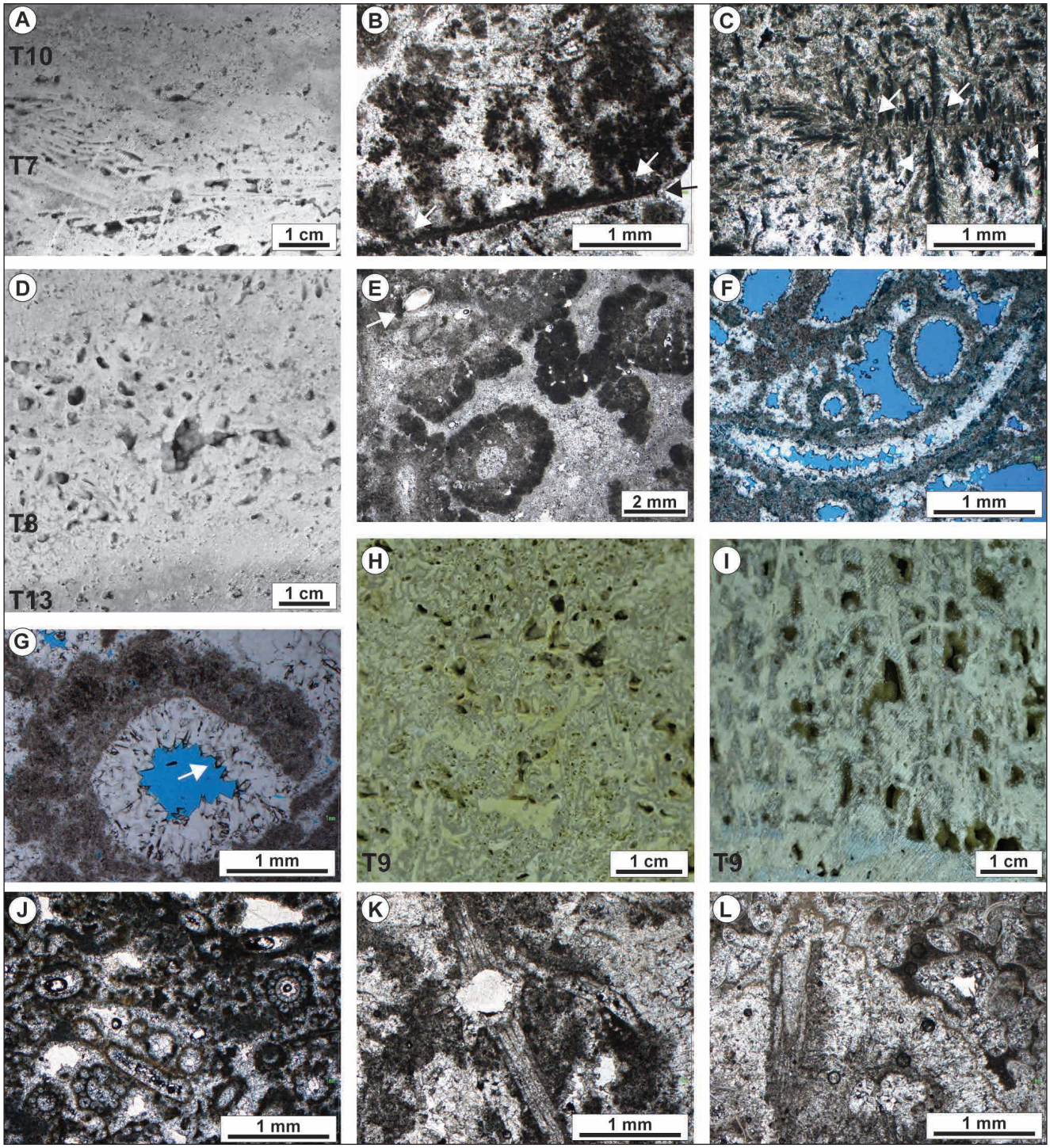

Fig. 7 - Core slab photos and photomicrographs of travertine facies T7 to T9. A) T7 raft rudstone from a pool at the base of core S6. B) Photomicrograph of micritic raft (black arrow) on which clotted peloidal mcirite dendrites nucleated (white arrows). C) Crossed polarisers image of micritic raft overlain and underlain by crystalline dendrites (white arrows). D) S2 core slab image showing T8 coated reed boundstone overlying a layer of T13 intraclastic extraclastic wackestone with grey matrix indicative of subaerial exposure and travertine erosion. E) Photomicrograph of reeds coated by micrite followed by crystal fans with turbid appearance. Ostracodes are embedded in the upper left corner (white arrow). F) Reeds coated by clotted peloidal micrite lined by equant sparite and preserved intraparticle porosity. G) Coated reed lined internally by prismatic calcite crystals with scalenohedral terminations (white arrow). H) S7 core slab of T9 brown coated reed and *Charophytes* boundstone with framework porosity infilled by terrigenous clay. I) S2 core slab image of T9 *Charophytes* boundstone. J) Photomicrograph of T9 micrite coated *Charophytes* stem boundstone surrounded by limpid equant sparite cement. K) Longitudinal section of T9 *Charophytes* stem surrounded by micrite followed by fibrous cement. L) T9 *Charophytes* stem surrounded by micrite followed by fibrous sparite cement overlain by ostracode packstone (upper right corner).

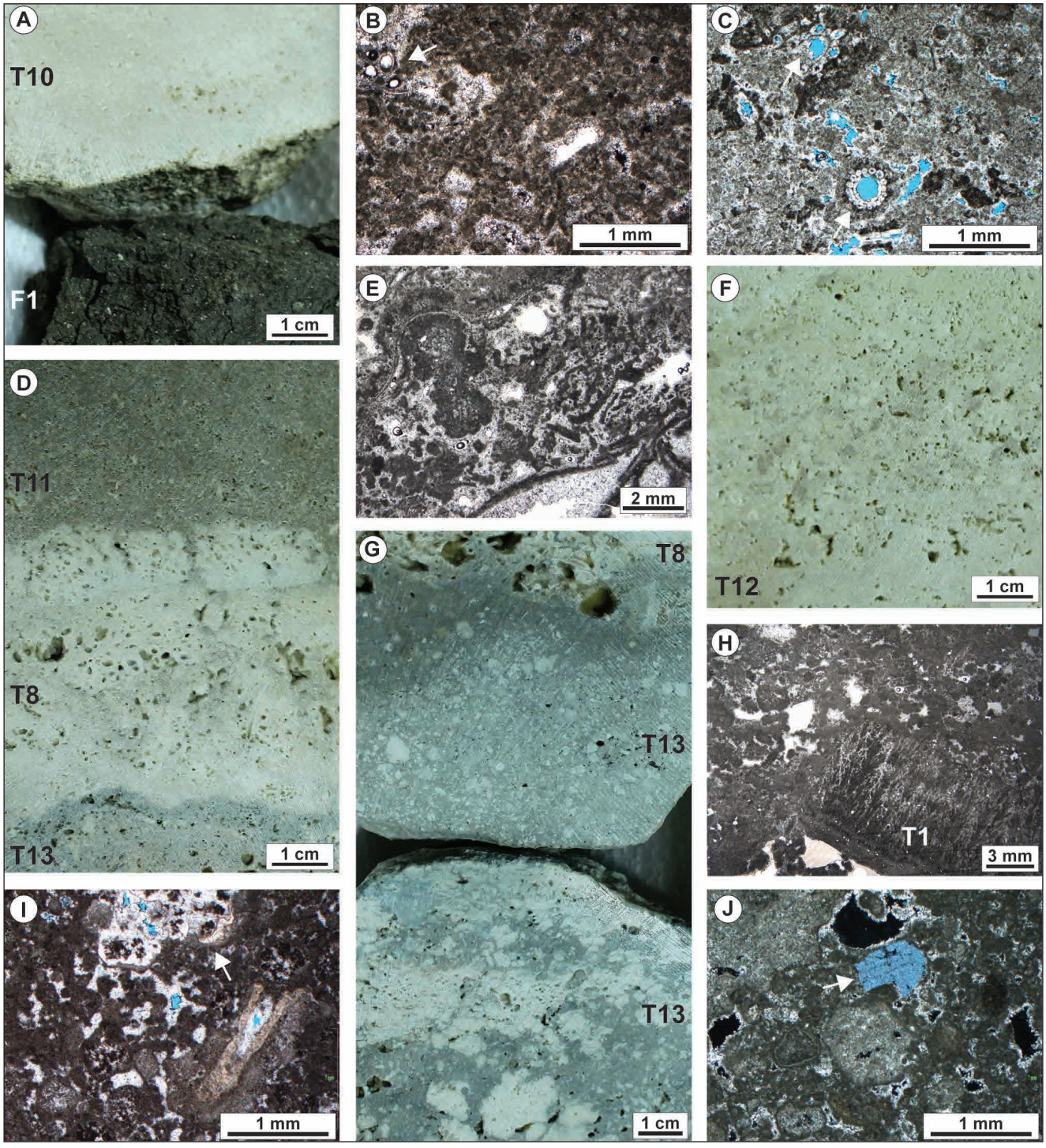

Fig. 8 - Core slab photos and photomicrographs of travertine facies T10 to T13. A) S1 core showing the contact between the first travertine deposit (T10 clotted peloidal micrite grainstone/boundstone with *Charophytes*) overlying F1 black mudstone. B) Photomicrograph of T10 clotted peloidal micrite grainstone/packstone with ostracodes (white arrow). C) T10 packstone with sparse *Charophytes* stems (white arrows). D) S2 core slab with T13 grey intraclastic extraclastic wackestone overlain by T8 coated reeds followed by T11 brown intraclastic phytoclastic packstone/rudstone. E) Photomicrograph of T12 white intraclastic coated grain grainstone/packstone with raft fragments. F) S4 core slab showing T12 intraclastic coated grain grainstone/packstone to rudstone. G) S1 core slab showing T13 wackestone to floatstone with centimetre-size travertine angular intraclasts in grey micrite-terrigenous matrix overlain by T8 coated reed boundstone. H) T13 intraclastic travertine packstone/rudstone with angular clast of T1 crystalline dendrites. I) T13 peloidal intraclastic packstone to grainstone with coated reeds and clasts with pendant calcite vadose cement (white arrow). J) T13 intraclastic grainstone to packstone with feldspar detrital grain (white arrow) and vuggy porosity lined by sparite.

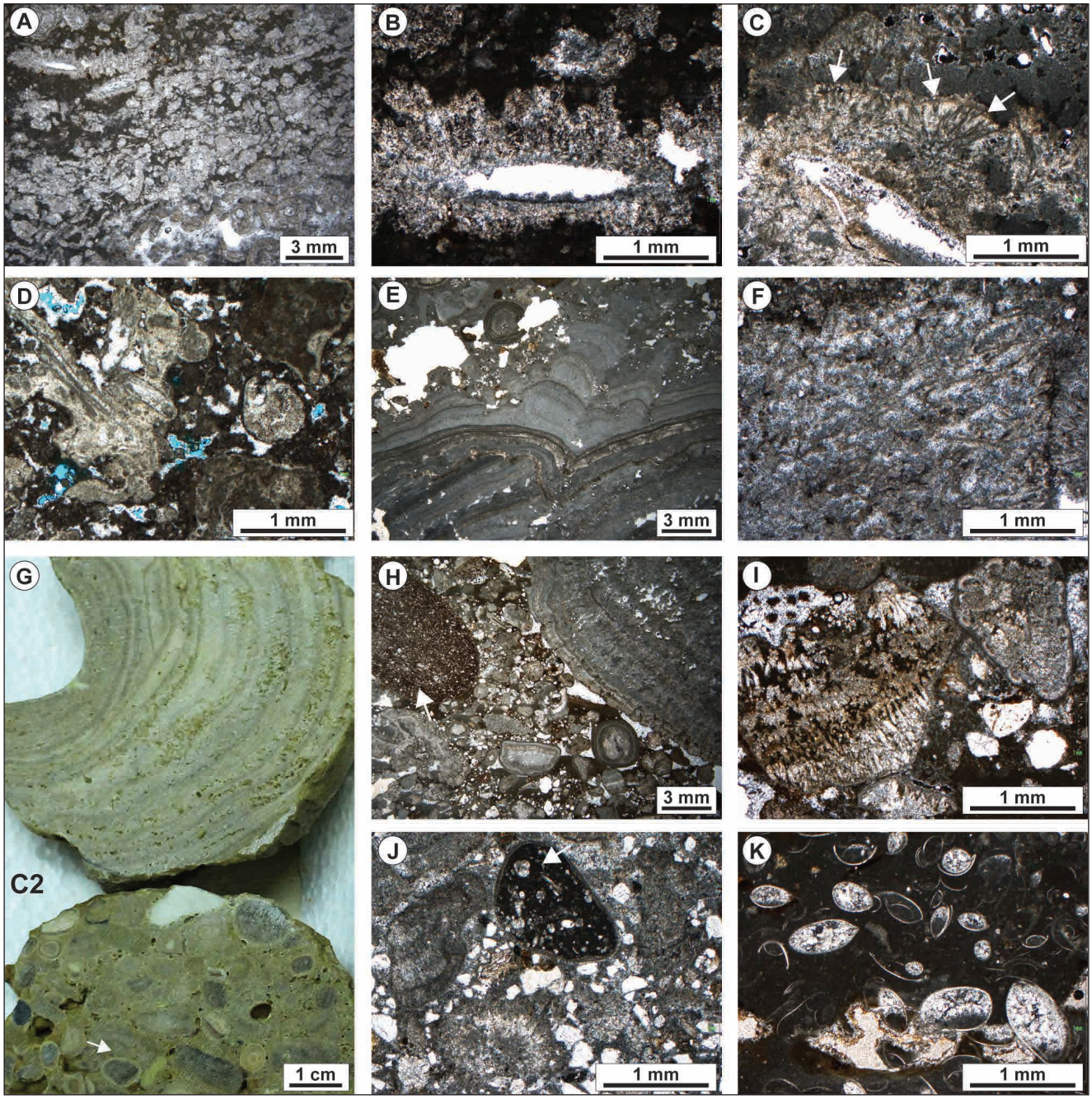

Fig. 9 - Core slab photos and photomicrographs of travertine facies T14 and post-travertine sediment filling C1 and C2. A) T14 phytoclastic packstone with plant stems coated by prismatic calcite spar. B) Close-up view of the prismatic crystals coating vegetation stems. C) Plant stem coated by calcite crystal fans embedding micritic tubular structures probably representing calcified cyanobacteria (white arrows). D) T14 intraclastic phytoclastic packstone/grainstone with preserved interparticle porosity (in blue). E) Micritic columnar laminae associated with speleothem structures filling karstic caves in S7 (C2). F) Tubular structures that might be attributed to filamentous cyanobacteria in C2. G) Cave fill in core S7 (C2) consisting of columnar cementstone (speleothems) and extraclastic to pisoidal (white arrow) packstone to rudstone indicative of vadose deposition within a cave. H) Extraclastic pisoidal rudstone with Cenozoic planktonic and benthonic foraminifer wackestone (white arrow) from the mountain ridges surrounding the AAB. I) Extraclastic/intraclastic pisoidal rudstone with detrital quartz and T1 crystalline dendrite clast. J) Extraclastic pisoidal rudstone with Cenozoic planktonic foraminifer wackestone at the nuclei of pisoids (white arrow) deriving from the mountain ridges surrounding the AAB. K) Ostracod wackestone/packstone (C1) infilling centimetre to decimetre-size vugs within the travertine.

ranges from 1 to 12 %. The coated bubble boundstone (T4) is characterized by high porosity up to 25 % and low permeability. Facies T6 samples have uniform porosity (6-8 %) but variable permeability values. Facies T8, T10 and T14 show a rapid increase in permeability at low increments of porosity. Facies T4 and T13 display limited increase in permeability despite the rapid increase in porosity.

Travertine carbon and oxygen stable isotopes

The measured carbon and oxygen isotope values (Fig. 15) are summarized in Table 3 as core averages, excluding the detrital travertine facies T13, and as averages of each facies type, cement and sediment infill categories. The carbon and oxygen isotope values are fairly uniform with average $\delta^{13}C$ per core ranging from 9.2 ‰ to 10.1 ‰ and $\delta^{18}O$ from -6.8 ‰ to -6.1 ‰, with standard deviations of 0.5-1.1 ‰ for $\delta^{13}C$ and 0.5-0.8 ‰ $\delta^{18}O$. The matrix of facies T13 (intraclastic/extraclastic wackestone to floatstone/rudstone) yields values similar to the precipitated travertines with average $\delta^{13}C$ 9.4 ‰ and $\delta^{18}O$ -6.7 ‰. Facies T14, the brown intraclastic phytoclastic packstone/grainstone to boundstone with *Charophytes* algae occurring intercalated with terrigenous deposits below the main travertines, shows a wide range of $\delta^{13}C$ values ranging from 10.4 ‰ to the most depleted values of 5.6-2.6 ‰. The equant to prismatic cements lining the pores provide slightly lighter values than the hosting travertines with average $\delta^{13}C$ 8.7 ‰ and $\delta^{18}O$ -7.2 ‰. The C1 ostracode wackestone sediment fill has average $\delta^{13}C$ 8.1 ‰ and $\delta^{18}O$ -6.7 ‰ and the C2 concentric columnar carbonate crusts provide average lighter $\delta^{13}C$ of 4.7 ‰ and similar average $\delta^{18}O$ of -6.4 ‰.

Facies abundance per core

Table 4 reports the abundances of the distinguished facies types expressed as cumulative thickness in each core and as facies thickness percentages relative to the whole core and main travertine unit. Core thickness includes also the non-recovered portions that might have been lost during drilling or represent post-travertine karstic caves. The most abundant travertine facies is the T6 radial coated grain grainstone, in particular in cores S1 and S2 (Fig. 16A), followed by the detrital intraclastic extraclastic wackestone to rudstone (T13), T2, T8 and T10 (Fig. 16B). Facies T1 crystalline dendrite cementstone and T5 laminated boundstone are not very common but they show the maximum thickness in core S4 (Fig. 16). Facies T2 clotted peloidal micrite dendrite and T4 bubble boundstone are ubiquitous but the thickest in cores S1 and S2. Facies types with carbonate coated reeds and *Charophytes* (T8-T11) are more frequent and the thickest in cores S2, S3 and S7. The terrigenous and volcanic deposits form the substrate of the travertine units in cores S1 to S4 (Table 4, Figs 4, 16A), whereas in the southernmost core S7, which is located close to the present-day Aniene River, terrigenous deposits (facies F5-F10) occur also intercalated with the travertines (Fig. 16B). Sandstone and conglomerate facies (F7-F10) occur exclusively in the southern cores S5-S6 and S7 (Fig. 16). In all the cores, except S4 and S5-S6, facies F1 black mudstone represents the first deposit underlying the travertines (Fig. 4).

Travertine stratal geometries

The upper portion of the analysed cores crops out in the quarries allowing to combine the core stratigraphy with the stratal geometries visible in the saw-cut quarry walls. S1 quarry walls show the predominance of horizontal to gently inclined (around 1-2°), centimetre-thick beds dipping towards the E and SE, alternating with numerous T13 detrital travertine and claystone beds (Fig. 17A-B). The travertine strata overlying T13 beds show locally low-angle onlap terminations against the T13 surfaces (Figs 17A, C). Centimetre-size micro-terraces and rare decimetre size pool rims formed by the T1 crystalline dendrite cementstone facies are visible both in the core and quarry (Figs 5A-B, 17B-C). In quarry S2, strata are gently inclined towards the W and SW (Fig. 17D) and, similarly to S1, the upper 18 metres show sub-horizontal to gently inclined parallel beds with locally centimetre-size micro-terraces and rare decimetre size pool rims, dominated by T6, T2, T13, T8 and T10 facies. In S3 quarry, bedding is predominantly horizontal (Figs 17E-G); however, core S3 shows evidences of a micro-terraced system between 2 and 4 m depth and 16-20 m depth where a few layers of the T1 crystalline dendrites are present forming rare decimetre-size rims. In both S4 core and quarry, the upper part, between 0 and 8 m depth in the core, consists of sub-horizontal layers of T10 and T6 facies. The lower part, at depths of 13-26 m in core S4, is dominated by T1 crystalline dendrites and T5 laminated boundstone, associated with T6 radial coated grain grainstone, forming centimetres thick layers dipping 5-30° towards the S and E (Figs 17H, 18A). Travertine beds show onlap stratal terminations against the T13 beds dipping south- and eastwards (Figs 17H, 18A). In quarry S5-S6 the travertine deposits dip towards the S and E, from a few degrees to 40°, forming units pinching out westward with onlap stratal terminations towards the W (Figs 18B-D). In S7, bedding appears

to gently dip towards the S, E and W and travertine units pinch out towards the N and E (Fig. 18E).

Interpretation

Facies associations and depositional environments

The fourteen distinguished travertine facies composing the investigated cores (Figs 4, 19 in Appendix 1) are interpreted with respect to the environment of deposition and precipitation processes (Table 1) integrating information from published travertine studies (cf. Chafetz & Folk 1984; Folk et al. 1985; D'Argenio & Ferreri 1986; Jones & Renaut 1995; Guo & Riding 1992, 1994, 1998, 1999; Chafetz & Guidry 1999; Pentecost 2005; Jones & Renaut 2010; Anzalone 2008; D'Argenio et al. 2008; Gandin & Capezzuoli 2014; Claes et al. 2015; Della Porta 2015; Croci et al. 2016; Anzalone et al. 2017; Cook & Chafetz 2017; Della Porta et al. 2017; Erthal et al. 2017). The travertine facies can be grouped into four facies associations indicative of specific depositional environments. 1) Travertine facies precipitated by fast-flowing thermal water on smooth slopes (dipping from 5° up to locally 40°) and on rounded rims and walls of pools in terraced slopes include T1 crystalline dendrite cementstone, T5 laminated boundstone, and T6 radial coated grain grainstone. 2) Travertine facies precipitated from slow-flowing to stagnant thermal water in sub-horizontal or microterraced (centimetre-size terraces) ponds and pools of terraced slopes are T2 clotted peloidal micrite dendrite, T3 micrite-microsparite crust, T4 coated gas bubble, T5 laminated boundstone, T6 radial coated grain grainstone, and T10 clotted peloidal micrite grainstone/boundstone. 3) Travertine facies consisting of carbonate coated vegetation and algae (T8 white coated reed, T9 brown coated reed and *Charophytes* boundstone, T10 clotted peloidal micrite grainstone/boundstone with *Charophytes*, T11 brown intraclastic phytoclastic grainstone/packstone to rudstone, T14 brown intraclastic phytoclastic packstone/grainstone to boundstone) accumulated in sub-horizontal ponds. 4) Detrital travertines indicative of erosion due to interruptions or deviations of the thermal water flow and exposure to meteoric diagenesis and pedogenesis include facies T12 white intraclastic coated grain grainstone/rudstone and T13 grey intraclastic extraclastic wackestone to floatstone/rudstone. Travertines with carbonate coated reeds may either overlie or underlie detrital travertines (T13) related to subaerial exposure or they are associated with siliciclastic deposits (core S7; Figs 4, 19 in Appendix 1). Reed travertines were interpreted as marsh pond facies deposited in depressions in distal settings from the hydrothermal vents and in rain-influenced and cooled thermal water (Guo & Riding 1998). *Charophytes* seem to be absent in active hydrothermal travertine systems with temperature ranging from 37 to 65°C from various localities in Central Italy (e.g., Saturnia, Bagni San Filippo, Bullicame). They have been, however, described associated with gastropods and ostracodes in mudstone from distal palustrine ponds or overlying erosional surfaces developed during

Fig. 10 - Diagenetic features in travertines. A) and B) Parallel and crossed polarizers images of facies T13 extraclastic/intraclastic grainstone with travertine intraclasts lined by meteoric pendant vadose cement (white arrows) followed by phreatic prismatic calcite cement with scalenohedral terminations (black arrows). C) Laminated boundstone from the smooth slope in S4 core with millimetre-thick meteoric vadose laminated pendant cement hanging from the lower part of the laminae (white arrows) followed by scalenohedral meteoric phreatic cement (black arrows). D) Facies T8 coated reeds from core S3 showing millimetre-thick brown laminated and bladed meteoric vadose pendant cement (white arrows) surrounded by equant sparite of meteoric phreatic diagenesis (black arrows). E) Close-up view of the pendant cement in panel D meteoric vadose cement (white arrows) surrounded by equant sparite of meteoric phreatic diagenesis (black arrow). F) Clotted peloidal micrite dendrites (T2) overlain by a first equant cement crust (c1) followed by ostracode wackestone (O) overlain by scalenohedral cement (c2) and blocky sparite (c3). G) Crossed polarizers image of T4 coated bubble internally lined by meteoric phreatic prismatic cement with scalenohedral terminations (white arrow). H) and I) Parallel polarized light and cathodoluminescence image of T2 clotted peloidal micrite dendrite and surrounding equant sparite cement. The cement is non luminescent (c) whereas the dendrites show a weak luminescence (d). J) and K) Parallel polarized light and cathodoluminescence image of T2 clotted peloidal micrite dendrite where the clotted micrite is non luminescent (a) or weak luminescent (b) with the scalenohedral cement showing a growth phase with bright orange luminescence (c). L) T1 crystalline dendrites with turbid crystals internally replaced by limpid sparite (black arrows). M) Micritic dendrites internally replaced by limpid sparite probably during meteoric diagenesis (black arrows). N) Clotted peloidal micrite showing internal microporosity evidenced by blue epoxy. The scalenohedral cement crystals are partially dissolved with internal porosity. O) Alveolar texture (black arrows) within T2 clotted peloidal micrite dendrite indicative of soil formation during subaerial exposure.

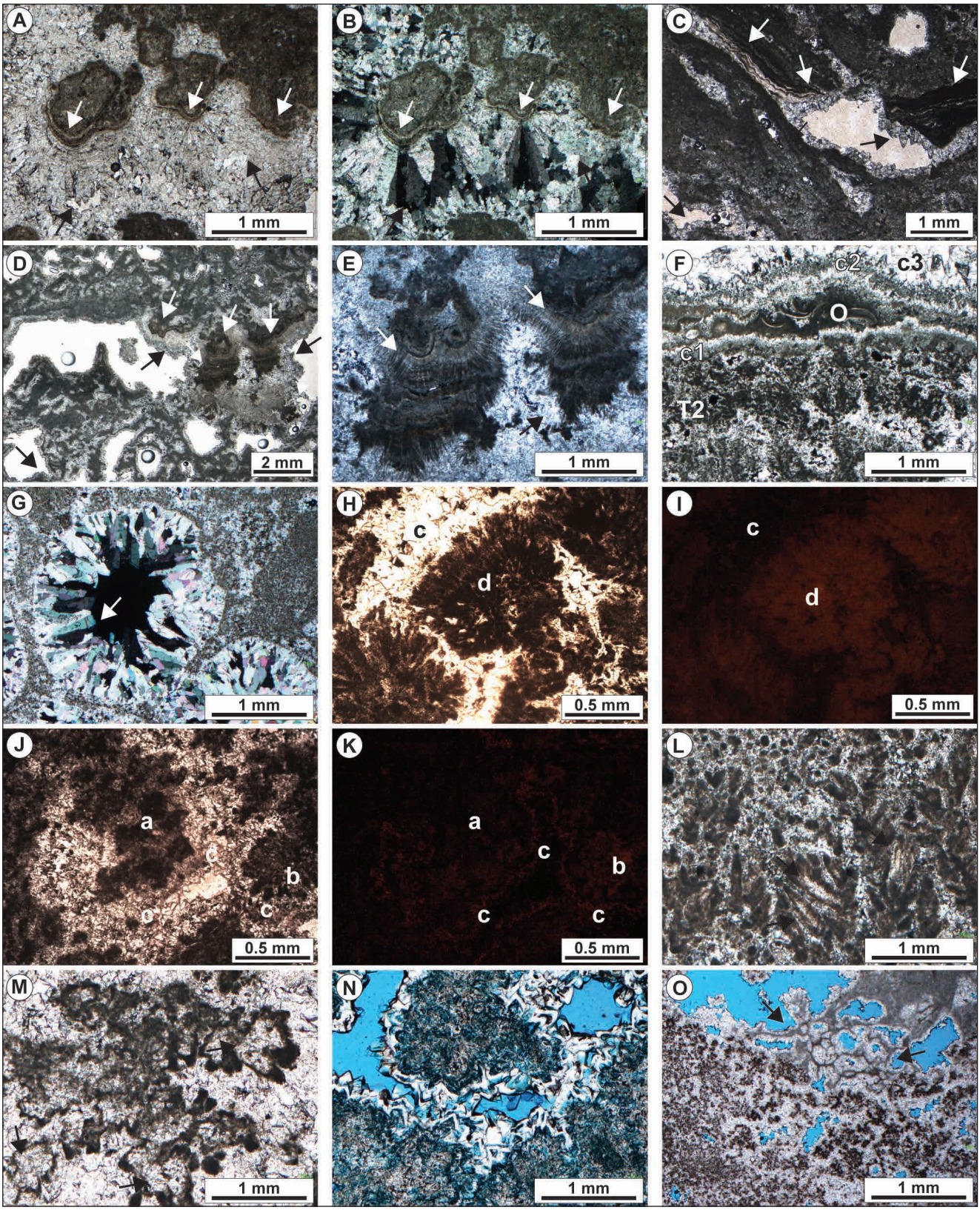

pauses or diversions of thermal water (Gandin & Capezzuoli 2014; Della Porta et al. 2017). *Charophytes* thrive in present-day warm-springs with water temperature up to 25°C in Arctic Svalbard where the warmest air temperatures are lower than 5°C (Langangen 2000). *Charophytes* are very common in freshwater lakes at temperate latitudes (Pelechaty et al. 2013), where they grow at shallow depths (2-10 m) within the photic zone (Murru et al. 2007; Gierlowski-Kordesch 2010;

Apolinarska et al. 2011), in alkaline oligo-mesotrophic water (Kufel & Kufel 2002; Pentecost et al. 2006; Apolinarska et al. 2011; Rey-Boissezon & Auderset Joye 2015).

In terms of processes, travertine precipitation appears mostly driven by physico-chemical parameters (CO_2 degassing of thermal water while flowing and evaporation) but the ubiquitous presence of organic substrates (microbial mats, algae and vegetation) in present-day hydrothermal systems (cf. Pentecost & Tortora 1989; Allen et al. 2000; Reysenbach et al. 2000; Fouke et al. 2003; Norris & Castenholz 2006; Costa et al. 2009; Di Benedetto et al. 2011; Fouke 2011; Okumura et al. 2012; Sugihara et al. 2016) suggests that there must also be a component of biologically induced and influenced carbonate precipitation. Carbonate precipitation appears to result from a continuum of interacting physico-chemical and biologically influenced, microbially mediated processes (cf. Della Porta 2015 and references therein). The biogenic contribution to carbonate precipitation might be dominant in low-energy, slow-flowing to stagnant water in shallow ponds where clotted peloidal micrite is the common product (cf. Guo & Riding 1994; Erthal et al. 2017), rather than in turbulent fast-flowing sloping settings where abiotically driven precipitation results in predominant crystalline dendrite cementstone. The presence of embedded organic matter could be the cause of the weak luminescence of the travertine T2 clotted peloidal micrite precipitates (Figs 10H-K). SEM analysis (Fig. 13) showed the presence of organic substrates, possible biofilm extracellular polymeric substances (EPS) and filamentous, coccoid and dumb-bell microbial bodies as observed in other travertine deposits (Chafetz & Folk 1984; Folk 1993; Guo & Riding 1994; Jones & Peng 2014a; Claes et al. 2015; Erthal et al. 2017). Clotted peloidal micrite precipitates consist of nanometre scale sub-spherical carbonate grains that might represent amorphous calcium carbonate (ACC) as identified in studies on spring and lacustrine carbonates (Jones & Peng 2012, 2014abc; Della Porta 2015 and references therein).

The terrigenous deposits (Fig. 19 in Appendix 1; Table 2) underlying the travertines and, in the southernmost core S7 also alternating with travertine strata, can be interpreted as being deposited in: a) shallow freshwater lacustrine to palustrine ponds and marshes with variable contribution of carbonate and siliciclastic sediment and organic matter (F1 mudstone, F5 marl, F6 fine sand, silt and clay); and b) colluvial fan, alluvial and fluvial depositional environments related to the Aniene River (F7 sand to laminated sandstone, F8 mud-supported debris, F9 polymictic conglomerates; F10 cross-laminated sandstone). The lacustrine and alluvial plain deposits (facies F5, F6) from core S1 to S5-S6 are lateral southward to the fluvial sandstone (F9) and conglomerate (F10) in the distal core S7. The F1 metre-thick mudstone, rich in organic matter and pyrite, is likely indicative of lacustrine restricted and dysoxic setting preceding the onset of travertine deposition.

The volcanic and volcaniclastic deposits (facies F2, F3, F4) must be related to the phreatomagmatic pyroclastic deposits of the Albani Hills and Sabatini Mts. volcanic districts (De Rita et al. 1995). There are two identified volcanic pyroclastic units separated by lacustrine alluvial plain deposits (Fig. 19 in Appendix 1): a) the lower volcanic unit includes contributions from both the Albani Hills and Sabatini Mts. volcanoes based on the mineral content (Table 2); b) the upper younger volcanic deposit might be attributed to the last eruption of the Tuscolano Artemisio phreatomagmatic phase of the Albani Hills volcano

Fig. 11 - Core slab photos and photomicrographs of terrigenous and volcanic facies F1 to F5. A) Facies T11 overlying facies F1 black mudstone at the base of the travertine deposit in core S3. B) and C) Parallel and crossed polarizers images of the F1 black mudstone in core S1 showing the clay matrix and aggregates of framboidal pyrite (white arrows). D) Photomicrograph of F2 volcanic pyroclastic deposit. E) S5-S6 core image of F2 green to grey volcanic pyroclastic deposit. F) S1 core image of grey volcanic pyroclastic deposit with feldspatoids (leucite; black arrows). G) F3 volcanic pyroclastic deposit with leucite (white arrow), pyroxenes and volcanic glass. H) and I) Parallel and crossed polarizers image of F3 volcanic pyroclastic deposit with pyroxenes and K-feldspars embedded in an aphanitic glass matrix. J) S3 core image of white to light brown marl with millimetre to centimetre-size carbonate lithoclasts (black arrows). K) Pennate diatoms (white arrows) in the matrix of facies F5 marls. L) F5 lacustrine skeletal wackestone with ostracodes (o) and gastropods (g). M) F5 lacustrine marl with bivalves (b) and *Charophytes* stems (c). N) F5 marl with chalcedony and microquartz tubular structures probably associated with plant roots and palaeosols. O) Photomicrograph of F6 green to brown fine sand, silt and clay with bivalve shell.

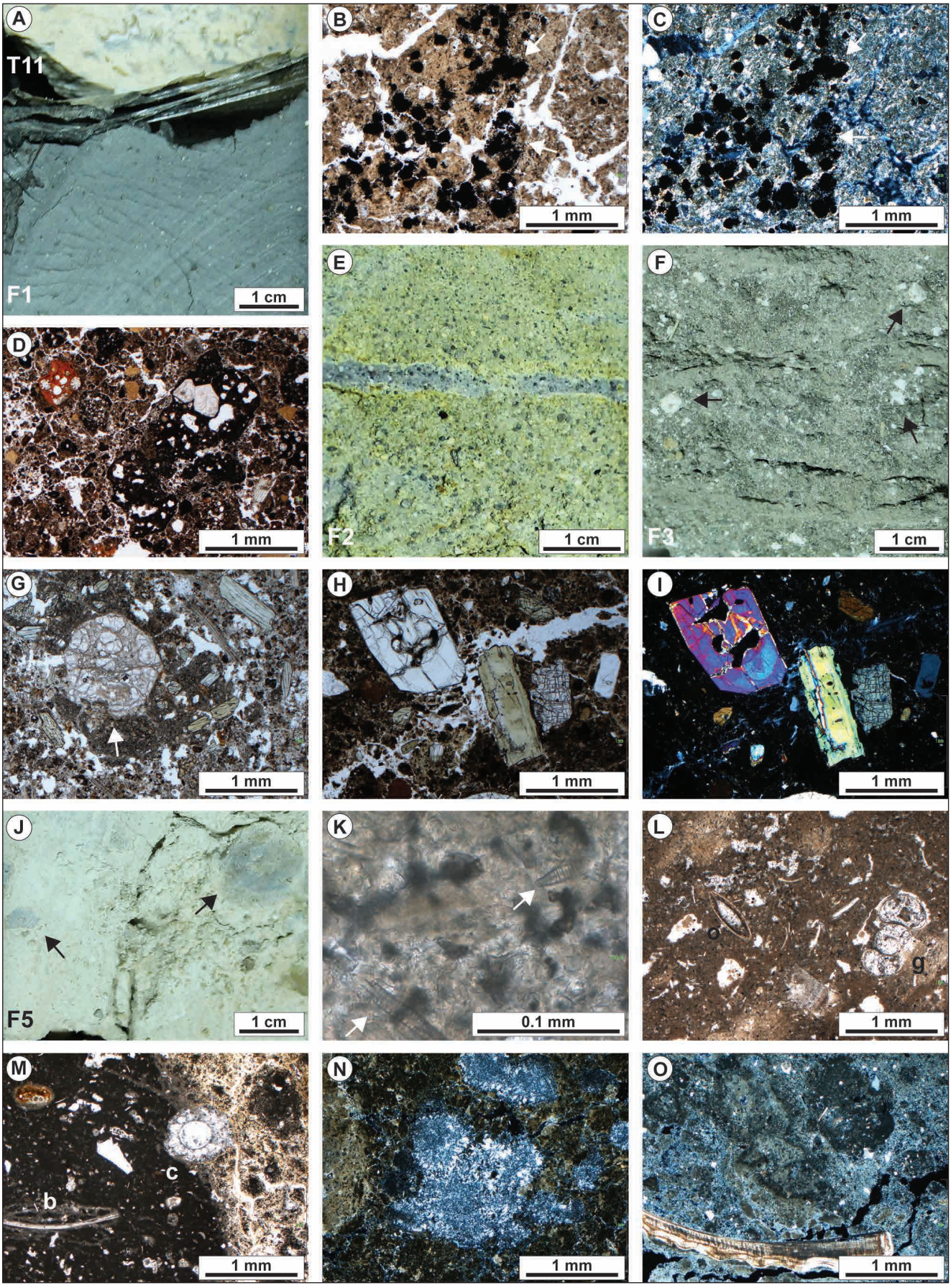
A
T11
F1
1 cm
B
1 mm
C
1 mm
D
1 mm
E
F2
1 cm
F
F3
1 cm
G
1 mm
H
1 mm
I
1 mm
J
F5
1 cm
K
0.1 mm
L
g
1 mm
M
b
c
1 mm
N
1 mm
O
1 mm

because of the presence of feldspatoid minerals such as leucite. This eruptive phase has been labelled Villa Senni and dated around 351-357 kyr (De Rita et al. 1995; Karner et al. 2001).

Travertine diagenetic features and porosity

The diagenetic features identified in the travertine deposits (Fig. 10) can be interpreted as the product of interaction with groundwater from the semi-confined aquifer within the travertine, rainfall precipitation and superficial drainage from the surrounding alluvial plain (Fig. 3). As reported in hydrogeological studies of the AAB (Petitta et al. 2010; Carucci et al. 2012; La Vigna et al. 2013ab), the semi-confined travertine aquifer is the site of mixing of meteoric water from the surrounding carbonate ridges and local plain recharge and geothermal fluids rising through faults from the deep Mesozoic-Cenozoic marine carbonate confined aquifer.

The pendant, equant and prismatic scalenohedral cements partially filling the travertine porosity are interpreted as the result of vadose and phreatic meteoric cement precipitation, respectively (cf. Chafetz et al. 1985; Della Porta et al. 2017; Török et al. 2017). The luminescence of some of the growth phases of the scalenohedral cement (Figs 10J-K) is indicative of oxygen depleted, reducing conditions and consequent Mn enrichment of the calcite crystals, within the phreatic meteoric pore water as confirmed also by the local occurrence of pyrite. Recrystallization of the travertine precipitated micrite and turbid dendrite crystals in limpid blocky sparite might be the result of meteoric phreatic diagenesis, as observed also in cores from the Yellowstone travertines (Chafetz & Guidry 2003). Diagenetic processes such as neomorphic spar formation and micritization of sparry calcite have both been described in travertines during early meteoric diagenesis (Guo & Riding 1992, 1994; Török et al. 2017). Pedogenetic features, such as alveolar textures (Fig. 10O), can be attributed to soil formation during temporary stasis of the thermal water outflow or following the deposition of the Tivoli travertines, from nearly 30 kyr according to Faccenna et al. (2008), up to present-day.

Dissolution features from sub-millimetre-scale vugs to metre-scale caves must have developed in the vadose zone and at the boundary with the phreatic water table. The present-day depth of the water table (Fig. 4) provides insights into the thickness of travertine succession affected by vadose and phreatic meteoric diagenesis, even though the water table must have fluctuated through time affecting different portions of travertines. The gaps in the stratigraphy due to lack of core recovery (e.g., 12-14 m depth in S1; 8-12 m depth in S4) might correspond to karstic caves as confirmed by the observation of quarry walls showing metre-scale caves and collapse breccias (Figs 17F, H, 18A) and in published studies (cf. Chafetz & Guidry 2003). In S5-S6, the 6 m thick T13 interval at 4.5-10.5 m depth coincides with the depth of no core recovery in S4 and with the depth of the present-day water table. Hence, this T13 rudstone might correspond to collapse breccia in karstic caves due to meteoric dissolution rather than being a syn-depositional detrital T13 rudstone/floatstone indicative of temporary subaerial exposure. In cores, without information about the facies lateral extension, it is difficult distinguishing these two types of travertine intraclast rudstone. The ostracode wackestone (C1) represents sediment filling primary voids, dissolution vugs and caves within the meteoric phreatic zone and in some cases it is overlain by prismatic

Fig. 12 - Core slab photos and photomicrographs of terrigenous and volcanic facies F6 to F10. A) S6 core image of facies F6 green fine sand, silt and clay embedding charcoal deriving from vegetation remains. B) Photomicrograph of F6 silt and clay with vegetation remains (black arrows). C) Core S7 image showing facies F7 green sand with plant or root remains oriented vertically (black arrow) and carbonate clasts (white arrows). D) and E) Parallel and crossed polarizers images of facies F7 with detrital angular quartz and feldspar grains in a clay matrix and sparse vadose pisoids with nuclei made of clotted peloidal micrite carbonate clasts (white arrows). F) S6 core image showing facies F8 chaotic mud-supported debris in green clay matrix with centimetre-size angular carbonate clasts (black arrows). G) Photomicrograph in crossed polarizers of facies F8 showing micritic carbonate clast with pendant bladed calcite cement (white arrows), detrital pyroxenes (p) and feldspars (f) in a clay to silt matrix. H) Photomicrograph of facies F8 with carbonate clasts and tubular structures made of prismatic calcite crystals probably related to rhyzoliths. I) Facies F9 polymictic conglomerate from core S7 with rounded embricated clasts. J) and K) Parallel and crossed polarizers photomicrograph of F9 conglomerate with clasts of Jurassic shallow-water carbonates (c) and chert (s). L) S7 core image of facies F10 cross-laminated fluvial sandstone. M) F10 litharenite with carbonate clasts with planktonic foraminifer (c), chert with radiolaria (s), detrital quartz and feldspar. N) Crossed polarizers photomicrograph of F10 litharenite with carbonate clasts with pendant vadose calcite cement (c), chert (s), detrital quartz (q), pyroxene (p) and interparticle porosity (white arrows).

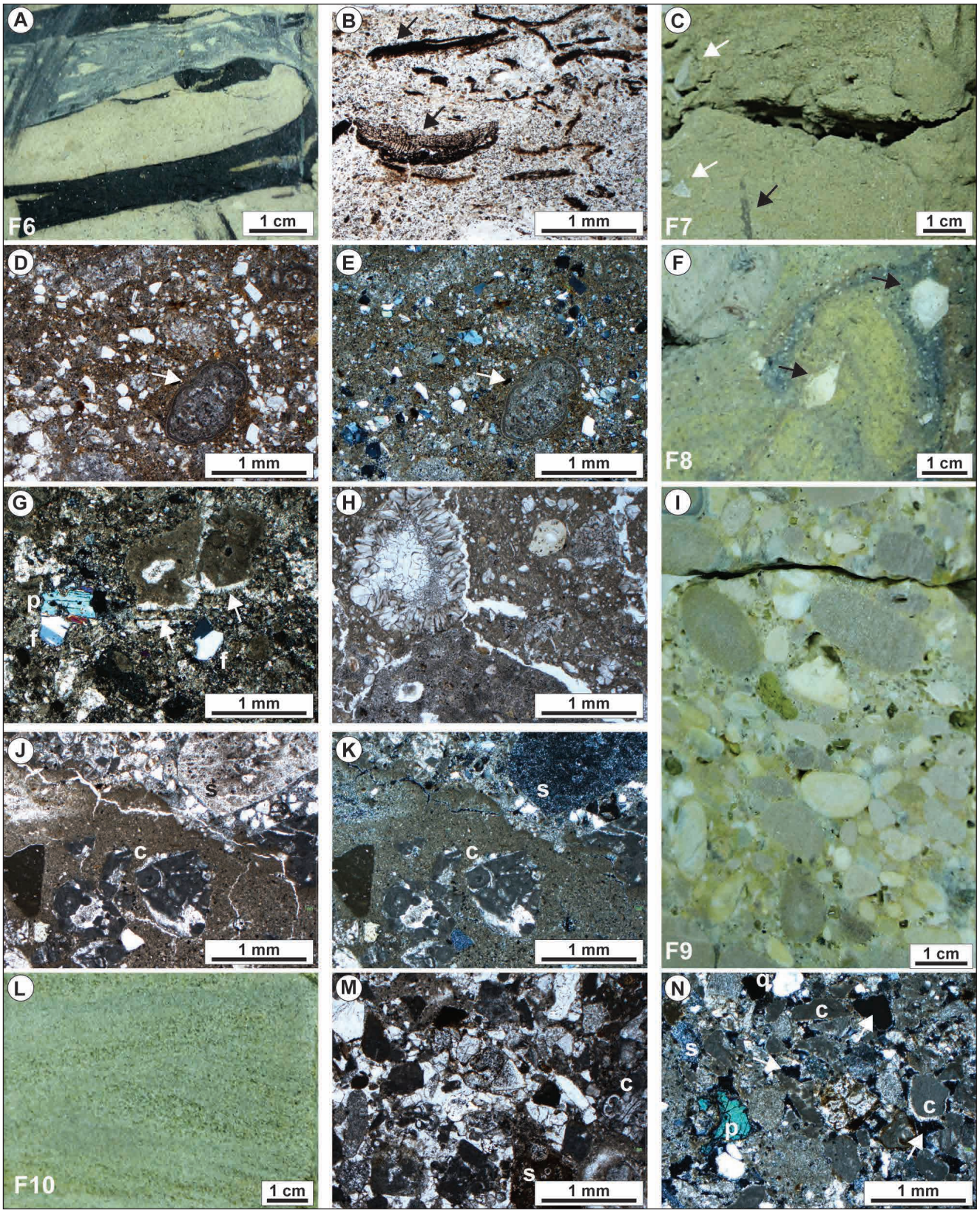

scalenohedral cement (Fig. 10F). The columnar cementstone structures associated with extraclastic and pisoidal packstone to rudstone (C2) occurring in core S7 (Figs 9E-J) are interpreted as karstic cave deposits with speleothems and adjacent pools with detrital sediment and vadose pisoids. The carbon stable isotope values of C2 deposits are enriched in ^{12}C with respect to the travertines (Fig. 15B), confirming the influence of meteoric karstic water for the precipitation of this cave-filling deposit.

The studied travertines show variable and high ranges of porosity and permeability with little direct correlation between the two parameters, as observed in other studies (Ronchi & Cruciani 2015; Della Porta et al. 2017), except for the detrital facies T13. The high porosity of the T4 coated bubbles is associated with low permeability due to lack of pore connection (cf. Della Porta et al. 2017; Erthal et al. 2017). Facies T2, T6, T8 and T10 display a wide spectrum of permeability values within the porosity range of 5-15 %. Travertines are characterized by complex growth framework and interlaminar pore networks and microporosity that result in strong isotropy in permeability, with horizontal permeability higher than the vertical one (Chafetz 2013; Soete et al. 2015; De Boever et al. 2016; Claes et al. 2017ab). In Pleistocene travertines from Central Italy, Ronchi & Cruciani (2015) determined that permeability values are not correlated with facies types, whereas porosity shows a stronger link with facies types, with raft and reed travertines achieving the highest porosity values. The highest reservoir properties in Pleistocene travertines from Turkey were determined for horizontal samples of dendritic shrubs (Claes et al. 2017b). In Pleistocene travertines from Hungary, Claes et al. (2017a) determined porosities of 5-15 % in terraced slope, smooth slope and marsh-pool facies, whereas the reed facies could reach up to 27 %.

Travertine stable isotope signature

The stable isotope values from this study are similar to those published for the Tivoli travertines by previous authors (Minissale et al. 2002; De Filippis et al. 2013b; Anzalone et al. 2017). The $\delta^{13}C$ and $\delta^{18}O$ signature of the Tivoli travertines falls within the published stable isotope ranges of hydrothermal travertines (cf. Pentecost 2005; Gandin & Capezzuoli 2008; Kele et al. 2008, 2011; Özkul et al. 2013; Capezzuoli et al. 2014; Claes et al. 2017a; Teboul et al. 2016) but with 2-4 ‰ heavier $\delta^{13}C$ values than other measured Neogene and Quaternary travertines in Central Italy (Fig. 15C; Minissale 2004; Gandin & Capezzuoli 2008; Della Porta 2015; Ronchi & Cruciani 2015; Croci et al. 2016; Della Porta et al. 2017). The negative $\delta^{18}O$ values might be influenced by the temperature of the precipitating thermal water and its original isotopic composition. The travertine $\delta^{13}C$ values must have been affected by thermal water pH, the isotopic composition of the dissolved inorganic carbon (DIC), which is influenced by the $\delta^{13}C$ of the dissolved substrate carbonate and CO_2 from different sources, the distance from the vent and the kinetic fractionation caused by downstream CO_2 degassing and rapid carbonate precipitation while thermal water is flowing (cf. Gonfiantini et al. 1968; Chafetz et al. 1991; Guo et al. 1996; Fouke et al. 2000; Minissale et al. 2002; Kele et al. 2008, 2011; Camuera et al. 2014; Della Porta 2015). The DIC of thermal water in Central Italy seems to derive from deep-seated geothermal sources influenced by the decarbonation of Mesozoic-Cenozoic marine limestones in the rock substrate, magmatic CO_2 sources from the mantle, meteoric water recharge and mixing between geothermal and groundwater (Minissale et al. 2002; Minissale 2004).

The measured $\delta^{13}C$ and $\delta^{18}O$ travertine values appear fairly uniform with a positive correlation between the carbon and oxygen isotope values as observed in other case studies (Chafetz & Guidry 2003; Kele et al. 2011; Della Porta et al. 2017). Even the detrital layers (facies T13), indicative of subaerial exposure, provide isotope values similar to the

Fig. 13 - SEM images of the travertine facies. A) The limpid equant microsparite to sparite (20-100 μm) cement lining the primary porosity in the T6 radial coated grain grainstone consists of euhedral rhombohedral calcite crystals (white arrows). B) The turbid lozenge shaped crystals of the T1 crystalline dendrites show nearly hexagonal cross-section and nanometre scale internal microporosity with moulds that can show squared, rounded or dumb-bell cross sections (white arrows). C) A broken crystal of T6 radial coated grains that shows euhedral well-developed crystal faces but it internally consists of nanometre-scale subrounded carbonate clots (black arrow). This supposed amorphous calcium carbonate (ACC) within the lozenge-shaped crystals is probably the cause of the turbid micritic appearance of such crystals. D) Facies T2 dendrites showing that clotted peloidal micrite consists of peloids (5-60 μm in diameter; white arrow) made of submicron-scale calcite spheres around which columnar bladed microsparite crystals (20-100 μm long; black arrows) are departing radially. The central peloid is made of nanometre-scale (0.1-1 μm) anhedral sub-spherical calcite structures, which might represent amorphous calcium carbonate (ACC). E) Enlarged image of peloid in panel D made of nanometre-scale (0.1-1 μm) anhedral sub-spherical calcite structures (white arrow). F) Peloids are also made of less than 1 μm size euhedral dodecahedral carbonate crystals (white arrow). G) Irregular, possibly organic, membrane in facies T6 attributable to microbial biofilm EPS embedding nanometre-scale subrounded structures, which might represent either amorphous calcium carbonate (ACC) or microbes with coccoid or dumbbell shape (white arrows). H) Organic membrane, probably EPS, embedding micron-size clots of calcite and micron-size coccoid bacterioform structures (white arrows).

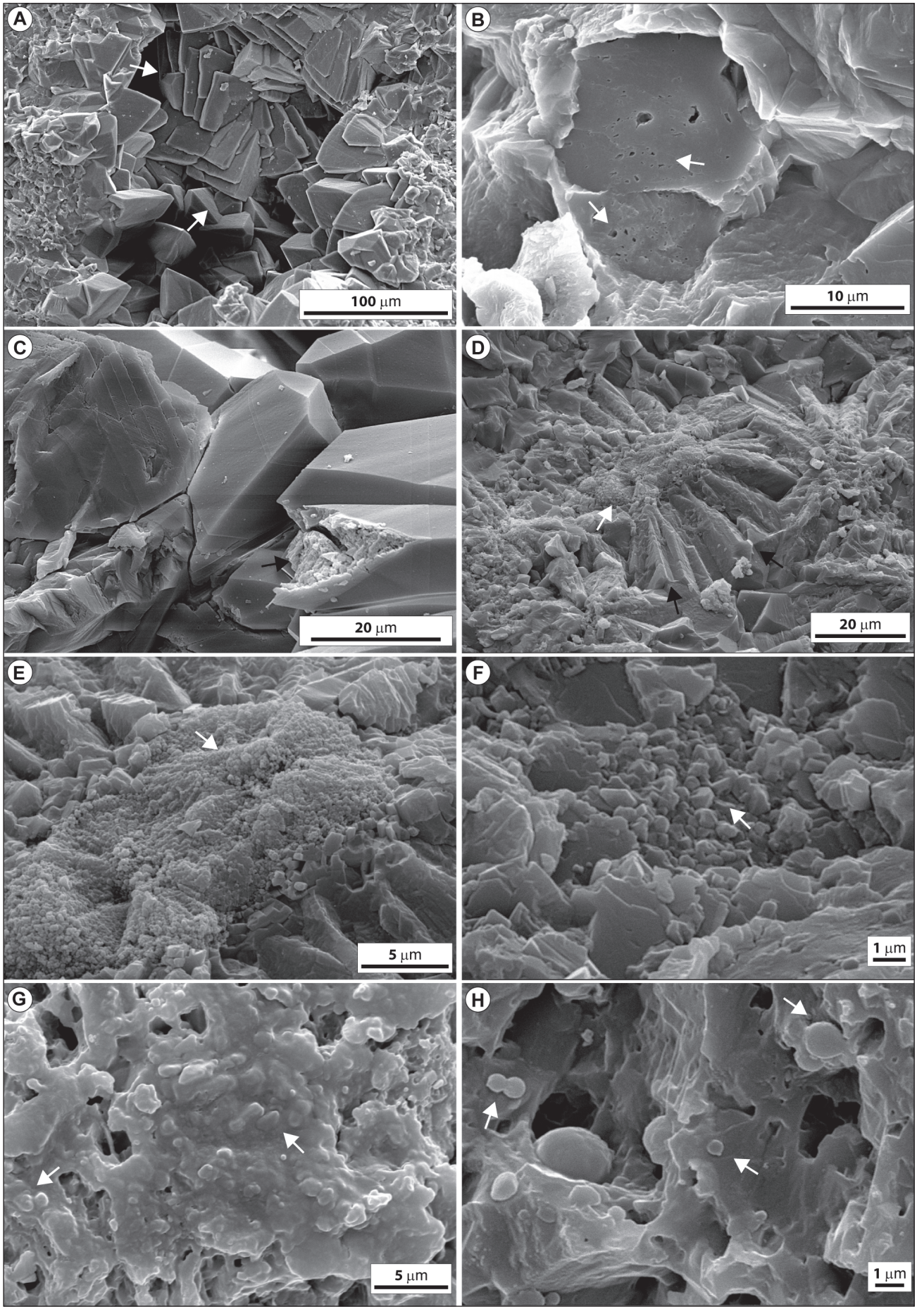
A
100 μm
B
10 μm
C
20 μm
D
20 μm
E
5 μm
F
1 μm
G
5 μm
H
1 μm

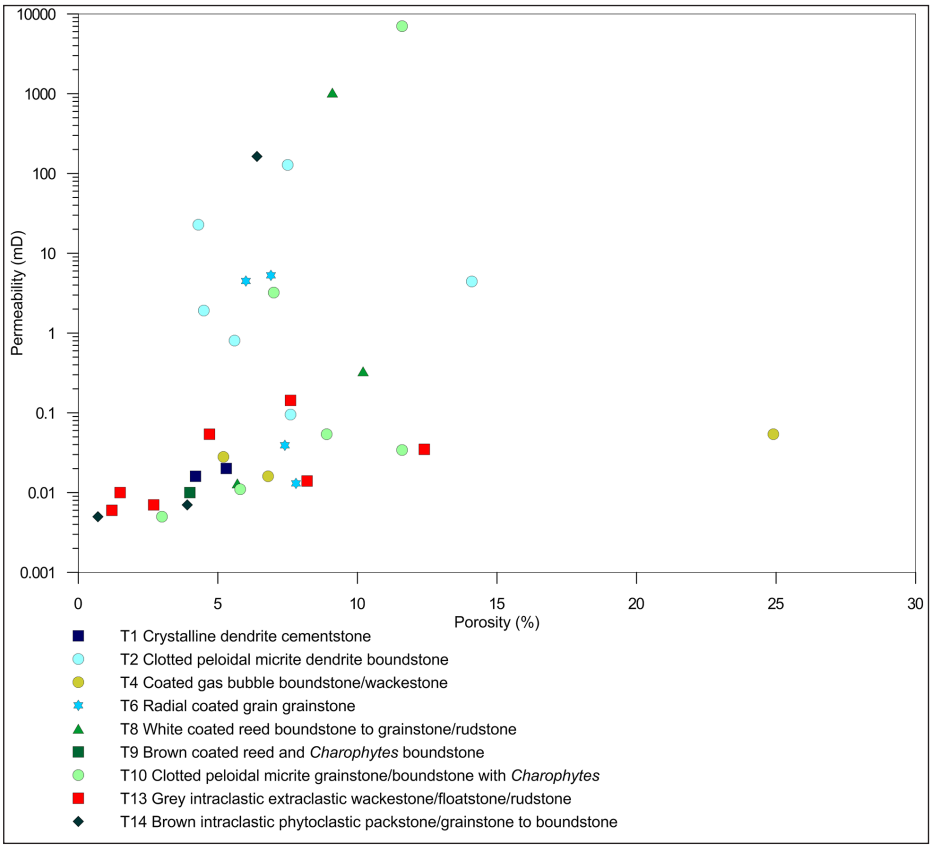

Fig. 14 - Plot of gas porosity and permeability measured on plugs for different travertine facies types from core S1.

precipitated travertines. The blocky and prismatic scalenohedral calcite cements attributed to meteoric phreatic diagenesis have $\delta^{13}C$ isotopic signature corresponding to the lower range of the travertine $\delta^{13}C$, with values between 8 and 10 ‰. Deviations from the range of $\delta^{13}C$ values characterizing the travertines with lighter carbon isotope values of 6-2 ‰ are shown by some samples belonging to the post-travertine carbonate filling (C1, C2) and facies T14. The C1 ostracode packstone/wackestone has only one value depleted in ^{13}C, with $\delta^{13}C$ around 4 ‰, which might be indicative of meteoric water influence. The C2 speleothem and vadose pisoid rudstone deposits from karstic cave in core S7 show $\delta^{13}C$ up to 6-9 ‰ lighter than the precipitated travertines suggesting the influence of soil derived ^{12}C from meteoric water. Two samples of facies T14 phytoclastic packstone to *Charophytes* boundstone derive from carbonate beds within the terrigenous substrate. These carbonates must have accumulated in freshwater lacustrine/palustrine settings before the onset of the main hydrothermal travertine deposition. One sample of facies T14, depleted in ^{13}C, underlies the C2 cave fill and must have been affected by the overlying meteoric diagenesis and ^{12}C enriched groundwater. All the other samples from facies with coated vegetation and *Charophytes* (T9, T10, T11, T14), detrital unconformity layers (T13), C1 ostracode packstone/wackestone and the meteoric phreatic cement do not show lighter $\delta^{13}C$ and heavier $\delta^{18}O$ values as it would be expected for cooler and meteoric freshwater. The most likely interpretation for this meteoric stable isotopic signature similar to the hydrothermal travertines must rely on the Tivoli hydrogeological system. As reported by Carucci et al. (2012) and La Vigna et al. (2013ab), the Pleistocene travertines represent a semi-confined shallow aquifer where deeply sourced geothermal water mixes with superficial precipitation and meteoric water inflowing from the adjacent mountain ridges. Because thermal water is recirculating in the travertine aquifer, the groundwater lens has a mixed stable isotope composition of meteoric and geothermal sources, with DIC likely largely derived from the thermal water. As a result, the post-travertine groundwater precipitates, including the meteoric phreatic cement, have isotopic signature similar to the hydrothermal travertines.

The expected $\delta^{13}C$ values of the precipitated carbonates in the Tivoli area were calculated using the equation proposed by Panichi & Tongiorgi (1976) $\delta^{13}C_{(CO2)} = 1.2 \times \delta^{13}C_{(trav)} - 10.5$, developed for

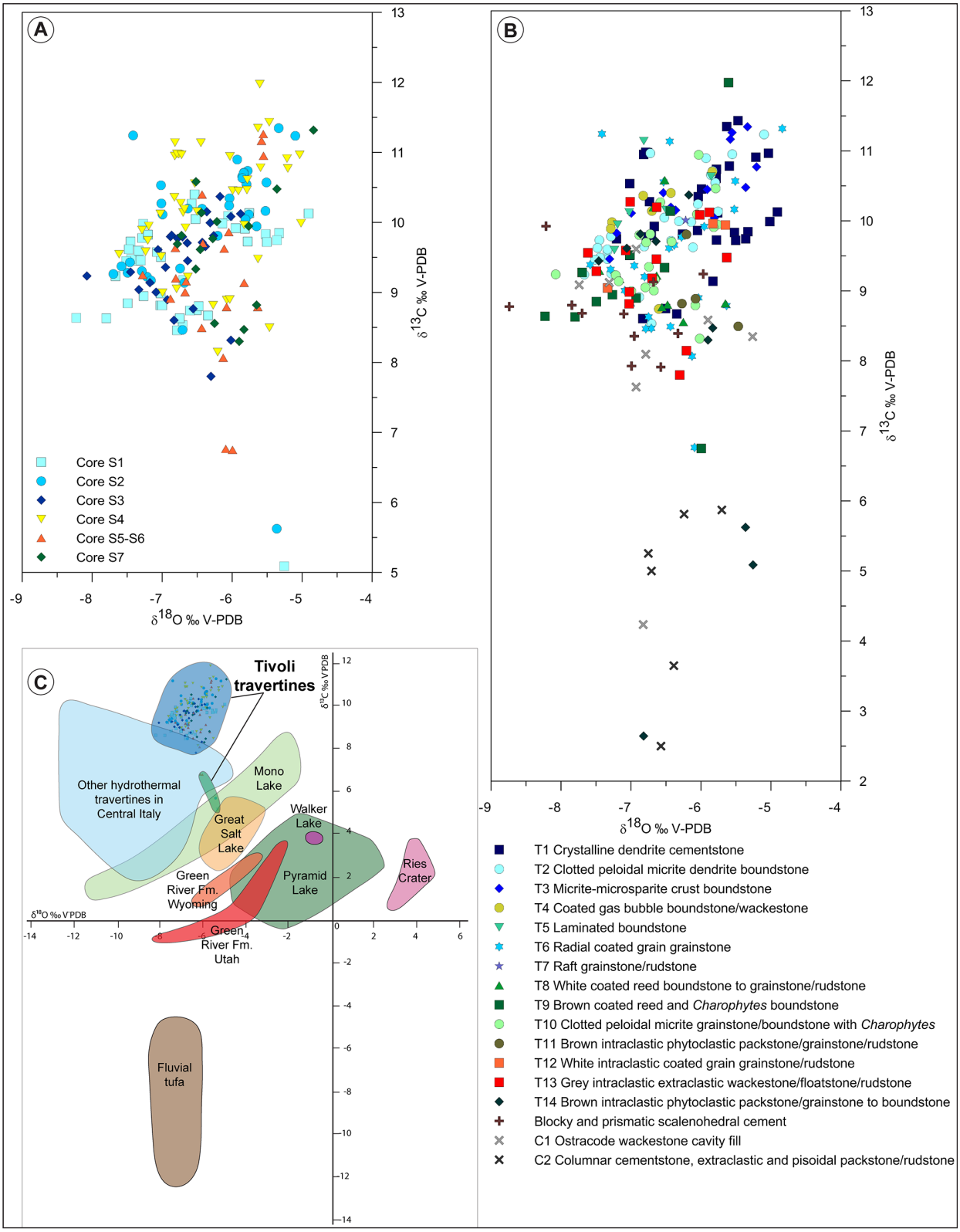

Fig. 15 - A) Stable carbon and oxygen isotope values of the studied travertines with respect to the sampled cores (S1 to S7). B) Stable carbon and oxygen isotope values plotted with respect to the travertine facies types (T1 to T13) compared with the isotopic signature of the carbonates associated with siliciclastics (T14) in the terrigenous substrate, the blocky and prismatic scalenohedral cement, and the post-travertine carbonate sediment filling (C1, C2). C) The stable isotope signature of the Tivoli travertines from this study plotted against those from various types of non-marine, spring and lacustrine carbonates (modified after Della Porta 2015). Most of the Tivoli hydrothermal travertines (large blue field) show heavier carbon isotope values when compared with other Neogene travertine deposits in Central Italy. Only a few samples (small green field) have lighter $\delta^{13}C$ signature but still in the range of other central Italian travertines. These samples correspond to facies T6, T8 and T14 likely influenced by ^{13}C depleted freshwater.

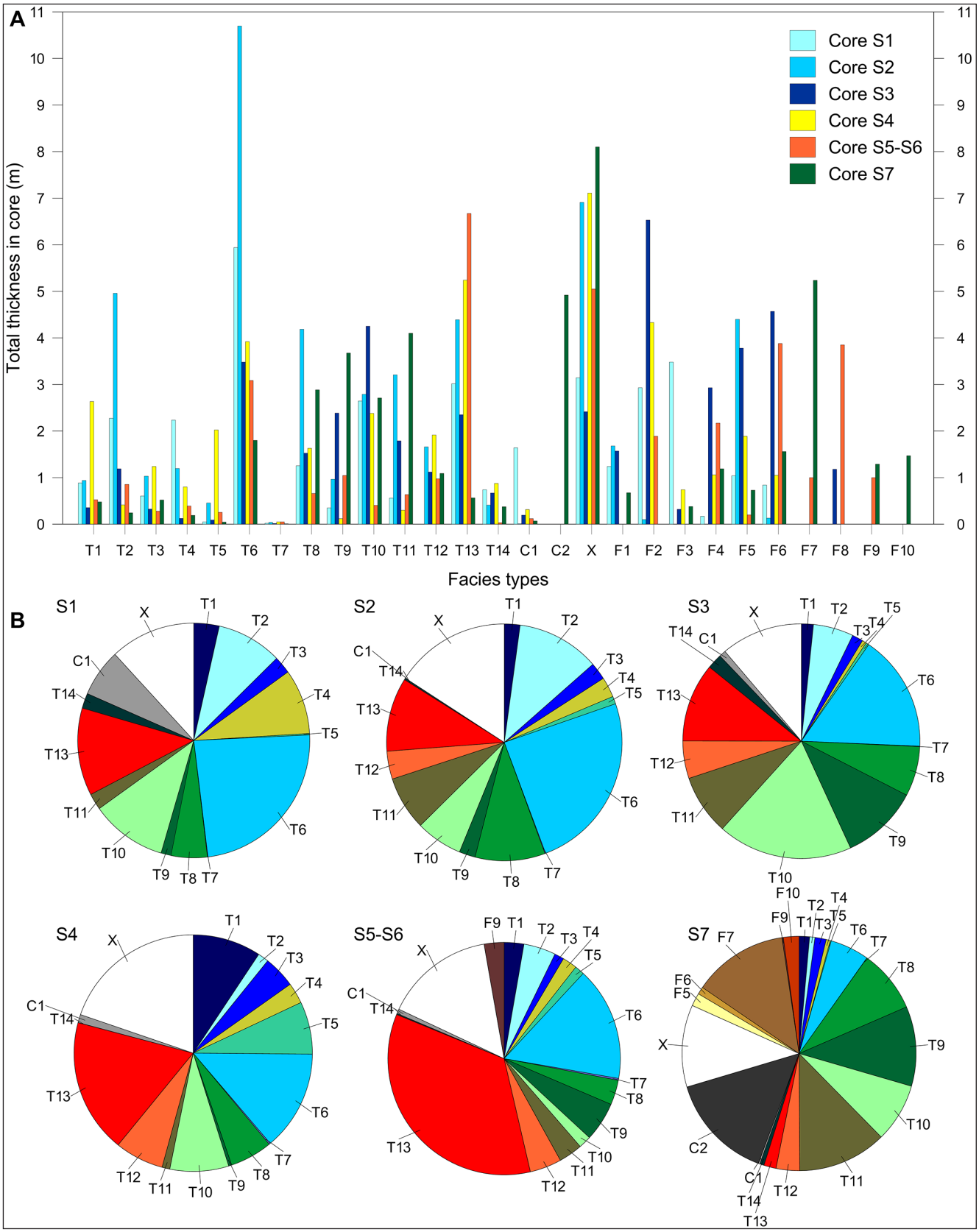

Fig. 16 - A) Histogram of the cumulative thickness of each facies type in the six analysed cores. Facies descriptions are reported in Table 1 and 2. X indicates the thickness of core not recovered during drilling. B) Pie chart diagrams showing the relative percentage of facies type thickness within the main travertine unit for each analysed core.

travertines in Central Italy and using the $\delta^{13}C_{(CO2)}$ of present-day thermal springs and groundwater in the Tivoli area measured by Carucci et al. (2012), assuming that they are similar to the Pleistocene ones. The calculated $\delta^{13}C$ values of the precipitated carbonates range between 9 and 16 ‰. The 9 ‰ value for carbonate precipitates is calculated using the $\delta^{13}C_{(CO2)}$ value of 0.69 ‰ measured from present-day groundwater in the quarry area (Carucci et al. 2012). This suggests that carbonates precipitated by groundwater in the travertine aquifer, such as the phreatic meteoric cement, can have heavy $\delta^{13}C$ values around 9 ‰ as the host travertines. This calculation additionally confirms that groundwater circulating within the travertine aquifer results from the mixing between superficial drainage, recharge from carbonate relieves and the deep geothermal water. Conversely, using the average travertine measured values of $\delta^{13}C_{(trav)}$ of 9-11 ‰, the calculated $\delta^{13}C_{(CO2)}$ results 2.7-0.3 ‰. According to Minissale et al. (2002), $\delta^{13}C$ of -1.0 to +2.0 ‰ is typical of CO_2 derived from the metamorphism of substrate Mesozoic marine limestones.

With respect to the oxygen isotope values, Tivoli present-day thermal water has low-temperatures (23°C; Pentecost & Tortora 1989). Calculations of the paleotemperature of the late Pleistocene thermal water, using the measured $\delta^{18}O$ values for core S1 and S3, the equation proposed by Kele et al. (2015) based on recent vent and pool travertine samples, and the water $\delta^{18}O$ value of -7.2 ‰ as published by Carucci et al. (2012), provide thermal water paleotemperature values ranging between 16 and 34°C, with average 21-23°C. This suggests that probably the Pleistocene thermal water had a temperature similar or only slightly higher than the present-day active thermal springs in the AAB (Fig. 2).

Stratigraphic architecture and evolution of the travertine depositional system through time

The Tivoli travertine deposits are characterized by numerous beds (facies T13) indicative of interruption of sedimentation and erosion related to intermittent vent activity. Each analysed core shows 4 to 6 main T13 unconformities, with thickness from a few decimetres to more than 1 m that were marked as U1 to U9 (Fig. 20). All the main unconformities logged in the cores, except U1, can tentatively be identified on the exposed quarry walls and laterally traced on satellite imagery (Figs 17, 18, 21). Information on these key stratigraphic surfaces extracted from the cores and interpretation of quarry wall imagery was imported in Petrel to develop a model of the stratigraphic architecture of the travertine system (Fig. 22). The travertine packages bounded by the unconformities have been labelled as units and named from older to younger as Unit 1 to 9 (Fig. 20). The proposed correlation of the unconformity surfaces across the cores is interpretative because of lack of age dating constraints and incomplete outcrop exposure of the core stratigraphy. The presence of numerous discontinuity surfaces of various magnitude had already been described in previous studies on the Tivoli travertines (Faccenna et al. 2008; De Filippis et al. 2013ab; Anzalone et al. 2017; Erthal et al. 2017). The unconformity surfaces U5 and U6 from this study, traced near core S5-S6 (Figs 18C, 21B), appear to be equivalent to the surfaces labelled as S3 and S1, respectively, by Faccenna et al. (2008) and De Filippis et al. (2013b, their Figure 7). However, the erosional surfaces S2, S3 and S4 by Erthal et al. (2017) might correspond to unconformities U4, U3 and U2, respectively, in the area around core S3 (Figs 17E, F, 21A). A direct correlation between this study and published literature was difficult due to limited information about the location of the few published images of quarry walls.

The terrigenous and volcanic substrate strata were tentatively correlated based on similar lithofacies (Figs 19 in Appendix 1, 20). Travertine deposition, dated by Faccenna et al. (2008) at 115-30 kyr, follows the upper pyroclastic deposits attributed to the Villa Senni volcanic event dated as 351-357 kyr (Karner et al. 2001) and seems to occur during the period of relative dormancy that characterized the Roman volcanic district between 250 and 45 kyr (Karner et al. 2001). In cores S1, S2, S3 and S7, between the upper pyroclastic deposits and the first travertine deposition, there are 1-2 m thick dark mudstone rich in organic matter (facies F1) representing stagnant shallow lake and marshes developed before the onset of travertine deposition.

Combining information on the stratigraphic unit architecture, internal stratal geometries and facies composition (Figs 19 in Appendix 1, 20-22), an evolution of the depositional system through space and time is proposed (Fig. 23). The Tivoli

travertine deposition is characterized by a general southward progradation consistent with the southern flow direction of thermal water, controlled by the substrate topographic gradient, dipping south towards the Aniene River incision. However, travertine units with beds dipping eastward and westward have also been identified (Figs 17, 18, 21). Even though there are several active and fossil springs in the AAB (Fig. 2), it is not known during which time the different hydrothermal vents were active. The stratal geometries seem to suggest that multiple active vents were present, which might have been located in the N-NE of the travertine deposits but also on the eastern and western sides of the analysed transect. In terms of facies association and depositional environments, the nine stratigraphic units comprise three lateral depositional zones indicative of travertine precipitation in proximal, intermediate and distal deposition (Figs 19 in Appendix 1, 20, 23), with respect to the inferred presence of fossil hydrothermal vents in the N-NE, for the older units, and in the E and W for the younger units, possibly along faults (Fig. 2A). The proximal zone (cores S1-S3) is dominated by facies association precipitated in horizontal to gently dipping micro-terraced, metres to decametres wide pools of terraced slopes (T2, T3, T4, T5, T6, T8, T10); the intermediate zone (cores S4, S5-S6) is characterized by steeply dipping (5-40°) terraced and smooth slopes dominated by facies T1, T5, T6; the distal zone (core S7) is represented by carbonate coated vegetation and algae (T8, T9, T10, T11, T14) accumulated in ponds and marsh environments with cooled thermal water and/or mixed with freshwater (marsh-pool facies in Guo & Riding 1998).

The older travertine units 1 and 2 are interpreted to pinch out towards the south in the intermediate zone where core S4 and S5-S6 are located (Figs 20-23). Travertine deposition, fed by the northern vents, seems not to have reached the southern location of core S7. In the proximal zone (S1-S3), unit 1 consists of travertines accumulated in laterally extensive, several metres wide sub-horizontal pools, locally micro-terraced (with dominant facies T6 and T2), lateral to a terraced slope system in the intermediate zone, with decimetre-size pool rims in core S4 (Fig. 19 in Appendix 1), dominated by T1, associated with T5 and T6 facies. Similarly to unit 1, unit 2 consists of proximal shallow ponds made of T2-T4 and T6 facies (S1, S2) lateral to a low-angle terraced slope with tens of metres wide pools with decimetre-size, rounded rims made of T1 crystalline dendrites (S3) evolving southward into a smooth slope (S4). This smooth slope consists of centimetre-thick layers made of facies T1, T5 and T6, dipping 5-30° towards the S and E. The unit 2 slope in S4 appears to pinch out in the intermediate zone and it is laterally adjacent, in core S5-S6, to distal ponds with encrusted reeds and *Charophytes* (T8-T11 and T14). The top of unit 2, below the U2 unconformity in the proximal cores S1-S3, is characterized by the deposition of the distal marsh facies association (T8-T11), suggesting that these freshwater ponds dominated by vegetation developed also in the proximal zone during phases of low discharge of thermal water preceding the development of the unconformity. Unit 3 appears to be limited to the proximal zone and characterized by deposition in low-angle terraced slope with tens of metres wide pools (S1) and freshwater ponds with vegetation and *Charophytes* (facies T8-T11) in cores

Fig. 17 - A) S1 quarry wall showing horizontal to gently inclined bedding with metre-thick facies T13 (grey intraclastic extraclastic wackestone/floatstone/rudstone) layers associated with siliciclastics marked with red dashed lines and colour fill. The lower metre-thick T13 interval corresponds to the U3 unconformity surface in core S1 (cf. Fig. 20). On the right side low-angle onlap terminations of the travertine beds against the T13 layer (blue arrow). B) S1 quarry wall showing horizontal to gently inclined bedding marked by the blue dashed line with decimetre- to centrimetre-thick facies T13 layers marked by the red dashed lines and colour fill. The two decimetre-thick layers of T13 correspond to the U4 and U3 unconformity surfaces in S1 (cf. Fig. 20). Some of the travertine layers show decimetre-size rounded rims of pools (blue arrow) suggesting a low-angle terraced slope system. C) S1 quarry wall showing horizontal to gently inclined bedding with numerous centimetre-thick facies T13 (red lines) and a decimetre-size rounded rim of pool (blue arrow) suggesting a low-angle terraced slope system. D) S2 quarry wall showing horizontal to gently inclined bedding with numerous centimetre-thick facies T13 (red lines) associated with clays. E) S3 quarry wall showing horizontal bedding. The four identified T13 layers (red dashed lines) might correspond from the top to the unconformity surfaces U5 to U2 in core S3 (cf. Fig. 20). F) S3 quarry wall showing horizontal bedding. At the top an area with karstic breccias related to meteoric dissolution and collapse (yellow dashed line). G) S3 quarry wall showing horizontal bedding. The dark yellow to brown intervals consist of facies rich in encrusted reeds and *Charophytes* algae (T8-T11) as logged in S3 core between 10 m and 16 m depth. H) S4 quarry wall showing south-dipping smooth slope clinoforms and T13 detrital layers (red lines and colour fill) associated with siliciclastics. The metre-thick T13 interval has been named as unconformity surface U4 in S4 (cf. Fig. 20). Quarry photos provided by Statoil ASA. Red dashed lines: T13 layers associated with siliciclastics. Blue dashed lines: travertine bedding. Yellow dashed lines: areas with travertine breccias due to collapse in karstic caves.

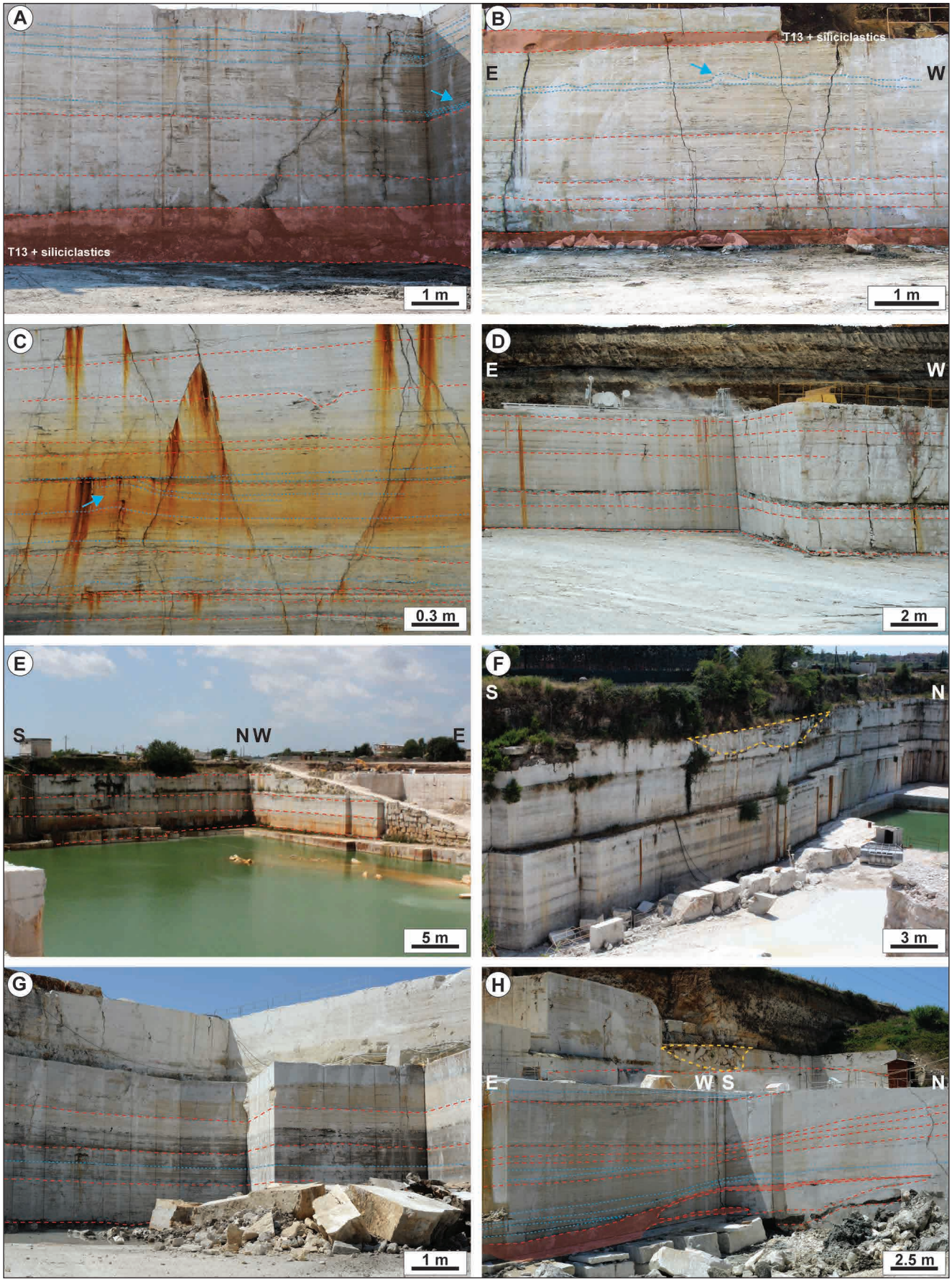
A
T13 + siliciclastics
1 m
B
T13 + siliciclastics
E
W
1 m
C
0.3 m
D
E
W
2 m
E
S
NW
E
5 m
F
S
N
3 m
G
1 m
H
E
W S
N
2.5 m

S2 and S3. Units 4 and 5 occur across the whole transect (Figs 19 in Appendix 1, 20-23), reaching the location of core S7 in the south. These units are characterized by a low-angle terraced system in the proximal zone (S1-S3), lateral to a smooth to terraced slope system in S5-S6, adjacent to distal travertine marshes (T8-T11), alternating with lacustrine and fluvial siliciclastic deposits (facies F5-F9) in the distal zone (S7). In the proximal S1-S2, the dominant facies association (T2-T4, T6) of unit 4 and 5 and the sparse centimetre-size microterraces and decimetre size pool rims formed by the T1 crystalline dendrites confirm deposition in a low-angle terraced system, within laterally extensive sub-horizontal pools frequently affected by interruption of the thermal water flow and subaerial exposure (Figs 17A-C). In S3, unit 4 shows horizontal ponds dominated by T10 and T8 facies, overlain by sub-horizontal, several metres wide travertine pools in unit 5. In S5-S6 unit 4 strata represent a smooth slope system with beds dipping 5-10° to locally 40° southward and eastward, whereas unit 5 was obliterated by the thick T13 interval that might correspond to collapse breccia in karstic caves. In S7, units 4 and 5 accumulated in distal shallow marsh environments. Unit 6 was deposited only in the intermediate and southern distal zone and terminates in onlap against the unconformity U5, a few tens of metres N, W and E of S4 (Figs 20, 21B, C), where it consists of sub-horizontal shallow ponds with common T10 and T6 facies. In core S5-S6, unit 6 travertines represent a low-angle terraced slope with sub-horizontal pools and decimetre size rims dipping southward and eastward, pinching out towards the west (Figs 18B, D). In S7, unit 6 includes distal travertine marshes (T8-T11) with siliciclastic fluvial and lacustrine deposits (Fig. 23). Unit 6 might have been sourced by vents located in the intermediate zone at lower elevation with respect to the vents sourcing units 1-5 or, alternatively, there was no change in the location of the active vent but rather a diversion in the water flow path. The younger units 7-9 are lens-shaped and appear to occur only in the southern area pinching out towards the north, east and west (Figs 21D, 22-23) and likely interfingering with siliciclastics southwards, as the underlying units. In core S7, these units consist of decimetre-size terraced slope and gently inclined smooth slope alternating with distal T8-T10 shallow pond facies.

Discussion

Travertine depositional geometry

The geometry of travertine deposits varies from high-relief fissure ridges, pinnacles, mounds and slope aprons to low-angle, gently sloping fans and lobes or tabular plateaus (cf. Pentecost 1995, 2005; Capezzuoli et al. 2014; Della Porta 2015 and references therein). Various studies have discussed the possible intrinsic and extrinsic parameters influencing the geometry of travertine depositional systems. These controlling factors range from the substrate morphology, topographic gradient, fault activity and subsidence rate to the rates of hydrothermal vent discharge and thermal water physicochemical properties affecting the rates and location of carbonate precipitation (Guo & Riding 1998, 1999; Hancock et al. 1999; Sant'Anna et al. 2004; Pentecost 2005; Brogi & Capezzuoli 2009; Brogi et al. 2010; Hammer et al. 2010; Guido & Campbell 2011; De Filippis et al. 2013ab; Capezzuoli et al. 2014; Della Porta 2015; Cook & Chafetz 2017; Della Porta et al. 2017; Lopez et al. 2017; Török et al. 2017).

Fig. 18 - A) S4 quarry wall showing east-dipping smooth slope clinoforms (blue lines) terminating in onlap towards the west against the T13 detrital facies (red lines) that corresponds to U5 unconformity surface in S4 (cf. Fig. 20). An area with travertine breccias due to collapse in karstic caves is marked with a yellow dashed line. B) S5-S6 quarry wall showing a south-dipping slope affected by brecciation and dissolution (T13 detrital facies due to subaerial exposure; red line) overlain by horizontal to southward gently dipping travertine strata (blue lines) terminating in onlap against the T13 surface. C) View of S5-S6 quarry wall showing sub-horizontal travertine bedding (blue lines) terminating in onlap against an east-dipping T13 interval (red line). The overlying package of travertine decreases in thickness and pinches out towards the west. The three unconformity surfaces marked with red dashed lines correspond from the top to U6, U5 and U4 in S5-S6 (cf. Fig. 20). D) View of S5-S6 quarry wall looking South showing bedding dipping eastward and wedge-shaped travertine packages pinching out northwards above a T13 layer associated with clays. The three unconformity surfaces marked with red dashed lines correspond from the top to U7, U6 and U5 in S5-S6 (cf. Fig. 20). E) View of S7 quarry showing metre-thick wedge shaped units pinching out towards the East and North. The dashed red lines correspond from the top to the T13 facies intervals addressed as unconformity surfaces U9 to U7 in core S7 (Fig. 20). Quarry photos provided by Statoil ASA. Red dashed lines: T13 layers associated with siliciclastics. Blue dashed lines: travertine bedding. Yellow dashed lines: areas with travertine breccias due to collapse in karstic caves.

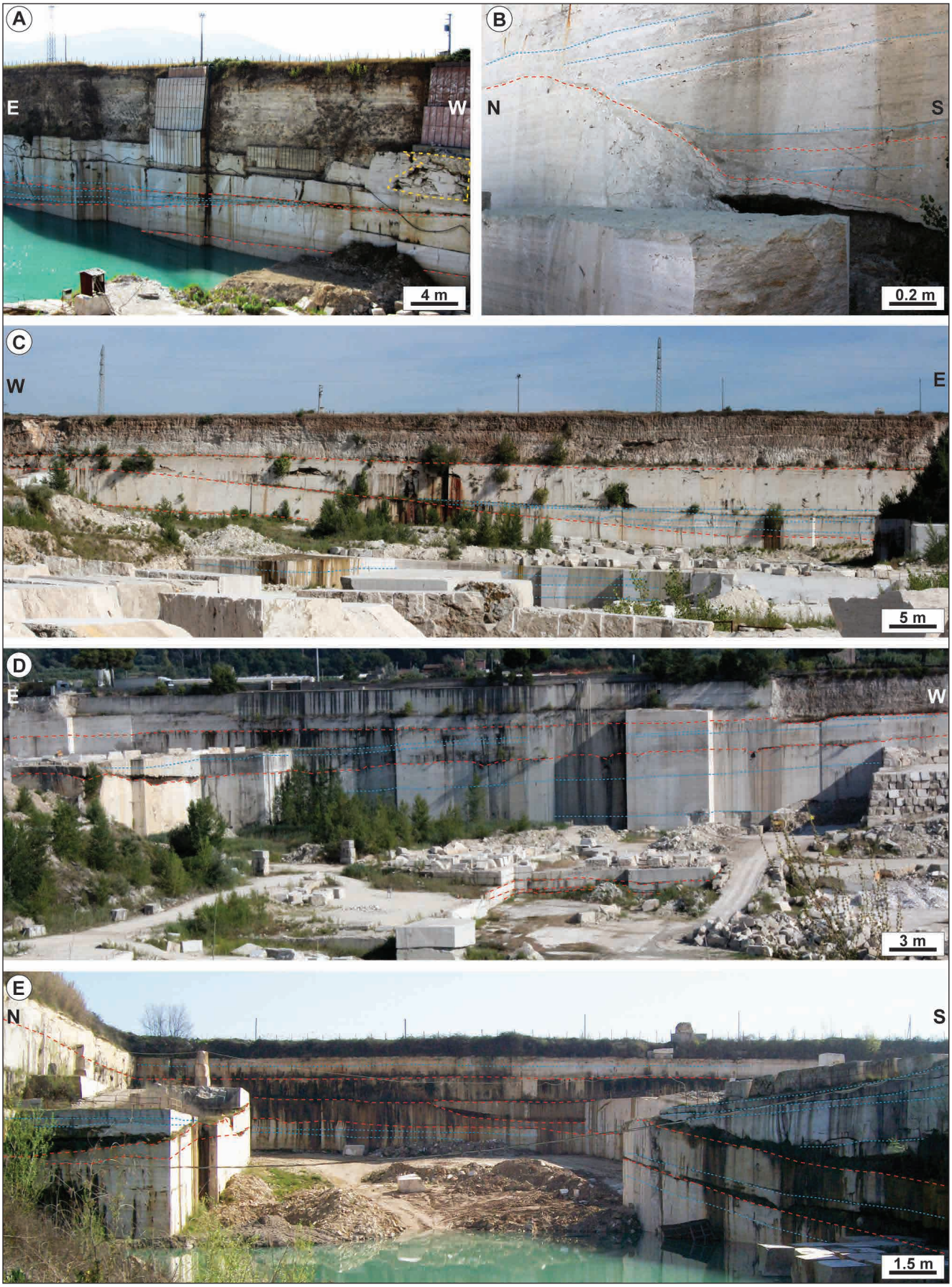
A
E
W
4 m
B
N
S
0.2 m
C
W
E
5 m
D
E
W
3 m
E
N
S
1.5 m

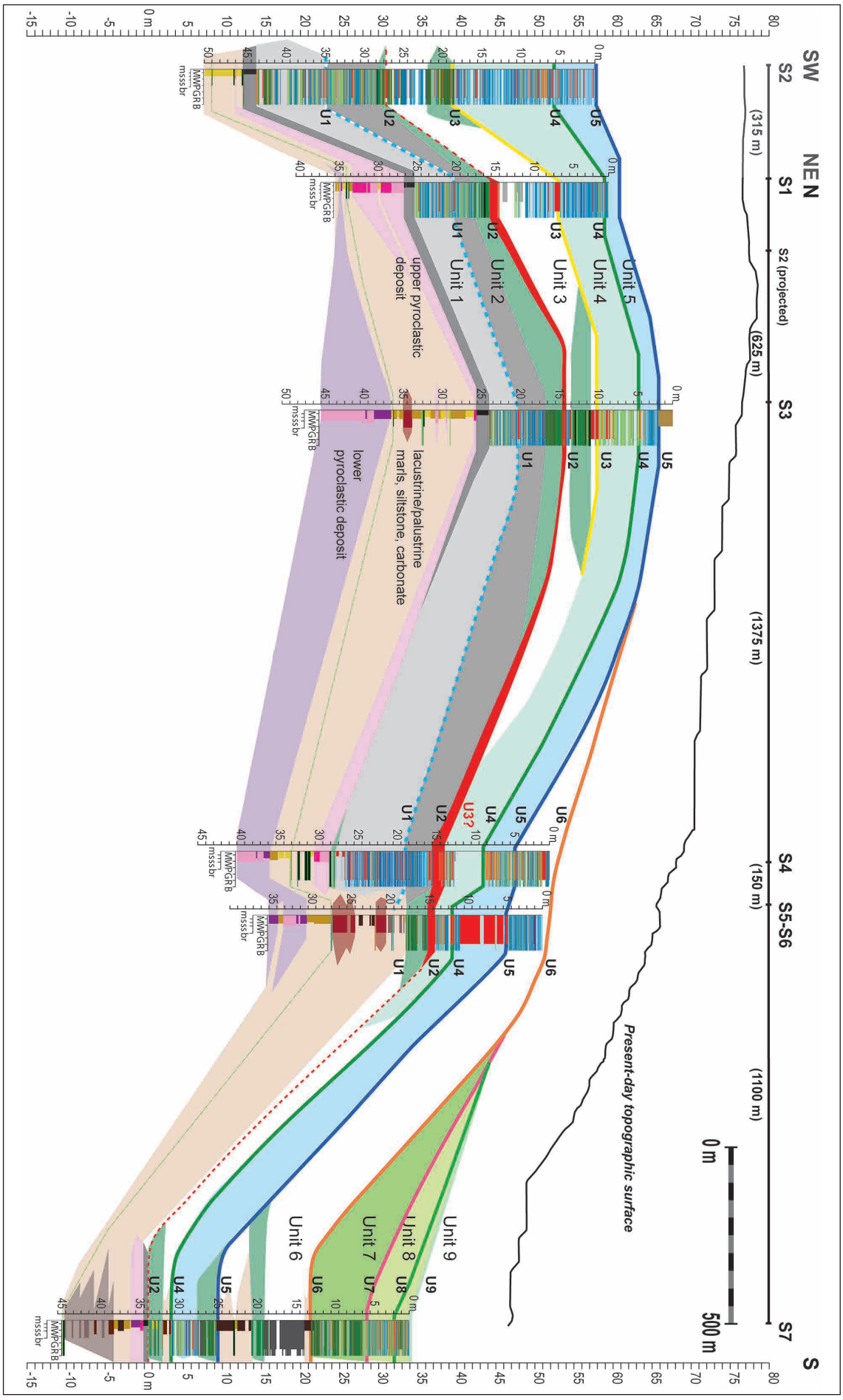

Fig. 20 - Correlation diagram with unconformity intervals labelled from base to top as U1 to U9 and the stratigraphic units labelled as Unit 1 to 9.

Fig. 21 - Google Earth Pro images showing the Tivoli travertine quarries with line drawing marking the key unconformity surfaces identified in the cores and used for correlation as shown in Figure 20. A) Oblique view towards the South of the northern part of the quarry area where cores S1 and S2 were drilled. Unconformity surfaces U4, U3 and U2 might correspond to erosional surfaces S2, S3 and S4, respectively, as labelled by Erthal et al. (2017). B) Oblique view towards the North of the intermediate part of the quarry area where core S5-S6 was drilled. To notice that U6 terminates in onlap against U5 towards the West and North. Unconformity surfaces U6 and U5 were labelled as S1 and S3, respectively, by Faccenna et al. (2008) and De Filippis et al. (2013ab). C) Oblique view towards the SE of the intermediate part of the quarry area where core S4 and S5-S6 were drilled. To notice that U6 terminates in onlap against U5 towards the West and North and U7 and U8 terminate against U6 towards the North. D) Oblique view towards the SE of the southern part of the quarry area where core S7 was drilled. To notice that U8 and U9 terminate in onlap against U7 towards the North. Coloured lines represent the unconformity surfaces traced: red U2; yellow U3; green U4; blue U5, orange U6; pink U7; light green U8; pale green U9.

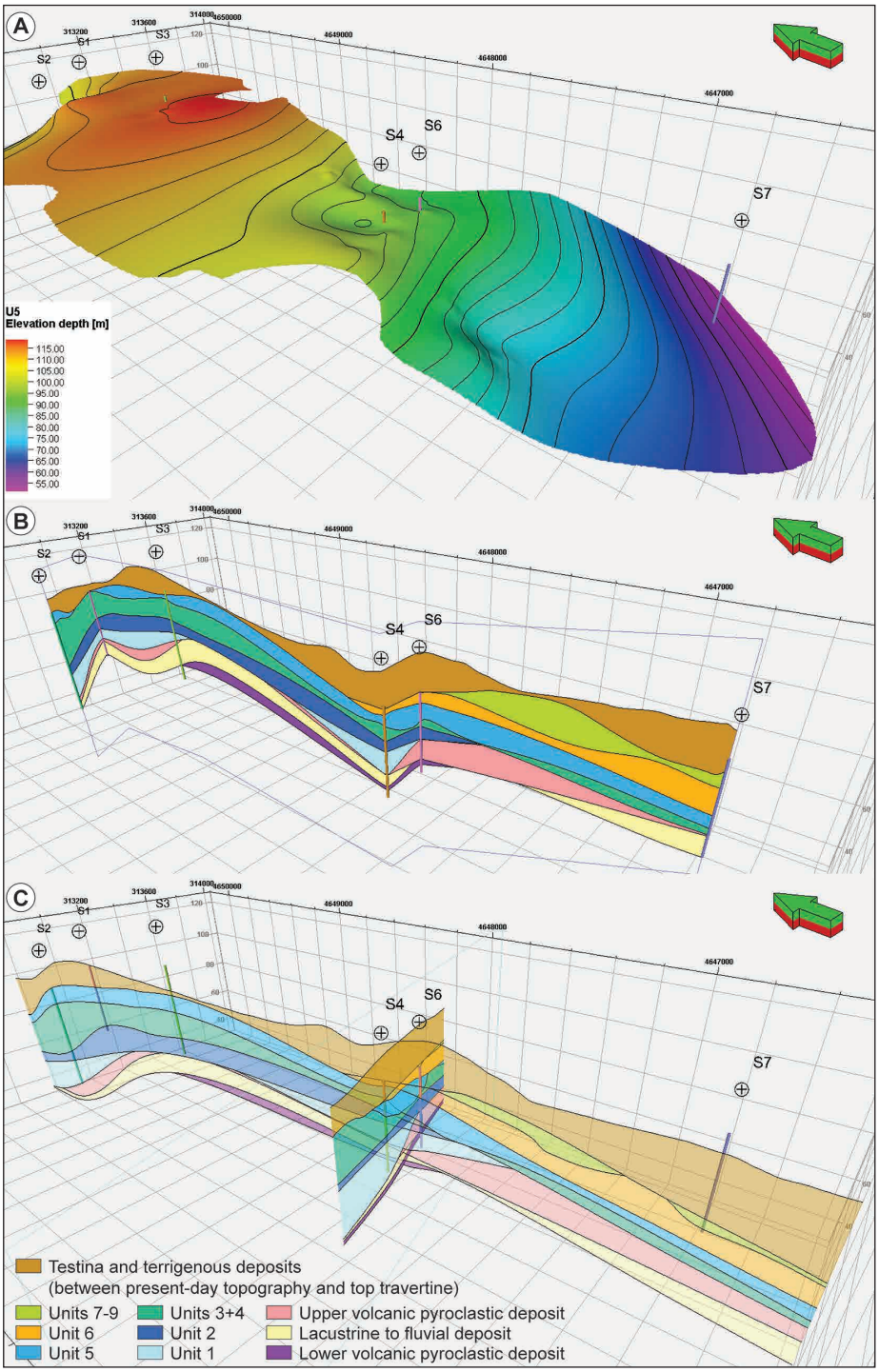

Fig. 22 - A) The U5 unconformity interpolated with a convergent algorithm using points picked on well stratigraphy and polylines digitized from orthorectified quarry wall images. B) Cross section tied to wells through the travertine model illustrating the geometry and stacking of the distinguished stratigraphic units. C) Fence diagram through the travertine model showing the lens-shaped geometry of unit 5 in the E-W cross section and unit 6 pinching out toward the N and W.

De Filippis et al. (2013b) described the Tivoli travertine geometry as a plateau, e.g., a large and massive thermal travertine deposit consisting of bedded travertine filling a tectonic depression and producing no prominent topography. The travertine plateau was composed of a sequence of sub-horizontal to gently southward dipping benches (Faccenna et al. 2008; De Filippis et al. 2013b). These authors explain the difference between a travertine plateau and a fissure ridge, as the one cropping out in the Denizli Basin (Turkey), as controlled by lateral progradation due to the growth in a subsiding basin with high discharge rate and high carbonate precipitation far away from the springs. A fissure ridge instead is characterized by a reduced discharge rate and travertine precipitation close to the springs, causing vertical aggradation (De Filippis et al. 2013b).

The geometry of the studied Tivoli travertines is characterized by proximal gently-dipping, ne-

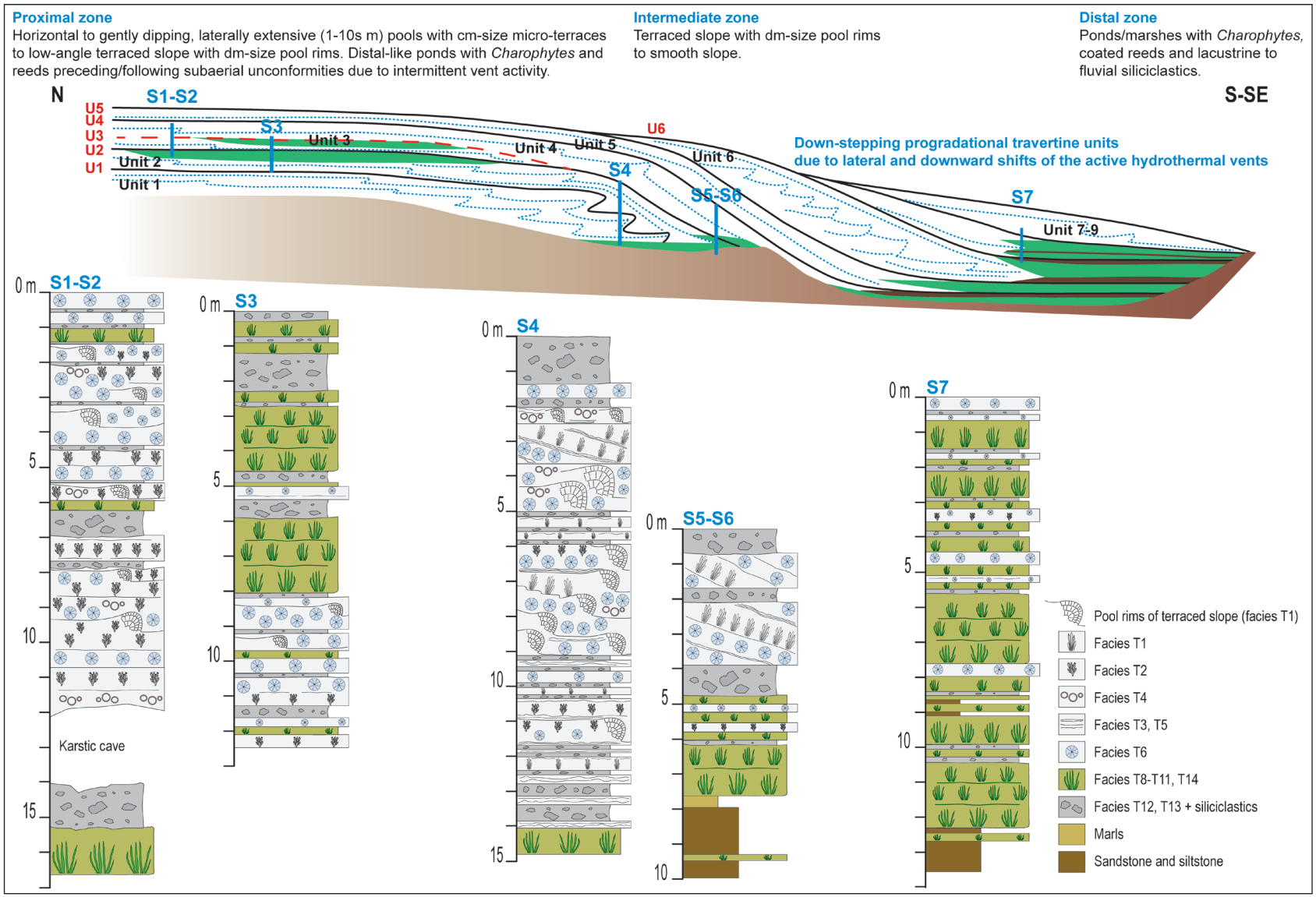

Fig. 23 – Interpretative depositional model of the studied N-S transect of the Tivoli travertines showing the subdivision in depositional zones with respect to inferred active vents in the North and the identified units bounded by unconformity surfaces (U). The proximal zone in the North (cores S1-S3) is characterized by low-angle terraced system with decametre-scale pools; the intermediate zone (cores S4, S5-S6) consists of terraced and smooth slope depositional environments, the distal zone (core S7) is dominated by marsh ponds with carbonate coated vegetation and algae (in green) alternating with siliciclastic deposits. The six stratigraphic logs show the facies superposition of selected portions of the drilled cores as marked by the blue lines in the depositional model.

Sample Category	$\delta^{13}C$ (V-PDB)	$\delta^{18}O$ (V-PDB)	Sample Category	$\delta^{13}C$ (V-PDB)	$\delta^{18}O$ (V-PDB)
S1 core average (n=40)	9.2	-6.8	**T5 facies average (n=6)**	10.3	-6.8
S1 SD	0.9	0.8	T5 SD	0.5	0.5
S2 core average (n=31)	9.9	-6.4	T5 max	11.1	-5.9
S2 SD	1.1	0.8	T5 min	9.6	-7.2
S3 core average (n=22)	9.4	-6.7			
S3 SD	0.5	0.5	**T6 facies average (n=24)**	9.4	-6.4
S4 core average (n=37)	10.1	-6.2	T6 SD	1.1	0.7
S4 SD	0.7	0.7	T6 max	11.3	-4.8
S5-S6 core average (n=18)	9.2	-6.2	T6 min	6.8	-7.6
S5-S6 SD	1.2	0.5			
S7 core average (n=15)	9.7	-6.1	**T7 facies (n=1)**	10.0	-6.2
S7 SD	0.8	0.5			
C1 fill average (n=8)	8.1	-6.7	**T8 facies average (n=9)**	9.3	-6.6
C1 SD	1.7	0.8	T8 SD	0.7	0.5
C1 max	9.6	-5.3	T8 max	10.6	-5.7
C1 min	4.2	-7.7	T8 min	8.6	-7.5
C2 cave fill average (n=6)	4.7	-6.4	**T9 facies average (n=11)**	9.2	-7.0
C2 SD	1.3	0.4	T9 SD	1.2	0.8
C2 max	5.9	-5.7	T9 max	12.0	-5.6
C2 min	2.5	-6.8	T9 min	6.7	-8.2
Cement average (n=11)	8.7	-7.2	**T10 facies average (n=21)**	9.5	-6.6
Cement SD	0.6	0.8	T10 SD	0.6	0.6
Cement max	9.9	-6.0	T10 max	10.9	-5.8
Cement min	7.9	-8.7	T10 min	8.3	-8.1
T1 facies average (n=33)	10.1	-6.1	**T11 facies average (n=4)**	9.0	-6.0
T1 SD	0.7	0.7	T11 SD	0.6	0.4
T1 max	11.4	-4.9	T11 max	9.8	-5.5
T1 min	8.6	-7.2	T11 min	8.5	-6.3
T2 facies average (n=27)	9.9	-6.6	**T12 facies average (n=3)**	9.6	-6.3
T2 SD	0.7	0.7	T12 SD	0.5	0.9
T2 max	11.2	-5.1	T12 max	10.0	-5.7
T2 min	8.5	-7.7	T12 min	9.0	-7.3
T3 facies average (n=13)	10.4	-6.1	**T13 facies average (n=14)**	9.4	-6.7
T3 SD	0.6	0.7	T13 SD	0.7	0.6
T3 max	11.3	-5.2	T13 max	10.3	-5.6
T3 min	9.5	-7.3	T13 min	7.8	-7.6
T4 facies average (n=7)	10.0	-6.7	**T14 facies average (n=10)**	7.9	-6.3
T4 SD	0.6	0.5	T14 SD	2.6	0.7
T4 max	10.7	-5.8	T14 max	10.4	-5.3
T4 min	8.7	-7.3	T14 min	2.6	-7.5

Tab. 3 - Stable C and O isotope values of the investigated travertines. SD = standard deviation.

arly tabular but terraced units at the decametre scale, passing into slope aprons pinching out distally, with a complex internal architecture, characterized by vertically and laterally stacked units separated by unconformities. The alternation of depositional and erosional phases must have been controlled by the intermittent activity of the hydrothermal vent and thermal water outflow or changes in the thermal water flow direction. Therefore, the final geometry of the travertine system results from the combination of the shape of the individual units and how they are superimposed at every renewal of thermal water flow. Two types of growth styles were identified in the Tivoli travertines (Fig. 23). 1) The older units 1 to 5 show aggradation in the proximal zone and progradation in the intermediate and distal zones. In the proximal zone, travertine strata aggrade vertically with uniform thickness and nearly tabular geometry, whereas laterally a slope apron develops in correspondence of an increase in dip of the underlying substrate. The slope apron progrades and pinches out following the underlying topography and, from unit 1 to 5, travertines reach locations gradually further to the south. 2) The younger units 6 to 9 are sloping lobes that develop in the intermediate to distal zone, terminating in onlap towards the N, E and W against the older underlying depositional unit (previous break in slope) and pinching out in the direction of the topographic gradient dips. Units 6-9 are laterally superimposed showing a southward step-down pattern. The described depositional architecture suggests that while units 1-5 might have been sourced by vents located to the N-NE of the proximal area, the deposition of units 6 to 9 likely relates to hydrothermal springs located more to the south, in the intermediate zone, at lower topographic elevations and laterally shifted to the east or to the west with respect to the

	Core S1	Total core thickness (m)	Total travertine thickness (m)	Terrigenous substrate thickness (m)			Core S2	Total core thickness (m)	Total travertine thickness (m)	Terrigenous substrate thickness (m)		
		35	24.83	10.17				40	43.33	6.67		
Facies types	**Number logged beds**	**Max thickness (m)**	**Min thickness (m)**	**Cumulative facies thickness (m)**	**% facies in whole core**	**% facies in travertine thickness**	**Number logged beds**	**Max thickness (m)**	**Min thickness (m)**	**Cumulative facies thickness (m)**	**% facies in whole core**	**% facies in travertine thickness**
T1	23	0.1	0.005	0.86	**2.5**	**3.6**	32	0.11	0.01	0.94	**1.9**	**2.2**
T2	75	0.16	0.005	2.28	**6.5**	**9.2**	289	0.08	0.003	4.96	**9.9**	**11.4**
T3	65	0.07	0.005	0.60	**1.7**	**2.4**	160	0.03	0.002	1.03	**2.1**	**2.4**
T4	69	0.19	0.005	2.23	**6.4**	**9.0**	53	0.13	0.005	1.20	**2.4**	**2.8**
T5	3	0.025	0.01	0.05	**0.1**	**0.2**	15	0.105	0.005	0.45	**0.9**	**1.1**
T6	196	0.17	0.005	5.94	**17.0**	**23.9**	411	0.2	0.005	10.70	**21.4**	**24.7**
T7	2	0.01	0.01	0.02	**0.1**	**0.1**	3	0.03	0.005	0.04	**0.1**	**0.1**
T8	31	0.135	0.01	1.25	**3.6**	**5.1**	109	0.24	0.005	4.18	**8.4**	**9.7**
T9	5	0.15	0.02	0.35	**1.0**	**1.4**	13	0.18	0.02	0.96	**1.9**	**2.2**
T10	69	0.22	0.005	2.64	**7.6**	**10.7**	80	0.21	0.005	2.79	**5.6**	**6.4**
T11	5	0.17	0.06	0.56	**1.6**	**2.3**	46	0.42	0.005	3.21	**6.4**	**7.4**
T12	0	0	0	0	**0**	**0**	47	0.2	0.005	1.66	**3.3**	**3.8**
T13	41	1.07	0.005	3.02	**8.6**	**12.1**	103	0.21	0.005	4.39	**8.8**	**10.1**
T14	5	0.52	0.04	0.74	**2.1**	**2.1**	4	0.15	0.06	0.41	**0.8**	**0.2**
C1	8	0.205	0.01	1.64	**4.7**	**6.6**	0.01	0.01	0.01	0.01	**0.02**	**0.02**
C2	0	0	0	0	**0**	**0**	0	0	0	0	**0**	**0**
X	24	0.92	0.01	3.15	**9.0**	**11.9**	45	0.88	0.01	6.91	**13.8**	**15.9**
F1	3	0.94	0.05	1.24	**3.5**		3	1.03	0.05	1.68	**3.4**	
F2	5	0.98	0.1	2.93	**8.4**		1	0.1	0.1	0.1	**0.2**	
F3	5	1.16	0.15	3.48	**9.9**		0	0	0	0	**0**	
F4	1	0.17	0.17	0.17	**0.5**		0	0	0	0	**0**	
F5	4	0.39	0.09	1.04	**3.0**		3	2.76	0.7	4.4	**8.8**	
F6	4	0.25	0.17	0.84	**2.4**		1	0.13	0.13	0.13	**0.3**	
F7	0	0	0	0	**0**		0	0	0	0	**0**	
F8	0	0	0	0	**0**		0	0	0	0	**0**	
F9	0	0	0	0	**0**		0	0	0	0	**0**	
F10	0	0	0	0	**0**		0	0	0	0	**0**	

Tab. 4 - Distinguished facies type thickness and relative percentage in each analysed core (X = thickness of non-recovered intervals).

	Core S3	Total core thickness (m)	Total travertine thickness (m)	Terrigenous substrate thickness (m)			Core S4	Total core thickness (m)	Total travertine thickness (m)	Terrigenous substrate thickness (m)		
	45	21.67	21.49					40	28.21	11.79		
Facies types	**Number logged beds**	**Max thickness (m)**	**Min thickness (m)**	**Cumulative facies thickness (m)**	**% facies in whole core**	**% facies in travertine thickness**	**Number logged beds**	**Max thickness (m)**	**Min thickness (m)**	**Cumulative facies thickness (m)**	**% facies in whole core**	**% facies in travertine thickness**
T1	23	0.03	0.005	0.36	**0.8**	**1.6**	104	0.1	0.005	2.63	**6.6**	**9.3**
T2	73	0.12	0.005	1.19	**2.6**	**5.5**	30	0.045	0.005	0.42	**1.0**	**1.5**
T3	48	0.03	0.005	0.32	**0.7**	**1.5**	86	0.115	0.005	1.24	**3.1**	**4.4**
T4	8	0.03	0.01	0.13	**0.3**	**0.6**	37	0.09	0.005	0.8	**2.0**	**2.8**
T5	6	0.03	0.01	0.09	**0.2**	**0.4**	53	0.2	0.005	2.03	**5.1**	**7.2**
T6	151	0.1	0.005	3.48	**7.7**	**16.1**	172	0.09	0.005	3.92	**9.8**	**13.7**
T7	2	0.01	0.005	0.015	**0.03**	**0.1**	5	0.01	0.01	0.05	**0.1**	**0.2**
T8	55	0.165	0.005	1.52	**3.4**	**6.9**	61	0.105	0.005	1.63	**4.1**	**5.8**
T9	28	0.26	0.015	2.38	**5.3**	**10.6**	1	0.12	0.12	0.12	**0.3**	**0.4**
T10	83	0.2	0.005	4.25	**9.4**	**18.4**	86	0.17	0.005	2.38	**5.9**	**8.0**
T11	26	0.3	0.01	1.79	**4.0**	**8.3**	3	0.12	0.09	0.3	**0.7**	**1.1**
T12	33	0.11	0.01	1.12	**2.5**	**5.2**	60	0.1	0.005	1.92	**4.8**	**6.6**
T13	42	0.47	0.005	2.35	**5.2**	**10.8**	93	0.77	0.005	5.24	**13.1**	**18.3**
T14	7	0.17	0.03	0.67	**1.5**	**2.1**	4	0.34	0.005	0.87	**2.2**	**0.02**
C1	4	0.08	0.01	0.20	**0.4**	**0.9**	4	0.235	0.01	0.32	**0.8**	**1.1**
C2	0	0	0	0	**0**	**0**	0	0	0	0	**0**	**0**
X	20	0.47	0.01	2.41	**5.4**	**11.1**	23	3.77	0.02	7.11	**17.8**	**19.7**
F1	2	1.52	0.05	1.57	**3.5**		0	0	0	0	**0**	
F2	10	2	0.14	6.53	**14.5**		3	2.4	0.74	4.33	**10.8**	
F3	1	0.32	0.32	0.32	**0.7**		1	0.74	0.74	0.74	**1.9**	
F4	5	0.95	0.23	2.93	**6.5**		2	0.86	0.2	1.06	**2.7**	
F5	9	0.74	0.15	3.78	**8.4**		6	0.75	0.08	1.89	**4.7**	
F6	9	1.17	0.1	4.57	**10.2**		1	1.05	1.05	1.05	**2.6**	
F7	0	0	0	0	**0**		0	0	0	0	**0**	
F8	1	1.18	1.18	1.18	**2.6**		0	0	0	0	**0**	
F9	0	0	0	0	**0**		0	0	0	0	**0**	
F10	0	0	0	0	**0**		0	0	0	0	**0**	

Tab. 4 - Distinguished facies type thickness and relative percentage in each analysed core (X = thickness of non-recovered intervals).

	Core S5-S6	Total core thickness (m)	Total travertine thickness (m)	Terrigenous substrate thickness (m)			Core S7	Total core thickness (m)	Total travertine thickness (m)	Terrigenous substrate thickness (m)		
		35	**19.36**	**15.64**				**44.31**	**33.38**	**10.82**		
Facies types	**Number logged beds**	**Max thickness (m)**	**Min thickness (m)**	**Cumulative facies thickness (m)**	**% facies in whole core**	**% facies in travertine thickness**	**Number logged beds**	**Max thickness (m)**	**Min thickness (m)**	**Cumulative facies thickness (m)**	**% facies in whole core**	**% facies in travertine thickness**
T1	26	0.13	0.005	0.53	**1.5**	2.7	20	0.11	0.005	0.48	**1.1**	**1.4**
T2	58	0.05	0.005	0.85	**2.4**	4.4	15	0.08	0.005	0.24	**0.6**	**0.7**
T3	35	0.03	0.005	0.28	**0.8**	1.3	28	0.055	0.005	0.52	**1.2**	**1.6**
T4	11	0.14	0.005	0.39	**1.1**	2.0	12	0.035	0.005	0.19	**0.4**	**0.6**
T5	20	0.03	0.005	0.26	**0.7**	1.3	3	0.03	0.005	0.05	**0.1**	**0.1**
T6	141	0.17	0.005	3.08	**8.8**	15.7	83	0.08	0.005	1.8	**4.1**	**5.4**
T7	4	0.025	0.005	0.05	**0.1**	0.3	2	0.005	0.005	0.01	**0.02**	**0.03**
T8	30	0.05	0.01	0.66	**1.9**	3.4	94	0.13	0.01	2.88	**6.5**	**8.6**
T9	15	0.2	0.015	1.04	**3.0**	5.4	50	0.57	0.005	3.68	**8.3**	**11.0**
T10	16	0.08	0.01	0.41	**1.2**	1.7	80	0.16	0.005	2.71	**6.1**	**8.1**
T11	11	0.19	0.005	0.63	**1.8**	3.3	66	0.27	0.005	4.1	**9.3**	**12.3**
T12	28	0.11	0.005	0.98	**2.8**	4.4	44	0.12	0.005	1.09	**2.5**	**3.3**
T13	17	2.6	0.005	6.67	**19.1**	34.5	25	0.07	0.005	0.56	**1.3**	**1.7**
T14	1	0.03	0.03	0.03	**0.1**	0.2	2	0.195	0.18	0.38	**0.8**	**0.6**
C1	5	0.06	0.01	0.12	**0.3**	0.6	2	0.06	0.01	0.07	**0.2**	**0.2**
C2	0	0	0	0	**0**	0	33	0.51	0.02	4.92	**11.1**	**14.7**
X	18	0.87	0.02	5.05	**14.4**	15.1	27	0.89	0.02	8.1	**18.3**	**11.3**
F1	0	0	0	0	**0**		1	0.675	0.675	0.67	**1.5**	
F2	2	1.69	0.2	1.89	**5.4**		0	0	0	0	**0**	
F3	0	0	0	0	**0**		1	0.38	0.38	0.38	**0.9**	
F4	4	1.16	0.22	2.17	**6.2**		1	1.19	1.19	1.19	**10.9**	
F5	1	0.2	0.2	0.2	**0.6**		6	0.25	0.04	0.73	**1.6**	**1.8**
F6	11	0.94	0.12	3.88	**11.1**		3	0.69	0.34	1.56	**3.5**	**1.0**
F7	4	0.37	0.13	1.0	**2.9**		12	1.35	0.02	5.24	**11.8**	**13.1**
F8	8	0.94	0.1	3.85	**11.0**		0	0	0	0	**0**	
F9	5	0.44	0.12	1.0	**2.9**	2.7	6	0.6	0.06	1.29	**2.9**	**0.2**
F10	0	0	0	0	**0**		4	0.57	0.18	1.47	**3.3**	**2.2**

Tab. 4 - Distinguished facies type thickness and relative percentage in each analysed core (X = thickness of non-recovered intervals).

springs sourcing units 1-5. This progradational and step-down growth style of travertine depositional systems must be caused by the downward and lateral shifts of the sourcing vents. Similar downstepping growth style with laterally stacked units terminating in onlap against the older strata had been described in other Pleistocene travertines in Central Italy (Della Porta et al. 2017). The depositional model and stratigraphic architecture presented in this study partly differ from Faccenna et al. (2008; their Figure 2) with respect to the shape of the individual stratigraphic units bounded by unconformity surfaces. A direct comparison, however, cannot be discussed due to the limited information about the location of the erosional surfaces identified by Faccenna et al. (2008).

The described pattern of discontinuous sedimentation has been observed in numerous travertine deposits and attributed to intermittent tectonic and volcanic activity, fault movement affecting groundwater flow, or to climatically-controlled fluctuations of the water table and groundwater hydrology or to the combined effect of these parameters (Chafetz & Guidry 2003; Sant'Anna et al. 2004; Faccenna et al. 2008; Rainey & Jones 2009; Özkul et al. 2013; Priewisch et al. 2014; Ronchi & Cruciani 2015; Toker et al. 2015; Berardi et al. 2016; Croci et al. 2016; Claes et al. 2017a; Cook & Chafetz 2017). However, the subaerial exposure of travertines might be simply produced by diversion of the thermal water flow and it is not necessarily due to tectonically or climatically driven interruptions of vent outflow. In the active Mammoth Hot Springs (Yellowstone National Park, USA) travertine system, only 7 % of the surface is covered by a film of flowing thermal water (De Boever et al. 2017), or alternatively there could be more active vents interfering and producing amalgamating sloping fans (Cook & Chafetz 2017). Nevertheless, in the studied Tivoli travertines, units 2 and 3 are characterized by deposition of distal-like facies (T8-T11, T14), rich in coated vegetation, also in the proximal zone underlying the unconformities. This change in depositional conditions with predominance of freshwater marsh facies in the proximal area might suggest some changes in the hydrology of the basin, probably driven by climatic oscillations, as proposed for the Tivoli travertines by Faccenna et al. (2008) and Anzalone et al. (2017).

The Tivoli travertines vs. current travertine definitions

The most recent proposed definition for travertines indicates that hydrothermal travertines are precipitated by thermal water generally with temperature over 30°C and are generally devoid of macrophytes (Capezzuoli et al. 2014). Bacteria and cyanophytes are typically the only associated organic constituents due to the unsuitable water temperature or chemistry for plants and trees to grow (Capezzuoli et al. 2014). However, the studied Tivoli travertines (*lapis tiburtinus*), which provide the name to the whole category of terrestrial carbonates precipitated by thermal water, seem not to exactly match this definition. Present-day springs in the AAB have a temperature of 23°C and, according to the geochemical data and paleotemperature calculations presented in this study, late Pleistocene fossil springs seem to have had values ranging between 16 and 34°C, with average 21-23°C. These temperature values would place the Tivoli travertines at the lower limit or outside the current temperature-based classification of spring carbonates. In the analysed cores, the 5-20 % of the travertine thickness consists of facies with abundant coated reeds and *Charophytes* that should not be included within the travertine definition and could as well be labelled as calcareous tufa (e.g., ambient temperature spring carbonates or meteogene travertine), except for their stable isotope carbon values. In fact, the geochemical signature of the Tivoli travertine facies agrees with the proposed carbon stable isotope values indicative of DIC generated through subsurface geothermal processes (e.g., decarbonation of limestones; magmatic mantle-derived CO_2). However, in Tivoli also the travertine facies with coated macrophytes and *Charophytes* (T8-T11, T14), the post-travertine ostracode sediment filling (C1) and meteoric cement have carbon isotope values falling within the field of thermal spring precipitates. This is because most of the DIC in the Tivoli groundwater lens derives from the mixing of freshwater with cooled thermal water in the travertine aquifer. Hence, the applicability of the classification of spring carbonates based on water temperature, encrusted macro- and microphytes content and geochemical signature remains a matter of debate even for the classical *lapis tiburtinus* from Tivoli. In addition to already discussed controversial examples (cf. Jones & Renaut 2010; Capezzuoli et al. 2014 and

references therein), Camuera et al. (2014) describe in the Canary Islands carbonate spring deposits that have textural characteristics of tufa due to the abundance of macrophytes but with isotopic signature typical of thermogene travertine indicative of deep sourced fluids that probably had temperature of 20-35°C. Travertines from Pleistocene mounds in the Denizli Basin (Turkey) show numerous intervals of coated reed facies and carbon stable isotopes indicative of a contribution of both surface meteoric water and deeply seated thermal CO_2 (Claes et al. 2015). Calculated palaeotemperatures for the travertines in the Denizli Basin are 23-39°C (Özkul et al. 2013) and 26-35°C (Claes et al. 2015).

Even though Capezzuoli et al. (2014) discuss the possible pitfalls of applying temperature-based classifications to the fossil record and evaluate the occurrence of interlayered carbonates with textures resembling freshwater tufa and hydrothermal travertine, in particular in distal reaches of travertine systems, they propose the term "travitufa" to address tufa precipitated by cooled thermal water in peripheral sectors of geothermal regions. This term, descriptive of intermediate or interlayered carbonates with textures similar to travertine or tufa endmembers, might increase the difficulty in classifying spring carbonates. Spring carbonates precipitated by thermal water, while flowing superficially along the topographic gradient, supersaturated with respect to carbonates with DIC originated from geothermal or meteoric karstic processes, include a continuum of facies and facies associations due to the lateral evolution of the environmental conditions, water properties and hydrogeology. Creating a new intermediate category to address the products of a continuum of carbonates precipitated by thermal water, changing its physico-chemical properties while flowing and mixing on the surface topography, might be misleading.

Conclusions

Hydrothermal travertines display heterogeneities at various scales, spanning from millimetre to metre-scale vertical transitions of the different precipitated facies to the decametre to kilometre-scale depositional geometry of geobodies characterized by complex internal stratal patterns. The upper Pleistocene travertines of the Acque Albule Basin (Tivoli, Central Italy) were investigated combining data from six borehole cores, including centimetre-scale facies composition of specific depositional zones, diagenetic features, porosity and oxygen and carbon stable isotope signature, depositional geometry from exposed quarry walls and a 3D digital model produced in Petrel. The studied travertines are wedge-shaped with variable lateral thickness (20-45 m thick), gently dipping and thinning towards the S, E or W. Travertines overlie a tens-of-metres thick succession of Middle Pleistocene deposits comprising lacustrine siltstones and marls with ostracodes, molluscs and *Charophytes*, alluvial plain siltstones and sandstones and pyroclastic deposits from the Sabatini Mts. and Albani Hills volcanic districts. In the southernmost distal area, travertines are intercalated with alluvial fluvial siltstones, parallel to cross-laminated sandstones and conglomerates of the Aniene River, which borders the southern end of the travertine unit. In most of the analysed cores, the onset of hydrothermal travertine precipitation followed the deposition of 1-2 m thick organic matter-rich mudstone of marsh environment.

Travertine stable isotope data indicate average values per core of $\delta^{13}C$ from 9.2 ‰ to 10.1 ‰ and $\delta^{18}O$ from -6.8 ‰ to -6.1 ‰, confirming the geothermal origin of the precipitating spring water.

The vertical and lateral distribution of the travertine facies in the analysed cores reflects the different environments of deposition across a nearly 3 km long, N-S transect. The travertine system is subdivided into three zones (proximal, intermediate and distal) with respect to the inferred location of the feeding hydrothermal vents in the N-NE. The proximal depositional zone in the north (cores S1, S2 and S3), closer to the inferred active vents, is characterized by deposition in horizontal to gently dipping decametre-size pools belonging to a low-angle terraced system with facies types indicative of slow flowing thermal water (clotted peloidal micrite dendrites boundstone, radial coated grain grainstone, coated reeds, rafts and coated gas bubble boundstone). The intermediate zone, nearly 2 km southward, includes cores S4 and S5-S6 and represents a smooth to terraced slope setting, with beds dipping 5-40° southward and eastward, dominated by facies types indicative of fast-flowing thermal water (crystalline dendrite cementstone, laminated boundstone and radial coated grain grainstone).

The distal southern core S7 consists of lobes dipping southward, eastward and westward of low-angle smooth and terraced slope systems adjacent to marshes dominated by carbonate encrusted vegetation and *Charophytes*, alternating with alluvial-fluvial terrigenous deposits.

The travertine succession is marked by numerous centimetre- to metre-thick clayey intraclastic/extraclastic wackestone to floatstone/rudstone indicative of non-deposition and erosion, due to temporary interruption or diversion of thermal water flow direction. These unconformities allow distinguishing nine depositional units, prograding southward. The wedge geometry of the Tivoli travertine depositional system is the result of the geometry of the individual units and the way units stack vertically and laterally due to changes in the location of the active vents. The geometry of the individual fan-shaped units is influenced by the topographic gradient and rates of thermal water discharge and carbonate precipitation. The pattern of vertical and lateral superimposition of the travertine units is controlled by the intermittent vent activity and changes in the location of the active vents, shifting through time to lower elevations with respect to the topographic gradient.

Acknowledgements. Statoil ASA is thanked for making the travertine cores available for investigation and for providing the high-resolution georeferenced photographs of the quarry walls, the digitized stratigraphic surfaces and the porosity and permeability data. In particular, the authors wish to thank Klaas Verwer, Giulio Casini and Fabio Lapponi (Statoil) for supporting the project. E. Capezzuoli (Perugia University) is thanked for introducing to the travertine quarry area. The authors would like to thank Monica Dapiaggi (Milan University) for the XRD analyses, Curzio Malinverno (Milan University) for thin-section preparation and Agostino Rizzi (CNR, Milan University) for SEM analysis. Schlumberger is thanked for providing the academic license for Petrel. The Editors, Paul Wright and an anonymous reviewer are warmly thanked for their constructive comments.

References

Allen C.C., Albert F.G., Chafetz H.S., Combie J., Graham C.R., Kieft T.L., Kivett S.J., McKay D.S., Steele A., Taunton, A.E. & Taylor M.R. (2000) - Microscopic physical biomarkers in carbonate hot springs: implications in the search for life on Mars. *Icarus*, 147(1): 49-67.

Alvarenga R.S., Iacopini D., Kuchle J., Scherer C.M.S. & Goldberg K. (2016) - Seismic characteristics and distribution of hydrothermal vent complexes in the Cretaceous offshore rift section of the Campos Basin, offshore Brazil. *Mar. Pet. Geol.*, 74: 12-25.

Anzalone E. (2008) - Late Pleistocene travertines and their analogues under deposition. A comparative analysis. *Italian J. Quat. Sci.*, 21: 91-98.

Anzalone E., D'Argenio B. & Ferreri V. (2017) - Depositional trends of travertines in the type area of Tivoli (Italy). *Rend. Fis. Acc. Lincei,* 28(2): 341-361

Apolinarska K., Pelechaty M. & Pukacz A. (2011) - Sedimentation by modern charophytes (Characeae): can calcified remains and carbonate $\delta^{13}C$ and $\delta^{18}O$ record the ecological state of lakes? *Studia Limnologica et Telmatologica*, 5: 55-66.

Berardi G., Vignaroli G., Billi A., Rossetti F., Soligo M., Kele S., Baykara M.O., Bernasconi S.M., Castorina F., Tecce F. & Shen C.C. (2016) - Growth of a Pleistocene giant carbonate vein and nearby thermogene travertine deposits at Semproniano, southern Tuscany, Italy: Estimate of CO_2 leakage. *Tectonophysics*, 690: 219-239.

Bertini A., Minissale A. & Ricci M. (2014) - Palynological approach in upper Quaternary terrestrial carbonates of central Italy: anything but a 'mission impossible'. *Sedimentology*, 61(1): 200-220.

Bigi G., Cosentino D., Parotto M., Sartori R. & Scandone P. (1990) - Structural Model of Italy 1: 500,000. La Ricerca Scientifica, Quaderni, C.N.R. 114 (3).

Billi A., Tiberti M.M., Cavinato G.P., Cosentino D., Di Luzio E., Keller J.V.A., Kluth C., Orlando L., Parotto M., Praturlon A., Romanelli M., Storti F. & Wardell N. (2006) - First results from the CROP-11 deep seismic profile, central Apennines, Italy: evidence of mid-crustal folding. *J. Geological Society London*, 163: 583-586.

Bollati A., Corrado S., Cosentino D., Marino M., Mattei M. & Parotto M. (2011) - Structural scheme of the Umbria-Sabina fold-and-thrust belt (Central Italy) derived from the geological mapping of 366 "Palombara Sabina" and 375 "Tivoli" sheets (CARG Project). *Rend. Online Soc. Geol. It.*, 14: 37-61.

Bollati A., Corrado S. & Marino M. (2012) - Inheritance of Jurassic rifted margin architecture into the Apennines Neogene mountain building: a case history from the Lucretili Mts. (Latium, Central Italy). *Int. J. Earth Sci.*, 101: 1011-1031.

Brogi A. & Capezzuoli E. (2009) - Travertine deposition and faulting: the fault-related travertine fissure-ridge at Terme S. Giovanni, Rapolano Terme (Italy). *Int. J. Earth Sci.*, 98(4): 931-947

Brogi A., Capezzuoli E., Aqué R., Branca M. & Voltaggio M. (2010) - Studying travertines for neotectonics investigations: Middle–Late Pleistocene syn-tectonic travertine deposition at Serre di Rapolano (Northern Apennines, Italy). *Int. J. Earth Sci.*, 99(6): 1383-1398.

Brogi A., Capezzuoli E., Kele S., Baykara M.O. & Shen C.C. (2017) - Key travertine tectofacies for neotectonics and palaeoseismicity reconstruction: effects of hydrothermal overpressured fluid injection. *J. Geol. Soc.* Published Online First. https://doi.org/10.1144/jgs2016-124

Brogi A., Liotta D., Ruggieri G., Capezzuoli E., Meccheri M. & Dini A. (2016) - An overview on the characteristics of geothermal carbonate reservoirs in southern Tuscany.

Ital. J. Geosci., 135(1): 17-29.

Brunetti E., Jones J.P., Petitta M. & Rudolph D.L. (2013) - Assessing the impact of large-scale dewatering on fault-controlled aquifer systems: a case study in the Acque Albule basin (Tivoli, central Italy). *Hydrogeol. J.*, 21:401-423.

Camuera J., Alonso-Zarza A.M., Rodríguez-Berriguete Á. & Rodriguez-Gonzalez A. (2014) - Origin and palaeoenvironmental significance of the Berrazales carbonate spring deposit, North of Gran Canaria Island, Spain. *Sediment. Geol.*, 308: 32-43.

Capezzuoli E., Gandin A. & Pedley M. (2014) - Decoding tufa and travertine (fresh water carbonates) in the sedimentary record: the state of the art. *Sedimentology*, 61:1-21.

Carminati E. & Doglioni C. (2012) - Alps vs. Apennines: the paradigm of a tectonically asymmetric Earth. *Earth-Sci. Rev.*, 112(1): 67-96.

Carucci V., Petitta M., Aravena R. (2012) - Interaction between shallow and deep aquifers in the Tivoli Plain (Central Italy) enhanced by groundwater extraction: A multi-isotope approach and geochemical modeling. *Appl. Geochem.*, 27: 266-280.

Chafetz H.S. (2013) - Porosity in bacterially induced carbonates: Focus on micropores. *AAPG Bulletin*, 97(11): 2103-2111.

Chafetz H.S. & Folk R.L. (1984) - Travertines: depositional morphology and the bacterially constructed constituents. *J. Sed. Res*, 54: 289-316.

Chafetz H.S & Guidry S.A. (2003) - Deposition and diagenesis of Mammoth Hot Springs travertine, Yellowstone National Park, Wyoming, U.S.A. *Can. J. Earth Sci.*, 40: 1515–1529.

Chafetz, H.S. & Guidry S.A. (1999) - Bacterial shrubs, crystal shrubs, and ray-crystal shrubs: bacterial vs. abiotic precipitation. *Sediment. Geol.*, 126(1): 57-74.

Chafetz H.S., Rush P.F. & Utech N.M. (1991) - Microenvironmental controls on mineralogy and habit of $CaCO_3$ precipitates: an example from an active travertine system. *Sedimentology*, 38(1): 107-126.

Chafetz H.S., Wilkinson B.H. & Love K.M. (1985) - Morphology and composition of non-marine carbonate cements in near-surface settings. In: Schneidermann N. & Harris P.M. (Eds) - Carbonate cements. *SEPM Spec. Publ.*, 36: 337-347. Soc. Econ. Paleont. Min.

Claes H., Degros M., Soete J., Claes S., Kele S., Mindszenty A., Török Á., El Desouky H., Vanhaecke F. & Swennen R. (2017a) - Geobody architecture, genesis and petrophysical characteristics of the Budakalász travertines, Buda Hills (Hungary). *Quat. Int.*, 437: 107-128.

Claes H., Erthal M.M., Soete J., Özkul M. & Swennen R. (2017b) - Shrub and pore type classification: Petrography of travertine shrubs from the Ballık-Belevi area (Denizli, SW Turkey). *Quat. Int.*, 437: 147-163.

Claes H., Soete J., Van Noten K., El Desouky H., Erthal M.M., Vanhaecke F., Özkul M. & Swennen R. (2015) - Sedimentology, three-dimensional geobody reconstruction and carbon dioxide origin of Pleistocene travertine deposits in the Ballık area (south-west Turkey). *Sedimentology*, 62(5): 1408-1445.

Cook M. & Chafetz H.S. (2017) - Sloping fan travertine, Belen, New Mexico, USA. *Sediment. Geol.*, 352: 30–44.

Corrado S., Cosentino D., Crescenzi B. & Parotto M. (1992) - Geometrie delle deformazioni della Sabina meridionale attraverso la ricostruzione di superfici strutturali (Lazio, Appennino Centrale). In: Tozzi M., Cavinato G.P. & Parotto M. (Eds) - Studi preliminari all'acquisizione dati del profilo CROP 11 Civitavecchia-Vasto. *Studi Geologici Camerti*: 42-53.

Cosentino D. & Parotto M. (1986) - Assetto strutturale dei Monti Lucretili settentrionali (Sabina): nuovi dati e schema tettonico preliminare. *Geologica Romana*, 25: 73-90.

Costa K.C., Navarro J.B., Shock E.L., Zhang C.L., Soukup D. & Hedlund B.P. (2009) - Microbiology and geochemistry of great boiling and mud hot springs in the United States Great Basin. *Extremophiles*, 13(3): 447-459. DOI 10.1007/s00792-009-0230-x.

Croci A., Della Porta G. & Capezzuoli E. (2016) - Depositional architecture of a mixed travertine-terrigenous system in a fault-controlled continental extensional basin (Messinian, Southern Tuscany, Central Italy). *Sediment. Geol.*, 332: 13-39.

D'Argenio B. & Ferreri V. (1986) - A brief outline of sedimentary models for Pleistocene travertine accumulation in southern Italy. *Rend. Soc. Geol. It.*, 9: 167-170.

D'Argenio B., Ferreri V. & Anzalone E. (2008) - Travertines and carbonate platforms. Geometries and evolutionary trend. *Rend. Soc. Geol. It.*, 2: 67-72.

De Boever E., Foubert A., Lopez B., Swennen R., Jaworowski C., Özkul M. & Virgone A. (2017) - Comparative study of the Pleistocene Cakmak quarry (Denizli Basin, Turkey) and modern Mammoth Hot Springs deposits (Yellowstone National Park, USA). *Quat. Int.*, 437: 129-146.

De Boever E., Foubert A., Oligschlaeger D., Claes S., Soete J., Bertier P., Özkul M., Virgone A. & Swennen R. (2016) - Multiscale approach to (micro) porosity quantification in continental spring carbonate facies: Case study from the Cakmak quarry (Denizli, Turkey). *Geochem., Geophy., Geosyst.*, 17(7): 2922-2939.

De Filippis L., Anzalone E., Billi A., Faccenna C., Poncia P.P. & Sella P. (2013a) - The origin and growth of a recently-active fissure ridge travertine over a seismic fault, Tivoli, Italy. *Geomorphology*, 195: 13-26.

De Filippis L. & Billi A. (2012) - Morphotectonics of fissure ridge travertines from geothermal areas of Mammoth Hot Springs (Wyoming) and Bridgeport (California). *Tectonophysics*, 548–549: 34-48.

De Filippis L., Faccenna C., Billi A., Anzalone E., Brilli M., Özkul M., Soligo M., Tuccimei P. & Villa I.M. (2012) - Growth of fissure ridge travertines from geothermal springs of Denizli basin, western Turkey. *Geol. Soc. Am. Bulletin*, 124: 1629–1645.

De Filippis L., Faccenna C., Billi A., Anzalone E., Brilli M., Soligo M. & Tuccimei P. (2013b) - Plateau versus fissure ridge travertines from Quaternary geothermal springs of Italy and Turkey: Interactions and feedbacks between fluid discharge, paleoclimate, and tectonics. *Earth-Sci. Rev.*, 123: 35-52.

Della Porta G. (2015) - Carbonate build-ups in lacustrine, hydrothermal and fluvial settings: comparing depositional geometry, fabric types and geochemical signature In: Bosence D.W.J., Gibbons K.A., Le Heron D.P., Morgan W.A., Pritchard T. & Vining B.A. (Eds) - Microbial Carbonates in Space and Time: Implications for Global Exploration and Production. *Geol. Soc. London Spec. Publ.*, 418: 17-68.

Della Porta G., Capezzuoli E. & De Bernardo A. (2017) - Facies character and depositional architecture of hydrothermal travertine slope aprons (Pleistocene, Acquasanta Terme, Central Italy), *Mar. Pet. Geol.*, 87: 171-187.

De Rita D., Faccenna C., Funiciello R. & Rosa C. (1995) - Structural and geological evolution of the Colli Albani volcanic district. In: Trigila R. (Ed) - The Volcano of the Alban Hills. Rome: Tipografia SGS: 33–71.

De Rita D., Giordano G., Esposito A., Fabbri M. & Rodani S. (2002) - Large volume phreatomagmatic ignimbrites from the Colli Albani volcano (Middle Pleistocene, Italy). *J. Volc. Geoth. Res.*, 118: 77-98.

Di Benedetto F., Montegrossi G., Minissale A., Pardi L.A., Romanelli M., Tassi F., Delgado Huertas A., Pampin E.M., Vaselli O. & Borrini D. (2011) - Biotic and inorganic control on travertine deposition at *Bullicame 3* spring (Viterbo, Italy): a multidisciplinary approach. *Geochim. Cosmochim. Acta*, 75: 4441-4455.

Di Salvo C., Mazza R. & Capelli G. (2013) - Gli acquiferi in travertino del Lazio: schemi idrogeologici e caratteristiche chimico-fisiche. *Rend. Online Soc. Geol. It.*, 27: 54-76.

Doglioni C. (1991) - A proposal for the kinematic modelling of W-dipping subductions – possible applications to the Tyrrhenian-Apennines system. *Terra Nova*, 3: 423-434.

Durand O. (2011) - Reservoir characterization of the Lapis Tiburtinus travertine system (Tivoli, Italy). Master Thesis Institut Polytechnique Lasalle Beauvais. Mémoire d'Ingénier Géologique, 468, 131 pp.

Erthal M.M., Capezzuoli E., Mancini A., Claes H., Soete J. & Swennen R. (2017) - Shrub morpho-types as indicator for the water flow energy – Tivoli travertine case (Central Italy). *Sediment. Geol.*, 347: 79-99.

Faccenna C., Funiciello R., Bruni A., Mattei M. & Sagnotti L. (1994a) - Evolution of a transfer related basin: the Ardea basin (Latium, Central Italy). *Basin Res.*, 5: 1-11.

Faccenna C., Funiciello R. & Mattei M. (1994b) - Late Pleistocene N–S shear zones along the Latium Tyrrhenian margin: structural characters and volcanological implications. *Boll. Geofis. Teor. Appl.*, 36: 507–522.

Faccenna C., Funiciello R., Montone P., Parotto M. & Voltaggio M. (1994c) - Late Pleistocene strike-slip tectonics in the Acque Albule Basin (Tivoli, Latium). *Mem. Descr. Carta Geologica d'Italia*, 49, 37–50.

Faccenna C., Soligo M., Billi A., De Filippis L., Funiciello R., Rossetti C. & Tuccimei P. (2008) - Late Pleistocene depositional cycles of the Lapis Tiburtinus travertine (Tivoli, Central Italy): Possible influence of climate and fault activity. *Glob. Planet. Change*, 63: 299-308.

Folk R.L. (1993) - SEM imaging of bacteria and nannobacteria in carbonate sediments and rocks. *J. Sediment. Petrol.*, 63(5): 990-999.

Folk R.L. & Chafetz H.S. (1983) - V. 4 Pisoliths (Pisoids) in Quaternary Travertines of Tivoli, Italy. In: Peryt T.M. (Ed) - Coated grains, 474-487, Springer-Verlag, Berlin Heidelberg.

Folk R.L., Chafetz H.S. & Tiezzi P.A. (1985) - Bizarre forms of depositional and diagenetic calcite in hot- spring travertines, central Italy. In: Schneidermann N. & Harris P.M. (Eds) - Carbonate cements. *SEPM Spec. Publ.*, 36: 349-369.

Ford T.D. & Pedley H.M. (1996) - A review of tufa and travertine deposits of the world. *Earth-Sci. Rev.*, 41: 117-175.

Fouke B.W. (2011) - Hot-spring Systems Geobiology: abiotic and biotic influences on travertine formation at Mammoth Hot Spring, Yellowstone National Park, USA. *Sedimentology*, 58: 170-219.

Fouke B.W., Farmer J.D., Des Marais D.J., Pratt L., Sturchio N.C., Burns P.C., Discipulo M.K. (2000) - Depositional facies and aqueous-solid geochemistry of travertine depositing hot springs (Angel Terrace, Mammoth Hot Springs, Yellowstone National Park, USA). *J. Sediment. Res.*, 70: 265-285.

Fouke B.W., Bonheyo G.T., Sanzenbacher B. & Frias-Lopez J. (2003) - Partitioning of bacterial communities between travertine depositional facies at Mammoth Hot Springs, Yellowstone National Park, USA. *Can. J. Earth Sci.*, 40(11): 1531-1548..

Frery E., Gratier J.P., Ellouz-Zimmerman N., Deschamps P., Blamart D., Hamelin B. & Swennen R. (2017) - Geochemical transect through a travertine mount: A detailed record of CO 2-enriched fluid leakage from Late Pleistocene to present-day–Little Grand Wash fault (Utah, USA). *Quat. Int.*, 437: 98-106.

Funiciello R., Giordano G. & De Rita D. (2003) - The Albano maar lake (Colli Albani Volcano, Italy): recent volcanic activity and evidence of pre-Roman Age catastrophic lahar events. *J. Volcan. Geoth. Res.*, 123: 43-61.

Gaeta M., Fabrizio G. &. Cavarretta G. (2000) - F-phlogopites in the Alban Hills Volcanic District (Central Italy): indications regarding the role of volatiles in magmatic crystallisation. *J. Volcan. Geoth. Res.*, 99: 179-193.

Gandin A. & Capezzuoli E. (2008) - Travertine vs. calcareous tufa: distinctive petrologic features and stable isotope signatures. *It. J. Quat. Sci.*, 21: 125-136.

Gandin A. & Capezzuoli E. (2014) - Travertine: distinctive depositional fabrics of carbonates from thermal spring systems. *Sedimentology*, 61: 264-290.

Gierlowski-Kordesch E.H. (2010) - Lacustrine carbonates. In: Alonso-Zarza A.M. & Tanner L.H. (Eds) - Carbonates in continental settings: facies, environments and processes. Developments in Sedimentology, 61: 1-101. Elsevier, Amsterdam.

Gonfiantini R., Panichi C. & Tongiorgi E. (1968) - Isotopic disequilibrium in travertine deposition. *Earth Planet. Sci. Lett.*, 5: 55-58.

Gradziński M., Wróblewski W., Duliński M. & Hercman H. (2014) - Earthquake-affected development of a travertine ridge. *Sedimentology*, 61(1): 238-263.

Gueguen E., Doglioni C. & Fernandez M. (1997) - Lithospheric boudinage in the Western Mediterranean back-arc basin. *Terra Nova*, 9(4): 184-187.

Guido D.M. & Campbell K.A. (2011) - Jurassic hot spring deposits of the Deseado Massif (Patagonia, Argentina): characteristics and controls on regional distribution. *J. Volcan. Geoth. Res.*, 203(1): 35-47.

Guo L., Andrews J., Riding R., Dennis P. & Dresser Q. (1996) - Possible microbial effects on stable carbon isotopes in hot-spring travertines. *J. Sediment. Res.*, 66: 468-473.

Guo L. & Riding R. (1992) - Aragonite laminae in hot water travertine crusts, Rapolano Terme, Italy. *Sedimentology*, 39: 1067-1079.

Guo L. & Riding R. (1994) - Origin and diagenesis of Quaternary travertine shrub fabrics, Rapolano Terme, central Italy. *Sedimentology*, 41: 499-520.

Guo L. & Riding R. (1998) - Hot-spring travertine facies and sequences, Late Pleistocene, Rapolano Terme, Italy. *Sedimentology*, 45: 163-180.

Guo L. & Riding R. (1999) - Rapid facies changes in Holocene fissure ridge hot spring travertines, Rapolano Terme, Italy. *Sedimentology*, 46: 1145-1158.

Hammer Ø., Dysthe D.K. & Jamtveit B. (2010) - Travertine terracing: patterns and mechanisms. In: Pedley H.M. & Rogerson M. (Eds) - Tufas and Speleothems: Unravelling the Microbial and Physical Controls. *Geological Society of London Special Publication*, 336: 345–355.

Hancock P.L., Chalmers R.M.L., Altunel E. & Çakir Z. (1999) - Travitonics: using travertines in active fault studies. *J. Struct. Geol.*, 21(8): 903-916.

Jones B. & Peng X. (2012) - Intrinsic versus extrinsic controls on the development of calcite dendrite bushes, Shuzhishi Spring, Rehai geothermal area, Tengchong, Yunnan Province, China. *Sediment. Geol.*, 249: 45-62.

Jones B. & Peng X. (2014a) - Multiphase calcification associated with the atmophytic cyanobacterium *Scytonema julianum*. *Sediment. Geol.*, 313: 91-104.

Jones B. & Peng X. (2014b) - Signatures of biologically influenced $CaCO_3$ and Mg–Fe silicate precipitation in hot springs: Case study from the Ruidian geothermal area, western Yunnan Province, China. *Sedimentology*, 61: 56-89.

Jones B. & Peng X. (2014c). Hot spring deposits on a cliff face: A case study from Jifei, Yunnan Province, China. *Sediment. Geol.*, 302: 1-28.

Jones B. & Renaut R.W. (1995). Noncrystallographic calcite dendrites from hot-spring deposits at Lake Bogoria, Kenya. *J. Sediment. Res.*, 65: 154-169.

Jones B. & Renaut R.W. (2010) - Calcareous spring deposits in continental settings. In: Alonso-Zarza A.M. & Tanner L.H. (Eds) - Carbonates in continental settings: facies, environments and processes. Developments in Sedimentology, 61: 177-224. Elsevier, Amsterdam.

Karner D.B., Marra F. & Renne P.R. (2001) - The history of the Monti Sabatini and Alban Hills volcanoes: groundwork for assessing volcanic-tectonic hazards for Rome. *J. Volcan. Geothe. Res.*, 107: 185-219.

Kele S., Breitenbach S.F., Capezzuoli E., Meckler A.N., Ziegler M., Millan I.M., Kluge T., Deák J., Hanselmann K., John C.M. & Yan H. (2015) - Temperature dependence of oxygen-and clumped isotope fractionation in carbonates: a study of travertines and tufas in the 6–95°C temperature range. *Geochim. Cosmochim. Acta*, 168: 172-192.

Kele S., Demeny A., Siklosy Z., Nemeth T., Toth M. & Kovacs M.B. (2008) Chemical and stable isotope composition of recent hot-water travertines and associated thermal waters, from Egerszalok, Hungary: depositional facies and nonequilibrium fractionation. *Sediment. Geol.*, 211: 53-72.

Kele S., Özkul M., Gökgöz A., Forizs I., Baykara M.O., Alçiçek M.C. & Nemeth T. (2011) - Stable isotope geochemical and facies study of Pamukkale travertines: new evidences of low-temperature non-equilibrium calcite-water fractionation. *Sediment. Geol.*, 238: 191-212.

Kufel L. & Kufel I. (2002) - Chara beds acting as nutrient sinks in shallow lakes - a review. *Aquatic Botany*, 72(3): 249-260.

La Vigna F., Hill M.C., Rossetto R. & Mazza R. (2016) - Parameterization, sensitivity analysis, and inversion: an investigation using groundwater modeling of the surface-mined Tivoli-Guidonia basin (Metropolitan City of Rome, Italy). *Hydrogeol. J.*, 24(6): 1423-1441.

La Vigna F., Mazza R. & Capelli G. (2013a) - Water resources in the travertines of Tivoli-Guidonia plain. Numerical modeling as a tool for aquifer management. Le risorse idriche nei travertini della piana di Tivoli-Guidonia. La modellazione numerica come strumento di gestione degli acquiferi. *Rend. Online Soc. Geol. Ital.*, 27: 77-85, doi: 10.3301/ROL.2013.21.

La Vigna F., Mazza R. & Capelli G. (2013b) - Detecting the flow relationships between deep and shallow aquifers in an exploited groundwater system, using long-term monitoring data and quantitative hydrogeology: the Acque Albule basin case (Rome, Italy). *Hydrolog. Proces.,* 27: 3159–3173.

Langangen A. (2000). - *Charophytes* from the warm springs of Svalbard. *Polar Res.*, 19: 143-153.

Lopez B., Camoin G., Özkul M., Swennen R. & Virgone A. (2017) - Sedimentology of coexisting travertine and tufa deposits in a mounded geothermal spring carbonate system, Obruktepe, Turkey. *Sedimentology*, 64(4): 903-931.

Malinverno A. & Ryan W.B.F. (1986) - Extension in the Tyrrhenian Sea and shortening in the Apennines as result of arc migration driven by sinking of the lithosphere. *Tectonics*, 5: 227-254.

Mancini M., Marini M., Moscatelli M., Pagliaroli A., Stigliano F., Di Salvo C., Simionato M., Cavinato G.P. & Corazza A. (2014) - A physical stratigraphy model for seismic microzonation of the Central Archaeological Area of Rome (Italy). *Bulletin Earthquake Engineering*, 12(3): 1339-1363.

Marra F., Karner D.B., Freda C., Gaeta M. & Renne P. (2009) - Large mafic eruptions at Alban Hills Volcanic District (Central Italy): chronostratigraphy, petrography and eruptive behavior. *J. Volcan. Geotherm. Res.*, 179: 217–232.

Milli S., Mancini M., Moscatelli M., Stigliano F., Marini M. &

Cavinato G.P. (2016) - From river to shelf, anatomy of a high-frequency depositional sequence: the Late Pleistocene to Holocene Tiber depositional sequence. *Sedimentology*, 63(7): 1886-1928.

Minissale A. (2004) - Origin, transport and discharge of CO_2 in central Italy. *Earth-Sci. Rev.*, 66: 89–141.

Minissale A., Kerrick D.M., Magro G., Murrell M.T., Paladini M., Rihs S., Sturchio N.C., Tassi F. & Vaselli O. (2002) - Geochemistry of Quaternary travertines in the region north of Rome (Italy): structural, hydrologic, and paleoclimatic implications. *Earth Planet. Sc. Lett.*, 203: 709–728.

Murru M., Ferrara C., Matteucci R. & Da Pelo S. (2007) - I depositi carbonatici palustrini paleocenici della Sardegna centro-meridionale (Italia). *Geologica Romana*, 40: 201-213.

Norris T.B. & Castenholz R.W. (2006) - Endolithic photosynthetic communities within ancient and recent travertine deposits in Yellowstone National Park. *FEMS Microbiol. Ecol.*, 57(3): 470-483.

Okumura T., Takashima C., Shiraishi F. & Kano A. (2012) - Textural transition in an aragonite travertine formed under various flow conditions at Pancuran Pitu, Central Java, Indonesia. *Sediment. Geol.*, 265: 195-209.

Özkul M., Kele S., Gökgöz A., Shen C.C., Jones B., Baykara M.O., Fòrizs I., Németh T., Chang Y.W. & Alçiçek M.C. (2013) - Comparison of the Quaternary travertine sites in the Denizli extensional basin based on their depositional and geochemical data. *Sediment. Geol.*, 294: 179-204.

Panichi C. & Tongiorgi E. (1976) - Carbon isotopic composition of CO2 from springs, fumaroles, mofettes and travertines of central and southern Italy: a preliminary prospection method of geothermal areas. Proceedings of the 2nd U.N. Symposium on the Development and Use of Geothermal Energy, San Francisco, U.S.A., 20–29 May 1975: 815–825.

Patacca E., Sartori R. & Scandone P. (1992) - Tyrrhenian basin and Apenninic arcs: kinematic relations since late Tortonian times. *Mem. Soc. Geol. It.*, 45: 425-451.

Pedley H.M. (1990) - Classification and environmental models of cool freshwater tufas. *Sediment. Geol.*, 68: 143-154.

Pełechaty M., Pukacz A., Apolinarska K., Pełechata A. & Siepak M. (2013) - The significance of Chara vegetation in the precipitation of lacustrine calcium carbonate. *Sedimentology*, 60: 1017-1035.

Pentecost A. (1990) - The formation of travertine shrubs: Mammoth Hot Springs, Wyoming. *Geol. Mag.*, 127: 159-168.

Pentecost A. (1995) - The Quaternary travertine deposits of Europe and Asia Minor. *Quat. Sci. Rev.*, 14: 1005-1028.

Pentecost A. (2005) - Travertine. Springer, Berlin Heidelberg, 445 pp.

Pentecost A., Andrews J.E., Dennis P.F., Marca-Bell A. & Dennis S. (2006) - Charophyte growth in small temperate water bodies: extreme isotopic disequilibrium and implications for the palaeoecology of shallow marl lakes. *Palaeogeogr., Palaeoclimatol., Palaeoecol.*, 240: 389-404.

Pentecost A. & Coletta P. (2007) - The role of photosynthesis and CO_2 evasion in travertine formation: A quantitative investigation at an important travertine-depositing hot spring, Le Zitelle, Lazio, Italy. *J. Geol. Soc.*, 164: 843-853.

Pentecost A. & Tortora C. (1989) - Bagni di Tivoli, Lazio: a modern travertine depositing site and its associated microorganisms. *Boll. Soc. Geol. It.*, 108: 315–324.

Pentecost A. & Viles H. (1994) - A review and reassessment of travertine classification. *Geograph. Phys. Quatern.*, 48: 305-314.

Petitta M., Primavera P., Tuccimei P. & Aravena R. (2010) - Interaction between deep and shallow groundwater systems in areas affected by Quaternary tectonics (Central Italy): a geochemical and isotope approach. *Environm. Earth Sci.*, 63: 11-30.

Pola M., Gandin A., Tuccimei P., Soligo M., Deiana R., Fabbri P. & Zampieri D. (2014) - A multidisciplinary approach to understanding carbonate deposition under tectonically controlled hydrothermal circulation: a case study from a recent travertine mound in the Euganean hydrothermal system, northern Italy. *Sedimentology*, 61(1): 172-199.

Priewisch A., Crossey L.J., Karlstrom K.E., Polyak V.J., Asmerom Y., Nereson A. & Ricketts J.W. (2014) - U-series geochronology of large-volume Quaternary travertine deposits of the southeastern Colorado Plateau: Evaluating episodicity and tectonic and paleohydrologic controls. *Geosphere*, 10(2): 401-423.

Rainey D.K. & Jones B. (2009) - Abiotic versus biotic controls on the development of the Fairmont Hot Springs carbonate deposit, British Columbia, Canada. *Sedimentology*, 56: 1832-1857.

Rey-Boissezon A. & Joye D.A. (2015) - Habitat requirements of charophytes—Evidence of species discrimination through distribution analysis. *Aquatic Botany*, 120: 84-91.

Reysenbach A.L., Ehringer M. & Hershberger K. (2000) - Microbial diversity at 83°C in Calcite Springs, Yellowstone National Park: another environment where the *Aquificales* and "Korarchaeota" coexist. *Extremophiles*, 4(1): 61-67.

Rodríguez-Berriguete Á., Alonso-Zarza A.M. & Martín-García R. (2017) - Diagenesis of continental carbonate country rocks underlying surficial travertine spring deposits. *Quat. Int.*, 437: 4-14.

Ronchi P. & Cruciani F. (2015) - Continental carbonates as a hydrocarbon reservoir, an analog case study from the travertine of Saturnia, Italy. *AAPG Bulletin*, 99(4): 711-734.

Sabato Ceraldi T. & Green D. (2017) - Evolution of the South Atlantic lacustrine deposits in response to Early Cretaceous rifting, subsidence and lake hydrology. In: Sabato Ceraldi T., Hodgkinson R.A. & Backe G. (Eds). Petroleum Geoscience of the West Africa Margin, *Geol. Soc. London Spec. Publ.*, 438: 77-98.

Saller A., Rushton S., Buambua L., Inman K., McNeil R. & Dickson J.T. (2016) - Presalt stratigraphy and depositional systems in the Kwanza Basin, offshore Angola. *AAPG Bulletin*, 100: 1135-1164.

Sant'Anna L.G., Riccomini C., Rodrigues-Francisco B.H., Sial

A.N., Carvalho M.D. & Moura C.A.V. (2004) - The Paleocene travertine system of the Itaboraı basin, Southeastern Brazil. *J. S. Am. Earth Sci.*, 18: 11-25.

Serri G., Innocenti F. & Manetti P. (1993) - Geochemical and petrological evidence of the subduction of delaminated Adriatic continental lithosphere in the genesis of the Neogene–Quaternary magmatism of Central Italy. *Tectonophysics*, 223: 117-147.

Serri G., Innocenti F., Manetti P., Tonarini S. & Ferrara G. (1992) - Il magmatismo neogenico quaternario dell'area tosco-laziale-umbra: implicazioni sui modelli di evoluzione geodinamica dell'Appennino settentrionale. *Studi Geologici Camerti*, 1991(1): 429-463.

Soete J., Kleipool L.M., Claes H., Claes S., Hamaekers H., Kele S., Özkul M., Foubert A., Reijmer J.J.G. & Swennen R. (2015) - Acoustic properties in travertines and their relation to porosity and pore types. *Mar. Pet. Geol.*, 59: 320-335.

Sugihara C., Yanagawa K., Okumura T., Takashima C., Harijoko A. & Kano A. (2016) - Transition of microbiological and sedimentological features associated with the geochemical gradient in a travertine mound in northern Sumatra, Indonesia. *Sediment. Geol.*, 343: 85-98.

Teboul P.A., Durlet C., Gaucher E.C., Virgone A., Girard J.P., Curie J., Lopez B. & Camoin G.F. (2016) -Origins of elements building travertine and tufa: New perspectives provided by isotopic and geochemical tracers. *Sediment. Geol.*, 334: 97-114.

Toker E., Kayseri-Özer M.S., Özkul M. & Kele S. (2015) - Depositional system and palaeoclimatic interpretations of Middle to Late Pleistocene travertines: Kocabaş, Denizli, south-west Turkey. *Sedimentology*, 62(5): 1360-1383.

Török Á., Mindszenty A., Claes H., Kele S., Fodor L. & Swennen R. (2017) - Geobody architecture of continental carbonates: "Gazda" travertine quarry (Süttő, Gerecse Hills, Hungary). *Quat. Int.*, 437: 164-185.

Van Noten K., Claes H., Soete J., Foubert A., Özkul M. & Swennen R. (2013) - Fracture networks and strike–slip deformation along reactivated normal faults in Quaternary travertine deposits, Denizli Basin, western Turkey. *Tectonophysics*, 588: 154-170.

Wang Z., Meyer M.C. & Hoffmann D.L. (2016) - Sedimentology, petrography and early diagenesis of a travertine–colluvium succession from Chusang (southern Tibet). *Sediment. Geol.*, 342: 218-236.

Wright V.P. (2012) - Lacustrine carbonates in rift settings: the interaction of volcanic and microbial processes on carbonate deposition. In: Garland J., Neilson J.E., Laubach S.E. & Whidden K.J. (Eds) - Advances in Carbonate Exploration and Reservoir Analysis. *Geol. Soc. London Spec. Publ.*, 370: 39-47.

Wright V.P. & Barnett A. (2015) - An abiotic model for the development of textures in some South Atlantic early Cretaceous lacustrine carbonates. In: Bosence D.W.J., Gibbons K.A., Le Heron D.P., Morgan W.A., Pritchard T. & Vining B.A. (Eds) - Microbial Carbonates in Space and Time: Implications for Global Exploration and Production. *Geol. Soc. London Spec. Publ.*, 418: 209-219.

APPENDIX 1

Fig. 19 - Stratigraphic logs of the six analysed cores with indicated the depositional environments of the travertine and terrigenous facies.

SW NE N S

S2 S1 S2 (projected) S3 S4 S5-S6 S7

(315 m) (625 m) (1375 m) (150 m) (1100 m)

0 m 500 m

Present-day topographic surface

Proximal
Horizontal to gently dipping cm-size micro-terraces laterally extensive pools to terraced slope with dm-size pool rims

gentle dips W
sub-horizontal cm-size micro-terraces
cm-size micro-terraces dm-size pool rims
shallow pond with Charophytes
dm-size terraced with pool rims
cm-size microterraces

gentle dips E and S
sub-horizontal cm-size micro-terraces dm-size pool rims
karstic caves
shallow pond with Charophytes
sub-horizontal cm-size micro-terraces

sub-horizontal cm-size micro-terraces
horizontal shallow pond
shallow pond with Charophytes
dm-size terraced with pool rims
horizontal shallow pond
lacustrine/marsh organic-rich mudstone upper pyroclastic deposit
lacustrine/palustrine marls, siltstone, carbonate
lower pyroclastic deposit

Intermediate
Terraced slope with dm-size pool rims to smooth slope

sub-horizontal shallow pond pinching out N
karstic caves
terraced and smooth slope dipping E-S 5-30° pinching out W
dm-size terraced slope with pool rims

dm-size terraced slope with pool rims to smooth slope
smooth slope dipping 5-40° S and E, pinching out W
shallow pond with Charophytes and coated reeds
marls, sandstone and conglomerate
debris flow colluvial fan

Distal
Ponds with Charophytes, coated reeds and lacustrine to fluvial siliciclastics

shallow pond
dm-size terraced slope with pool rims
shallow pond with reeds and Charophytes pinching out W, E and N
karstic cave with speleothems and vadose pisoids
lacustrine-fluvial siltstone and marls
dm-size terraced slope with pool rims
shallow pond with reeds and Charophytes
upper pyroclastic deposit
lacustrine/palustrine marls and siltstone
fluvial conglomerate and sandstone

MWPGR B
msss br

M Calci-mudstone
W Wackestone
P Packstone
G Grainstone
R Rudstone/Floatstone
B Boundstone

m mudstone
s siltstone
ss sandstone
br breccia/conglomerate

Travertine facies

- T1 Crystalline dendrite cementstone
- T2 Clotted peloidal micrite dendrite boundstone
- T3 Micrite-microsparite crust boundstone
- T4 Coated gas bubble boundstone/wackestone
- T5 Laminated boundstone
- T6 Radial coated grain grainstone
- T7 Raft grainstone/rudstone
- T8 White coated reed boundstone to grainstone/rudstone
- T9 Brown coated reed and Charophytes boundstone
- T10 Clotted peloidal micrite grainstone/boundstone with Charophytes
- T11 Brown intraclastic phytoclastic grainstone/packstone/rudstone
- T12 White intraclastic coated grain grainstone/rudstone
- T13 Grey intraclastic extraclastic wackestone/floatstone/rudstone
- T14 Brown intraclastic phytoclastic packstone/grainstone to boundstone

Terrigenous facies

- F1 Black to dark grey mudstone
- F2 Green to grey volcanic pyroclastic deposits
- F3 Volcanic pyroclastic deposits with leucite
- F4 Dark grey to green volcanic ash deposits
- F5 White to light brown marls
- F6 Green to brown fine sand, silt and clay
- F7 Green sand to laminated sandstone
- F8 Chaotic mud-supported debris in green clay matrix
- F9 Polymictic conglomerate
- F10 Grey/green cross-laminated sandstone
- Lack of core recovery
- C1 Ostracode wackestone cavity fill
- C2 Columnar cementstone, extraclastic and pisoidal packstone/rudstone

- Lacustrine/marsh organic-rich mudstone
- Upper volcanic pyroclastic deposits with feldspatoids (Villa Senni - Tuscolano Artemisio Phase of Albani Hills)
- Lacustrine/palustrine marls, siltstones, carbonates with Charophytes
- Debris flow deposits from colluvial fans
- Fluvial conglomerate and sandstone
- Lower volcanic pyroclastic deposits